



ELECTRON DAMAGE EFFECTS ON CARBON NANOTUBE THIN FILMS

THESIS

Jeremy S. Best, Captain, USMC

AFIT-ENP-13-M-37

DEPARTMENT OF THE AIR FORCE
AIR UNIVERSITY

AIR FORCE INSTITUTE OF TECHNOLOGY

Wright-Patterson Air Force Base, Ohio

DISTRIBUTION STATEMENT A.

APPROVED FOR PUBLIC RELEASE; DISTRIBUTION UNLIMITED.

The views expressed in this document are those of the author and do not reflect the official policy or position of the United States Marine Corps, the United States Air Force, the United States Department of Defense or the United States Government. This material is declared a work of the U.S. Government and is not subject to copyright protection in the United States.

AFIT-ENP-13-M-37

ELECTRON DAMAGE EFFECTS ON CARBON NANOTUBE THIN FILMS

THESIS

Presented to the Faculty

Department of Engineering Physics

Graduate School of Engineering and Management

Air Force Institute of Technology

Air University

Air Education and Training Command

in Partial Fulfillment of the Requirements for the
Degree of Master of Science in Nuclear Engineering

Jeremy S. Best, BS Aerospace Engineering

Captain, USMC

March 2013

DISTRIBUTION STATEMENT A.

APPROVED FOR PUBLIC RELEASE; DISTRIBUTION UNLIMITED.

AFIT-ENP-13-M-37

ELECTRON DAMAGE EFFECTS ON CARBON NANOTUBE THIN FILMS

Jeremy S. Best, BS Aerospace Engineering
Captain, USMC

Approved:

Dr. John McClory, (Chairman)

Date

Dr. James Petrosky, (Member)

Date

Dr. Cory Cress, (Member)

Date

Capt Timothy Zens, PhD, USAF
(Member)

Date

Abstract

This research investigated the effects of electron damage on single walled carbon nanotube (CNT) thin films. CNT thin films were irradiated by electrons with energies of 500 keV and 1 MeV to determine what damage was created in the CNT thin film structure, how it affected conductivity, and what changes were evident in the Raman spectra.

Irradiation of a metallic sample to a fluence of $5.8 \times 10^{17} \frac{e^-}{cm^2}$ at 500 keV resulted in a change in the Raman D/G peak intensity ratio from 0.165 to 0.23, while the D/G' peak intensity ratio changed from 1.02 to 1.45. A semiconducting sample was irradiated to a fluence of $6.9 \times 10^{17} \frac{e^-}{cm^2}$ at 500 keV which showed a change in the D/G peak intensity ratio from 0.115 to 0.125, while the D/G' peak intensity ratio changed from 0.691 to 0.876. The semiconducting sample was then irradiated to a fluence of $2.2 \times 10^{17} \frac{e^-}{cm^2}$ with 1 MeV electrons. This showed a change in the D/G peak intensity ratio from 0.115 to 0.148, while the D/G' peak intensity ratio changed from 0.691 to 1.05.

A Hall study showed a 21% decrease in conductivity in the metallic sample after $2.5 \times 10^{16} \frac{e^-}{cm^2}$ at 500 keV while the semiconducting sample showed a 82% decrease in conductivity with $2.5 \times 10^{17} \frac{e^-}{cm^2}$. Carrier concentration did not substantially change with radiation, but the mobility decreased in both samples tested. An analysis of the radial breathing mode of the CNT thin film samples after irradiation is presented with potential indications of a change in the CNT average diameter.

This research provides insight into the performance of single walled CNT thin films perform under electron irradiation and shows that minor damage begins around $10^{16} \frac{e^-}{cm^2}$ and becomes more significant at electron fluences above $10^{17} \frac{e^-}{cm^2}$.

Acknowledgements

I would like to thank God for giving me the opportunity and ability to complete this course of study; my amazing wife for enduring me, my ramblings, and the many late nights spent working; My exuberant son who didn't get to see nearly as much of his daddy as he would have liked; and the great advice, direction and guidance I received from my advisor, Dr. John McClory, my committee, and all of the faculty at AFIT.

I recieved immeasurable help from Dr. Elizabeth Moore, Dr. David Look, Mr. John Hoelscher, Mr. Timothy Cooper, and Captain Merle Hamilton, USAF at AFRL Materials Directorate, and Sensors Directorate. Dr. Moore and John Hoelscher assisted with the Raman measurements, data analysis, and a general understanding of many physics principles along with substantial encouragement throughout the research. Dr. Look and Tim Cooper helped me with the Hall measurements, and understanding the physical processes involved in electrical transport through semiconductor and metallic materials. Captain Hamilton helped with access to the labs, introductions, and general support. Dr. Gary Farlow provided extensive help with the electron radiations in his lab at Wright State University, and many stimulating conversations regarding electron damage effects.

My fellow classmates were great for sharing the misery, long nights of working, and exchanging ideas. I would like to specifically thank Captain Jon Rowland, USAF for his direct assistance in plotting data in Matlab, and Major James Shinn, USA for many discussions on Raman spectra of carbon nanotubes.

Without all of this and more, success would not have been attainable.

Jeremy S. Best

Table of Contents

	Page
Abstract	iv
Acknowledgements	v
List of Figures	viii
List of Tables	xix
I. Introduction	1
1.1 Objectives	3
1.2 Overview of Research	3
1.3 Expectations	4
II. Theory	6
2.1 Origin of CNTs	7
2.2 CNT Synthesis	9
2.3 CNT Types	11
2.4 Electronic Type Separated SWCNT Thin Films	14
2.4.1 Metallic CNTs	15
2.4.2 Semiconducting CNTs	17
2.5 Electron Interaction	20
2.6 Defect Annealing	23
2.7 Conduction in SWCNT Thin Films	25
2.8 Hall Measurements	26
2.9 Substrate Effects	28
2.10 Raman Spectroscopy	29
2.10.1 General Raman Theory	29
2.10.2 Raman Spectroscopy on Single Walled Carbon Nanotubes	30
2.11 Silicon damage from electrons	32
2.12 Previous Research	34
III. Experiment	38
3.1 Purpose	38
3.2 Thin Films	38
3.2.1 Raman Spectroscopy	41
3.2.2 Dynamitron	43
3.3 Hall System	45
3.4 Setup and Design of Experiment	46
3.4.1 Raman Study	47

	Page
3.4.2 Hall Measurements	51
3.4.3 Vacuum Study	54
IV. Results and Analysis	58
4.1 Raman Study	58
4.1.1 Metallic Film	58
4.1.2 Semiconducting Film	61
4.2 Hall Study	65
4.2.1 Metallic Film	66
4.2.2 Semiconducting Film	69
4.3 Vacuum Study	72
4.4 Radial Breathing Mode Changes	73
V. Conclusions	76
5.1 Raman Study	76
5.2 Hall Study	77
5.3 Future Work	79
5.4 Overall Conclusions	80
Appendix A. Raman	82
1.1 D, G, and G' Maps	82
Appendix B. Appendix AFM	84
2.1 Atomic Force Images	84
2.2 Kelvin Probe Images	86
Appendix C. Modeling	90
3.1 Monte Carlo Modeling: CASINO	90
Appendix D. MathCad Dynamitron Calculations	96
Appendix E. Follow-On Procedures	99
Bibliography	102

List of Figures

Figure		Page
1.	Low earth orbit electron energy spectra which shows the average electron flux versus electron energy.	2
2.	Wire diagrams of various carbon structures relating to the different bonding schemes of carbon. (a) Shows graphite with sp^2 hybridization, (b) is the diamond structure with sp^3 hybridization, (c) is the Buckminster Fullerene or Bucky ball with sp^2 hybridization as a C-60 molecule, and (d) is a single walled carbon nanotube (SWCNT) with sp^2 hybridization.	6
3.	Wire diagram of a basic single walled carbon nanotube showing the rolled structure with hexagonal carbon-carbon bonds in the sp^2 hybridization structure.	8
4.	Drawing of an arc discharge system for producing CNTs. The low pressure helium atmosphere, high DC power, and graphite cathode / anode provide ideal conditions for the graphite to form into nanotubes. The lower pictures are TEM images of single walled and multi walled nanotubes.	10
5.	Representative image of using a surfactant solution and centrifugation to separate and isolate different morphologies of carbon nanotubes. The smaller, lighter semiconducting single walled CNTs rise to the top, below that are the metallic CNTs, while the larger multi walled CNTs sink to the bottom of a test tube after being spun in a centrifuge.	11
6.	Image of CNTs separated by the ultra-centrifugation technique, showing the optical contrast between different diameters, as well as SWCNTs separated from MWCNTs.	12
7.	Planar wire diagram of how each of the three different types of CNTs are described by their chirality, or how they are rolled up by the primary direction of the atomic bonding vectors.	13

8.	Wire diagram of how each of the three different types of CNTs are described by their chirality, or how they are rolled up by the primary direction of the atomic bonding vectors showing the chiral vectors (n, m) here for each type. Tube b represents the zigzag chirality, which can be metallic or semiconducting based on tube diameter, but tends to behave like a very narrow band semiconductor. Tube c represents the armchair chirality, which is primarily metallic. Tube d represents a chiral tube, which is almost always semiconducting. The effective band gap being dependent on the specific chiral vector.	15
9.	Mathematica [®] rendering of the momentum space of a carbon ring using the tight binding and zone folding techniques for understanding the energy band structure of metallic SWCNTs. The conduction and valence bands touch at a Fermi-Dirac point along the atomic k points.	16
10.	Mathematica [®] rendering of the momentum space of a carbon ring using the tight binding and zone folding techniques for understanding the energy band structure of semiconducting SWCNTs. The conduction and valence bands are separated based on the chirality of the CNT, which can vary significantly within a random network of CNTs such as a thin film.	18
11.	Adsorption geometry of oxygen molecule on the wall of the (10,0) nanotube and ab initio band structure calculation of the oxygen adsorbed nanotube system. Arrows in (b) indicate oxygen molecular states.	19
12.	Geometry of the ballistic ejection of a carbon atom from a single wall nanotube, illustrated in cross section. Note that angles α and γ are not necessarily coplanar. The electron beam is incident from the top, and causes carbon atom cascade knock-on effects into other CNTs in the vicinity of the primary knock on atom.	22
13.	Graph of carbon non-ionizing energy loss using Akkerman-Barak method.	24

Figure		Page
14.	Front walls of the same SWCNT just after energetic particle impact (left) and after annealing (right). During annealing the double vacancy (D) in the middle of the carbon network transformed to an agglomeration of non-hexagonal rings. The single vacancy (S) and the nearby carbon ad atom (A) in the upper right hand corner of the network transformed to a StoneWales 57 defect.	25
15.	Resistivity measurements using Van der Pauw methods. The four contacts are on the corners and are much smaller than the overall area of the sample. The contacts are numbers 1-4. Measurements from 1-2/2-1 and 4-3/3-4 represent vertical orientation while 1-4/4-1 and 2-3/3-2 represent horizontally oriented measurements.	27
16.	Phase imaging of electron beam irradiation at 10 keV on a 200 nm SiO ₂ layer on a Si and metal surface (triangle). The dark circles at the top show oxide charging effects. The metal distributes the electron beam charge, preventing the substrate from local charge buildup. The SiO ₂ will charge due to interactions with an electron beam, and subsequently affect anything on the surface of the oxide with local electric fields.	29
17.	This is a full spectrum Raman measurement with a 514.5 nm laser from 0 to 3000 cm ⁻¹ with an inset wire image labeling where the D and G phonon peaks arise from. The D peak is from defects causing scattering, while the G comes from the transfer of phonons down the long axis of the CNTs.	31
18.	Plot of non-ionizing energy loss of electrons in silicon and gallium arsenide reproduced from Akkerman-Barak. Electrons at 500 keV produce a NIEL of 1×10^{-5} MeV-cm ² /g.	33
19.	Results of Raman spectra changes with ion fluence on SWCNT thin films.	34

Figure	Page
20.	Results of an ion study with SWCNT thin films plot of Raman Spectra $\frac{D}{G}$. This figure shows the damage to SWCNTs created by ions at different fluences by comparing the ratio of the peak intensity of the D peak, with the peak intensity of the G peak in a Raman spectrum. As CNT damage increases, the ratio of the D to G peaks will correspondingly increase.35
21.	Results of temperature dependent conductivity as it changes with ion fluence on the sample.36
22.	The left figure (a) represents ion radiation results from Rossi <i>et al.</i> showing the changes in D/G, D/G', as well as R_s as a function of DDD, which is calculated from particle fluence. (b) shows the calculated average CNT tube length without vacancies caused by damage as a function of DDD.37
23.	Illustration of the fabrication technique used to create CNT thin films. Micro pore vacuum filtration to remove the CNTs from their surfactant solution is shown in the top left. The filter membrane is shown on the top right with the CNTs deposited on it. The filter membrane is then pressed down onto the silicon substrate, and acetone is used to dissolve the membrane. The bottom right graphic depicts the CNTs deposited on the substrate ready for further processing.39
24.	Optical photograph of the SWCNT thin films for Hall measurements, both 7 mm square. The semiconducting thin film is on the left, while the metallic thin film is on the right. The corner contacts are made from 100 nm of palladium deposited over the CNTs on a silicon dioxide layer grown over silicon.40
25.	Atomic force microscopy image of medium density single walled carbon nanotubes on a silicon substrate to illustrate the random nature of the CNT thin films used in this research. The scale is in microns.41

Figure	Page
26.	Atomic force microscope 3 dimensional representation of the semiconducting sample 127B. The oval highlights an average CNT with an approximate length of 1 μm and an average diameter of 1.5 nm.41
27.	Raman spectral plot of 3 laser lines used on metallic single walled carbon nanotube thin film. This shows the D peak, the G peak, and G' peaks with three different laser wavelengths available on the Raman system. The shift in the D and G' peaks with wavelength are due to energy dependent defect mode phonon interactions.42
28.	Image of the working parts of the Dynamitron electron accelerator showing the generator, the RF antennas surrounding the acceleration column, and the banks of diodes under the RF antennas.44
29.	Image of the large blue tank housing the working parts of the Dynamitron accelerator, including the tungsten filament, RF antennas, and diode banks. The tank is filled with SF ₆ at a pressure of 95 psi to minimize arcing in the accelerator.44
30.	Image of the 7mm diameter aluminum collimator used in all irradiations as mounted in the electron beam column.45
31.	Thin film Raman samples with representative circles indicating areas of electron irradiation with corresponding fluence and energy.47
32.	Representative digital photo of the experimental setup for the Raman study on the Dynamitron electron beam accelerator. This image shows sample 127A, with metallic SWCNTs in a thin film on Si/SiO ₂ , mounted on the cold head used in the irradiation study.49
33.	Representative digital photo of the experimental setup for the Raman study on the Dynamitron electron beam accelerator. This image shows sample 127A, with metallic SWCNTs in a thin film on Si/SiO ₂ , mounted on the cold head with an aluminum shield to isolate the other quadrants on the sample in the irradiation study.50

Figure	Page
34.	Photograph of the semiconducting Raman sample immediately following radiation and breaking vacuum while the sample is still mounted to the cold head. This clearly shows an area where water is adsorbed on the sample, corresponding to the area of irradiation at $6.9 \times 10^{17} \frac{e^-}{cm^2}$ 51
35.	EcopiaHMS 3000 pin board used to measure room temperature and liquid nitrogen Hall resistivity on samples. 54
36.	Experimental setup for Hall vacuum study with the sample mounted with thermal paste inside of a 1.0 T toroidal magnet placed on the copper cold head. 55
37.	IV curves taken with the Ecopia system while performing Hall measurements on the cold head with the metallic sample 134D. This shows both ambient temperature and pressure, along with 77 K measurements at ambient pressure and in vacuum. The results show that with a metallic CNT thin film, the 77 K and the pressure both serve to add resistance to the sample, but the pressure does not affect the metallic sample as much as the semiconducting sample shown in Figure 38. 56
38.	IV curves taken with the Ecopia system while performing Hall measurements on the cold head with the semiconducting sample 134H. This shows the sample becoming more resistive as the pressure is decreased. 57
39.	Normalized Raman spectra for the metallic Raman sample showing pre- and post-radiation spectra so that the increase in the D peak is obvious. The inset is the D peak. An annealing effect is seen in the post irradiation spectrum without direct radiation having an intensity lower than the pre-irradiated D peak intensity. The G' peak does not change substantially between pre- and post-radiation. 59

40.	Pre- and post- irradiation 2-dimensional map representation of the metallic SWCNT thin film used in the Raman study showing the D/G peak intensity ratio. This corresponds to three different areas of damage, with the highest electron fluence causing the most damage in the CNTs indicated in the bottom part of the figure.	60
41.	Pre- and post- irradiation 2-dimensional map representation of the metallic SWCNT thin film used in the Raman study showing the D/G' peak intensity ratio. This corresponds to three different areas of damage, with the highest electron fluence causing the most damage in the CNTs indicated in the bottom part of the figure.	60
42.	Pre- and post- irradiation Raman maps of the D/G peak intensity ratios after the first irradiation at 500 keV to a fluence of $6.9 \times 10^{17} \frac{e^-}{cm^2}$ over a period of 8 hours. This 2-dimensional map representation of the semiconducting SWCNT thin film used in the Raman study corresponds to the first area of irradiation on the lower right. The total D/G peak intensity ratio decreases after the first radiation.	61
43.	Pre- and post- irradiation 2-dimensional map representation of the semiconducting SWCNT thin film used in the Raman study after the first 500 keV electron irradiation to a fluence of $6.9 \times 10^{17} \frac{e^-}{cm^2}$ over a period of 8 hours. This shows an annealing effect of the heat and low pressure in the D/G' peak intensity ratio.	62
44.	Normalized Raman spectra for the semiconducting Raman sample showing pre- and post-radiation spectra so that the increase in the D peak is obvious. The inset here is the D peak. An annealing effect is seen in the post irradiation spectrum without direct radiation having an intensity lower than the pre-irradiated D peak intensity. The G' peak does not change substantially between pre- and post-radiation.	64

45.	Raman maps of the D/G peak intensity ratios after the first irradiation at 500 keV to a fluence of $6.9 \times 10^{17} \frac{e^-}{cm^2}$ over a period of 8 hours on the left. The right image is after the 1 MeV irradiation to a total electron fluence of $2.2 \times 10^{17} \frac{e^-}{cm^2}$ over a period of 6 hours. The scale is the same as Figure 42 from 0.08 to 0.18 in D/G peak intensity ratio.	64
46.	Raman spectra maps of the D/G' peak intensity ratios after the first irradiation at 500 keV to a fluence of $6.9 \times 10^{17} \frac{e^-}{cm^2}$ over a period of 8 hours on the left. The right image is after the 1 MeV irradiation to a total electron fluence of $2.2 \times 10^{17} \frac{e^-}{cm^2}$ over a period of 6 hours. The scale is lower than Figure 43 from 0.60 to 0.90 in D/G' peak intensity ratio. This highlights the two separate irradiation areas more clearly.	65
47.	Plot of metallic SWCNT thin film (134D) irradiated with $2.5 \times 10^{16} \frac{e^-}{cm^2}$ showing a change in the conductivity post-irradiation.	67
48.	Plot of the metallic Hall sample (134D) pre-irradiation (blue) and post-irradiation (red) mobility as a function of temperature.	67
49.	Plot of the metallic Hall sample (134D) pre-irradiation (blue) and post-irradiation (red) carrier concentration as a function of temperature.	68
50.	Metallic thin film sample 134D pre- and post-radiation Raman intensity map of the D peak intensity divided by the G' peak intensity created using the Renishaw WIRE program. The scale on the right hand side gives the color value of the D/G' peak intensity.	68
51.	Pre- and post-irradiation optical photographs of the semiconducting CNT sample 134H. This demonstrates the obvious difference in the thin films after irradiation with electrons. In this case, the sample was irradiated with 500 keV electrons to a total fluence of $2.5 \times 10^{17} \frac{e^-}{cm^2}$	69

Figure	Page
52.	Plot of semiconducting SWCNT thin film (134H) irradiated with $2.5 \times 10^{17} \frac{e^-}{cm^2}$ showing a change in the conductivity post-irradiation of 82%70
53.	Plot of the semiconducting Hall sample (134H) pre-irradiation (blue) and post-irradiation (red) mobility as a function of temperature.70
54.	Plot of the semiconducting Hall sample (134H) pre-irradiation (blue) and post-irradiation (red) carrier concentration as a function of temperature.71
55.	Plotted results of the vacuum study with the un-irradiated semiconducting sample 134J. This figure is plotted with conductivity on the vertical axis, as a function of pressure in torr on a log scale.73
56.	Plot of the radial breathing mode for sample 134D metallic CNTs. This shift is highlighted to show a potential annealing or diameter dependent degradation as a function of electron radiation damage.74
57.	Plot of the radial breathing mode for sample 134H semiconducting CNTs. This shift is highlighted to show a potential annealing or diameter dependent degradation as a function of electron radiation damage.75
58.	Displacement damage dose chart showing Raman measurements normalized to their pre-radiation values and plotted versus the calculated DDD. The general trend is an increase in damage as a function of radiation dose.78
59.	Raman maps of the semiconducting Raman sample 127B showing G peak intensity at 1592 cm^{-1} before and after the two separate irradiations. The left figure is pre-irradiation, the right figure is post irradiation The irradiations were 500 keV on the lower right, and 1 MeV on the lower left of the right figure.82

Figure	Page
60.	Raman maps of the semiconducting Raman sample 127B showing G' peak intensity at 2677 cm^{-1} before and after the two separate irradiations. The left figure is pre-irradiation, the right figure is post irradiation The irradiations were 500 keV on the lower right, and 1 MeV on the lower left of the right figure.82
61.	False color Raman peak intensity map of the semiconducting sample 127 B highlighting the D peak alone at 1341 cm^{-1} after the 2 irradiations, one at 500 keV (lower right)and one at 1 MeV (lower left). The scale on the right is the peak intensity count in arbitrary units.83
62.	Atomic force microscope image of metallic SWCNTs after $5.8\times10^{17}\frac{e^{-}}{cm^2}$ irradiation.84
63.	Atomic force microscope image zoomed in to $1\text{ }\mu\text{m}$ of metallic SWCNTs after $5.8\times10^{17}\frac{e^{-}}{cm^2}$ irradiation.85
64.	Kelvin Probe microscopy of the metallic sample 127 A on the unirradiated part86
65.	Kelvin Probe microscopy of the metallic sample 127 A on the $1.0\times10^{16}\frac{e^{-}}{cm^2}$ irradiation.87
66.	Kelvin Probe microscopy of the metallic sample 127 A on the $1.0\times10^{17}\frac{e^{-}}{cm^2}$ irradiation.88
67.	Kelvin Probe microscopy of the metallic sample 127 A on the $5.8\times10^{17}\frac{e^{-}}{cm^2}$ irradiation.89
68.	Casino model of 500 keV electrons incident from the top with the sample geometry as described in Chapter II. There are 200 electrons displayed here, with 1000 simulated. All of the simulated electrons pass through the CNT layer with little to no interaction. The CNT density is calculated from the physical sample geometry to be 1 g/cm^391

Figure	Page
69.	Casino model of 500 keV electrons incident from the top with the sample geometry as described in Chapter II. There are 200 electrons displayed here, with 1000 simulated. The CNT density is calculated from the physical sample geometry to be 1 g/cm ³ . This image shows where the electrons are stopping and depositing most of their energy. The color indicated the average intensity of the electrons as they slow down and interact with the sample geometry. 92
70.	Casino model of 1 MeV electrons incident from the top with the sample geometry as described in Chapter II. There are 200 electrons displayed here, with 1000 simulated. All of the simulated electrons pass through the CNT layer with little to no interaction. The CNT density is calculated from the physical sample geometry to be 1 g/cm ³ 93
71.	Casino model of 1 MeV electrons incident from the top with the sample geometry as described in Chapter II. There are 200 electrons displayed here, with 1000 simulated. The CNT density is calculated from the physical sample geometry to be 1 g/cm ³ . This image shows where the electrons are stopping and depositing most of their energy. The color indicated the average intensity of the electrons as they slow down and interact with the sample geometry. 94
72.	Casino simulation of 500 keV electrons onto the experimental setup using a 1 mm sheet of aluminum to shield the sample from the incident electrons. This shows that the electrons stop before .7 mm of aluminum and none reach the sample structure, proving the viability of aluminum to shield the sample. 95

List of Tables

Table		Page
1.	Table of the initial Hall measurements taken on an Accent HLS5500 Hall system before irradiation.	46
2.	D/G and D/G' peak intensity ratios for metallic fluence sample 127A showing the unirradiated and electron irradiated values. The associated fluences are indicated, with all irradiations done with 500 keV electrons. These all show an increase in the D/G and D/G' peak intensity ratios with radiation, indicating damage to the CNTs.	59
3.	Table of the D/G and D/G' ratios for semiconducting fluence sample 127B showing the unirradiated and electron irradiated values. The post radiation values are separated into the 500 keV irradiation and the 1 MeV irradiation with associated fluences indicated. These show an increase in the D/G ratio and D/G' with radiation, indicating damage to the individual CNTs. The D/G and D/G' ratios increased substantially with the 1 MeV irradiation as expected indicating significant damage to the CNTs within the thin film network.	63
4.	This table summarizes the room temperature Hall measurements on both the semiconducting and metallic SWCNT thin films for the pre- and post-irradiation measurements with the corresponding changes noted.	66
5.	Table of the D/G and D/G' ratios for metallic sample 134D showing the unirradiated and electron irradiated values. The post radiation values show a slight decrease in the D/G ratio, while the D/G' ratio increased indicating some damage within the individual CNTs within the thin film network.	69
6.	Table of the D/G and D/G' ratios for semiconducting sample 134H showing the unirradiated and electron irradiated values. The post radiation values show an increase in the D/G ratio, while the D/G' ratio remained the same within experimental error.	71

7.	This table summarizes the Raman changes within all of the samples tested, specifically the ratio of the D/G and D/G' intensities.	77
----	--	----

ELECTRON DAMAGE EFFECTS ON CARBON NANOTUBE THIN FILMS

I. Introduction

Technology continues to evolve in the semiconductor industry, with the current technology allowing for transistor dimensions on the order of 10's of nanometers (nm). Carbon nanotubes represent a recent discovery that can be used in electrical devices allowing for single digit nanometer technology. In theory, this could take computer chips from the current 22 nm technology down to as low as 5 nm technology. This could dramatically increase the number of transistors on a single chip.

In addition to their small size, ideal carbon nanotubes (CNTs) display ambipolar and nearly ballistic transport properties with very little heat buildup. The ambipolar transport refers to both electrons or holes as the primary conductive mechanism, as opposed to silicon based devices which are designed as n-type (electrons) or p-type (holes) for electrical transport. Nearly ballistic transport refers to the carriers traveling without scattering, which has been measured as high as 1/300th the speed of light in isolated single walled carbon nanotubes (SWCNT).[1] With these properties, devices made from carbon nanotubes could be made very small, use less power to drive them than current semiconductor technology, and have significantly less heat buildup in normal operating conditions.

Carbon nanotubes also have been shown to be more resistant to radiation than traditional silicon based devices.[2] [3] [4] [5] [6] This radiation resistance is still the subject of research using different radiation types such as electrons, neutrons, and ions. This resistance to radiation is particularly promising in space applications, such as integrated circuits for satellites where the radiation environment includes protons,

neutrons, electrons, and heavy ions across a broad energy spectrum.[7] The energy range from 500 keV to 1 MeV represents a significant portion of the average daily flux of electrons in low Earth orbit.[8] Figure 1 from Stassinopoulos *et al.*, plots the average electron flux as a function of electron energy on a log-log scale for a satellite in low earth orbit. This figure shows that for electrons at and above 500 keV, the

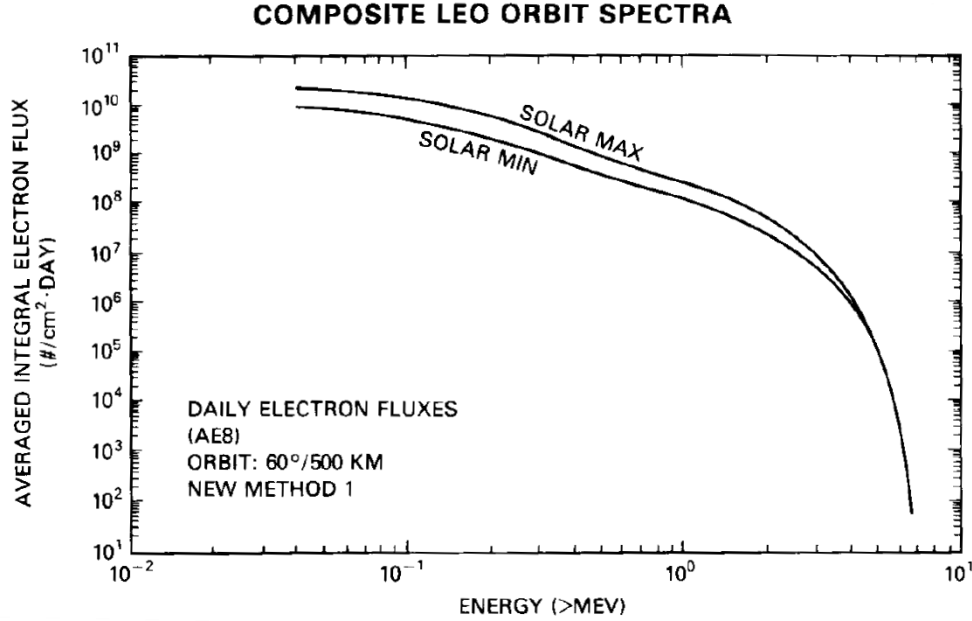


Figure 1. Low Earth Orbit Electron energy spectra which shows the average electron flux versus electron energy. Reproduced with permission from Stassinopoulos *et al.*[8]

average daily flux of electrons is on the order of 10^9 electrons per cm^2 . Using this as a baseline, the yearly fluence can be calculated as 3.65×10^{11} electrons per cm^2 at energies of 500 keV and above. Extending this out to the expected lifetime of a satellite in low earth orbit of 20 years, the total expected fluence of electrons on satellite electronics is 7.3×10^{12} electrons per cm^2 at 500 keV or above. This would be a minimum electron fluence to research for damage to CNT thin films; however, previous research indicates that a much higher fluence of electrons is needed to see significant damage effects.

1.1 Objectives

This research seeks to understand the physical and electrical changes in single walled CNT thin films in an electron radiation environment. This work follows ion irradiations of single walled CNT thin films by Cress *et al.*, [2], Rossi *et al.*, [3] and seeks to obtain data about electron irradiation to correlate with the calculations in those two references. Specifically, the correlation of Raman spectroscopy results and changes to the conductivity as a function of the total electron fluence. This radiation response can be directly related to the displacement damage dose (DDD). The DDD allows calculation of damage effects in electronic type separated SWCNTs in any type of radiation environment.

The SWCNT thin films are measured pre- and post-irradiation with Raman spectroscopy, as well as the temperature dependent Hall effect. The electron irradiations are accomplished at the Wright State University Dynamitron electron accelerator facility. The Raman spectroscopy measurements pre- and post-irradiation facilitate the separation of CNT only effects from those occurring due to other processes such as substrate oxide charging. Following the work of Cress *et al.*, and Rossi *et al.*, this research investigates electron fluences above 1×10^{16} electrons per cm^2 . Characterizing the damage to CNTs caused by electrons at 500 keV and 1 MeV will increase understanding of the overall electrical properties of networks of carbon nanotubes in thin film structures. In the future these thin film structures can then be functionalized in field effect transistors for space application allowing high current capacity, high speed switching, and radiation resistance.

1.2 Overview of Research

This research consists of CNT thin film samples irradiated with a high fluence (greater than $10^{16} \frac{e^-}{\text{cm}^2}$) of electrons in order to observe changes to the electrical prop-

erties of the material caused by structural damage in the form of carbon site defects in the carbon nanotubes. The experimental plan focuses on an electron energy of 500 keV. This type of research has been done with other radiation sources and structures, but not electrons in thin film structures.[2] [7] The samples in this study have detailed pre- and post-irradiation characterization by Raman spectroscopy for the purpose of observing the changes to the ratio of the D peak intensity to the G and G' peak intensity as a function of electron fluence. In addition to Raman spectroscopy, samples are measured electrically using the van der Pauw method of Hall characterization pre- and post- irradiation. This is first done at ambient temperature and pressure, followed by a full temperature sweep Hall measurement from liquid nitrogen (77 K) up to room temperature (300 K) at ambient pressure. A separate study is presented with un-irradiated samples comparing the conductivity of the samples under vacuum, at ambient temperatures. Additionally, the radial breathing mode (RBM) is reviewed for changes in average tube diameter after irradiations to understand radiation induced structural changes.

1.3 Expectations

Previous research indicates a decrease in conductivity within the network of CNTs from non-ionizing radiation damage that can be correlated to the radiation fluence of any radiation source. This decrease in conductivity is shown to be a function of CNT damage through Raman spectroscopy which isolates the damage to the individual CNTs. The changes to the transport properties between CNTs is shown through temperature dependent Hall measurements. [2] [7] [3]

This research is expected to follow the same methods as previous research. The specific mechanism of damage to the CNTs is carbon atom displacement described by knock-on effects. The Raman spectrum changes as a function of electron fluence,

specifically, an increase in the D peak intensity while the G and G' peak intensities decrease. In a spectrum normalized to the peak intensity of the G peak, the D peak is expected to increase enough to indicate damage to the CNT structure. The conductivity of the CNT thin films is also expected to decrease as a function of radiation damage. This is expected because of increases in charge carrier scattering from disorder within the CNT network, as well as changes to the conduction between neighboring CNTs which dominates conduction in randomly oriented CNT networks.

II. Theory

Carbon has a very strong bonding structure of covalent bonds and many different molecular forms. Some of these well known forms are the diamond structure, graphite or graphene, and more recently the carbon nanotube and Buckyballs shown in Figure 2. Each of these carbon arrangements have unique properties. The structure in

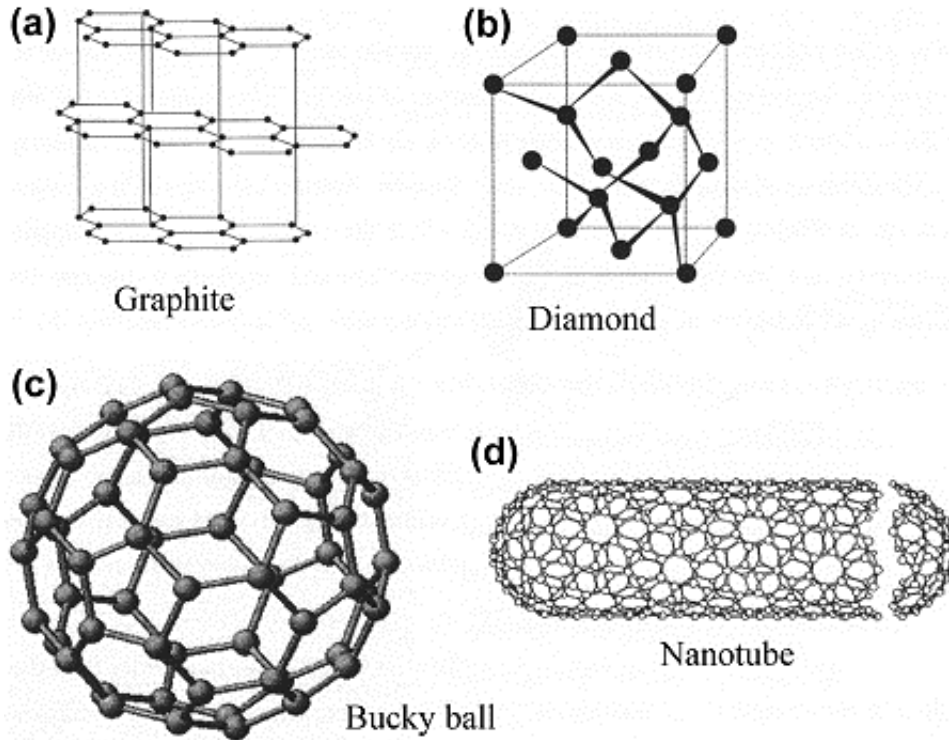


Figure 2. Wire diagrams of various carbon structures relating to the different bonding schemes of carbon. (a) Shows graphite with sp^2 hybridization, (b) is the diamond structure with sp^3 hybridization, (c) is the Buckminster Fullerene or Bucky ball with sp^2 hybridization as a C-60 molecule, and (d) is a single walled carbon nanotube (SWCNT) with sp^2 hybridization.

graphite is planar (shown in (a) of Figure 2), described by a 2 dimensional plane of hexagonal bonds of carbon. This forms the basis for understanding some of the properties of carbon nanotubes. A carbon nanotube (CNT) is an arrangement of carbon atoms in a tube structure that can be described by rolling a planar sheet of

graphite and having all of the atomic bonds satisfied with sp^2 covalent bonds. An ideal CNT is composed of a perfect arrangement of these bonds.[9] Although there are defects in CNTs, it is quantum mechanically preferential to satisfy all of the bonds to remain at the lowest energy state and maintain stability. There is a very low statistical defect density in most prepared and purified single walled CNTs used in research. As a result of the strong bonds, low defect density, and small size, there are some interesting properties of individual carbon nanotubes. These properties include an extremely high strength to weight ratio, a high thermal conductivity, and electrical conductivity 6 orders of magnitude higher than copper.[10]

2.1 Origin of CNTs

It is difficult to pinpoint the discovery of carbon nanotubes (CNTs) since there were papers produced in the former Soviet Union around 1975,[11] and other papers detailing carbonaceous tubules from the 1950's and after.[9] It has been more recently discovered that the famous Damascus steel with its characteristic carbon lines along the folds of the hand forged steel have carbon nanotubes within the carbon of the steel, so this is not a new manifestation of carbon, just a more scientific understanding of the structure and properties of CNTs. Carbon nanotubes were sensationalized by Sumio Iijima at NEC in 1991 from his work on synthesizing fullerenes, also known as Buckyballs, by arc discharge.[12] He noticed some carbon sooty deposits on the cathode of this arc discharge system and analyzed them in a transmission electron microscope (TEM) showing a variety of closed graphitic structures including nanoparticles and nanotubes of a type which had never previously been observed at that scale.[1] [13] He had discovered primarily multi-walled carbon nanotubes (MWCNTs) from the cathode end of his arc discharge system.[14] His resulting paper opened the door to CNT research and made it the "new" amazing material that soon promised to revo-

lutionize everything from structural materials to electronic circuit elements.[15] [16]
Carbon nanotubes such as the one depicted in Figure 3 represent the next logical step

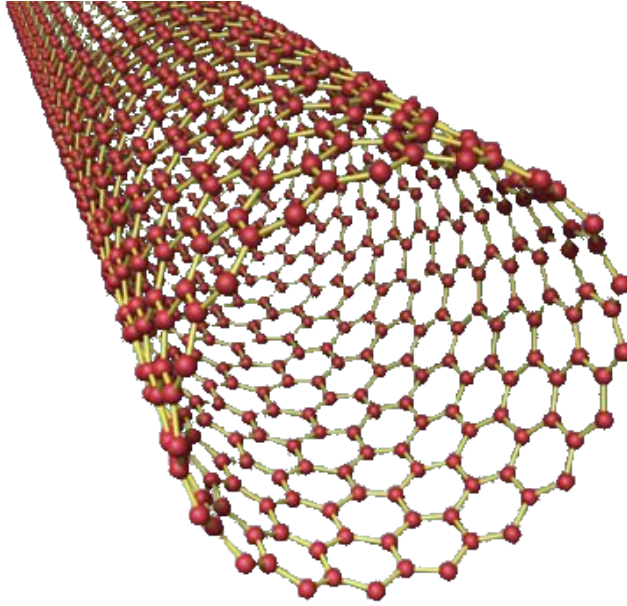


Figure 3. Wire diagram of a basic single walled carbon nanotube showing the rolled structure with hexagonal carbon-carbon bonds in the sp^2 hybridization structure.

in creating smaller scale electrical devices to advance the oft cited Moore's Law. [10] [9]. The relative size and function of these devices has the potential to increase the number of transistors, the switching speed, current capacity and overall device speed by several orders of magnitude. [1]

Although many papers have been published on this subject,[16] and many experiments have been done, there are still many technological and conceptual hurdles to overcome before these devices are fully functionalized and able to be mass produced into integrated circuits.[11] One of the steps toward this goal is studying carbon nanotube thin films as a bulk material before attempting to functionalize these into devices such as CNT thin film field effect transistors.[2]

2.2 CNT Synthesis

Growth Mechanisms

Carbon nanotubes are grown primarily through 3 processes: arc discharge, laser ablation, and chemical vapor deposition (CVD).[17] Each method has advantages and disadvantages. The arc discharge system is relatively simple and easy to operate, although it produces a low volume of CNTs relative to the total amount of carbon structures resulting from the process. Laser ablation has a higher yield of CNTs, but at a high cost of using argon gas, a high temperature furnace, and a high power laser with associated production complication and maintenance cost. The CVD method is simple to operate, patternable, and produces a high yield of CNTs. The CNTs used in this research were produced using the arc discharge method by NanoIntegris®.

Arc Discharge

The arc discharge method is how Sumio Iijima originally discovered CNTs, and remains a relatively cheap and popular method of growing nanotubes. Batch processing is possible with a large cathode, large anode, and enough available power for the system. Figure 4 shows a representative drawing of this system. In this method, a metal catalyst doped graphite anode is separated from a pure graphite cathode in a very low pressure helium atmosphere while a high voltage is placed on the system between the cathode and anode, so that the electricity arcs between the anode and the cathode breaking up some of the graphite in a plasma. When the ionized carbon recombines it forms CNTs of various types.

CNT Purification

All of the CNT growth methods produce multi-walled and single walled nanotubes, as well as Buckyballs and amorphous carbon in a random mixture. Arc discharge and laser ablation produce CNTs that are quasi-randomly oriented and distributed throughout various CNT diameters. The carbon nanotubes, in this ran-

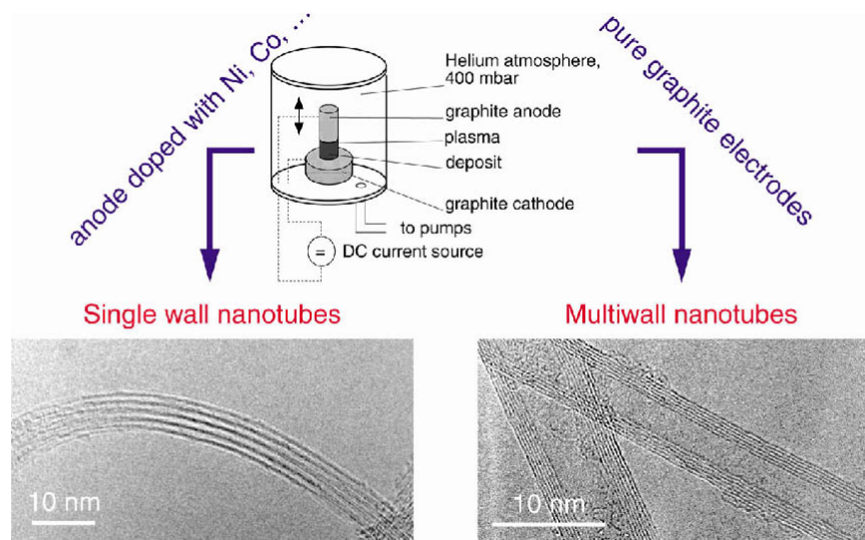


Figure 4. Drawing of an arc discharge system for producing CNTs. The low pressure helium atmosphere, high DC power, and graphite cathode / anode provide ideal conditions for the graphite to form into nanotubes. The lower pictures are TEM images of single walled and multi walled nanotubes. Reproduced with permission.[7]

dom arrangement, are not very functional. The impurities must be separated, while different tubes must be isolated and purified in order to functionalize them into usable material. One of the most efficient ways of doing this is ultrasonication in a surfactant solution as represented in Figure 5, followed by micro-pore filtration to remove the larger amorphous carbon particles, then ultra-centrifugation to separate the tubes. [3] Representative results of centrifugation are shown in Figure 6.

The great advantage of this processing technique is that the yield of specific dimensions of CNTs, specifically for single walled CNTs of a specific morphology, is usually over 95% which can be further improved up to 99% purity.[18] [19] This high purity yield of specific morphology and electronic type CNTs allows them to be further processed into structures and devices that have consistent properties and devices that are functional and repeatable. One such application of this process is the creation of CNT thin films that are used for research purposes to understand the physics of electrical transport in random networks of bulk single walled CNTs. This purification

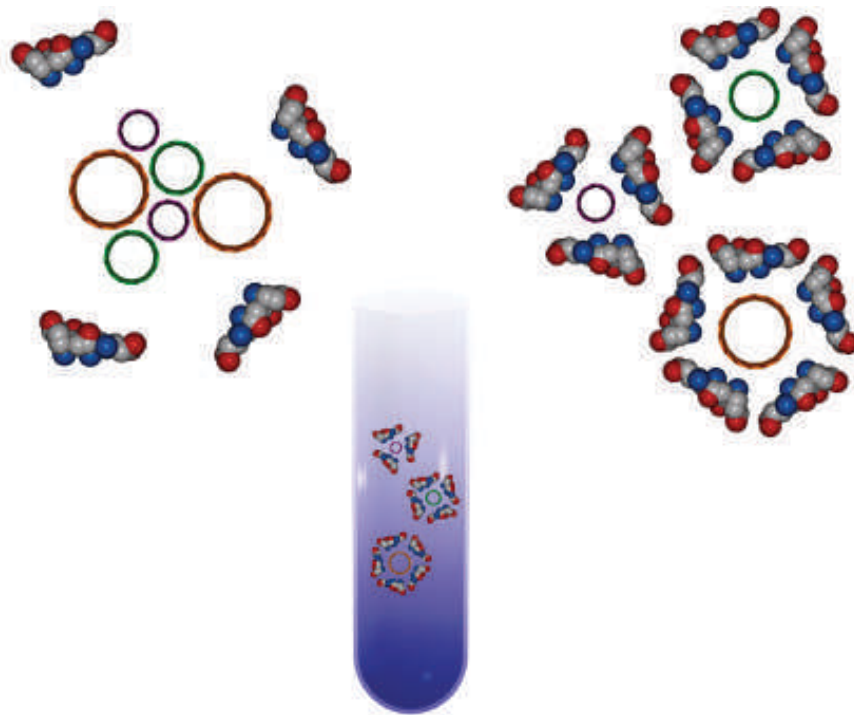


Figure 5. Representative image of using a surfactant solution and centrifugation to separate and isolate different morphologies of carbon nanotubes. The smaller, lighter semiconducting single walled CNTs rise to the top, below that are the metallic CNTs, while the larger multi walled CNTs sink to the bottom of a test tube after being spun in a centrifuge. Reproduced with permission from Arnold *et al.*[18]

process is further explained in Chapter III as it is the method used to produce the high purity, electronic type separated CNTs used in the thin films of this research.

2.3 CNT Types

Carbon nanotubes come in two different and very distinct forms. Multi-walled CNTs (MWCNTs) are tubes within tubes, which can have very complicated properties with varying inner and outer diameters. MWCNTs have as few as two walls with no apparent upper boundary to the number of walls measured (above 50 concentric tubes). The bulk of research to date has focused on multi-walled tubes with 2 to 10 concentric tubes. These MWCNTs have been functionalized in random networks for strengthening materials and heat dissipation. There is also ongoing research using

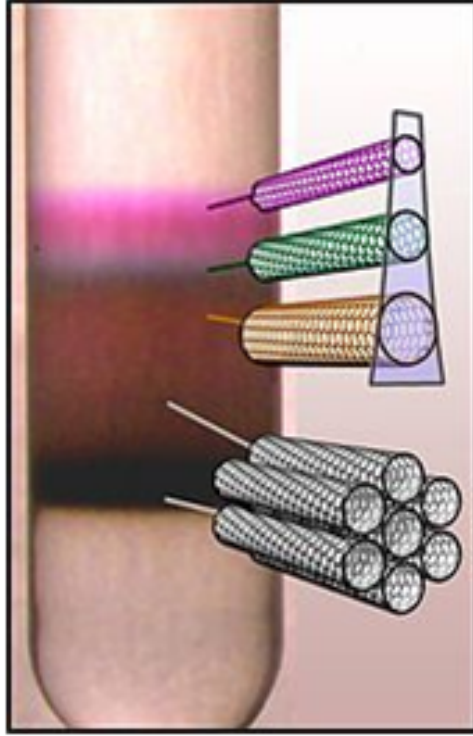


Figure 6. Image of CNTs separated by the ultra-centrifugation technique, showing the optical contrast between different diameters, as well as SWCNTs separated from MWCNTs. Reproduced with permission from Arnold *et al.*[18] [19]

MWCNTs grown in fully aligned patterned “forests” for heat sinks to dissipate excess heat from integrated circuits because of their dramatic thermal conductivity in the axial direction.

Single walled CNTs are primarily distinguished by their tube diameter, chirality, and length. These three parameters are the most relevant for describing the observed properties of individual CNTs, as well as correlating to random networks in the thin film structures used in this research. These SWCNTs in the random network thin films have a wide range of diameters which, in conjunction with their chirality, affect their electrical transport properties. This results in either semiconducting or metallic SWCNTs.

Chirality

The chirality, or roll of the CNT is the primary means of differentiating different

nanotubes and the specific properties of each. In particular, the electrical properties that arise from the different chiralities of nanotubes. These different chiralities,

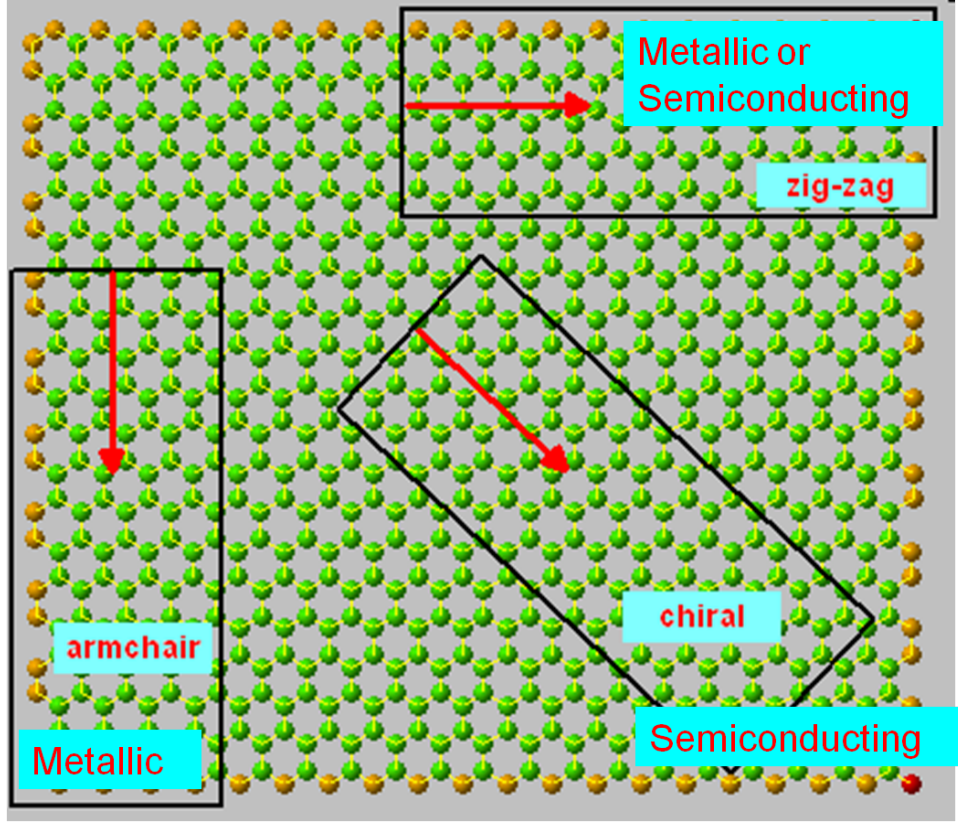


Figure 7. Planar wire diagram of how each of the three different types of CNTs are described by their chirality, or how they are rolled up by the primary direction of the atomic bonding vectors.

as shown in Figures 7 and 8 are armchair, zigzag, and chiral. The armchair variety of SWCNT is almost always metallic due to the direct path of electron travel along the circumference of the CNT. The zigzag chirality can be either metallic or semiconducting depending on the specific chiral vector. [20]

$$C_h = n_1 a_1 + n_2 a_2 \quad (1)$$

When $(2n_1) + n_2$ is an integer multiple of three, the CNT exhibits metallic behavior,

and for all others the CNT behaves as a semiconducting tube with various energy gaps based specifically on the chiral vectors that are represented by Figures 7, 8 and 10. In semiconducting CNTs the two bands do not cross at E_F , but a diameter-dependent band gap develops with the equation from Avouris *et al.*[21]

$$E_{gap} = \frac{4\hbar v_F}{3d_{cnt}} \quad (2)$$

where d_{cnt} is the tubes diameter and v_F is the Fermi velocity at $\approx 8 \times 10^5$ m/s [13] from $v_F = \sqrt{\frac{2E_F}{m}}$ where E_F is the Fermi energy and m is the particle mass.[22]

Typical band gaps of isolated semiconducting CNTs are less than 1 eV. [21] The band gap for a semiconducting CNT with a diameter of 1.6 nm is 0.439 eV as an example relevant to the average tube diameter of the CNTs tested here. The chiral tubes are so named because there is no specific preferential chiral vector other than not being armchair or zigzag. These can also be either metallic or semiconducting, but tend to be more semiconducting due to the more apparent random nature of the atomic orientation along the axial direction. These different ways of rolling the nanotube produce very different electrical properties based on their energy band representations.

2.4 Electronic Type Separated SWCNT Thin Films

The use of thin film structures for CNTs ensures that there are enough conduction pathways between electrical contacts to allow for rapid conduction, switching in the case of field effect transistors, and high current capability. Thin films can be randomly distributed or oriented by using a magnetic field during the fabrication process. The structures used in this research are randomly distributed CNT thin films of between 50 nm and 100 nm thickness.

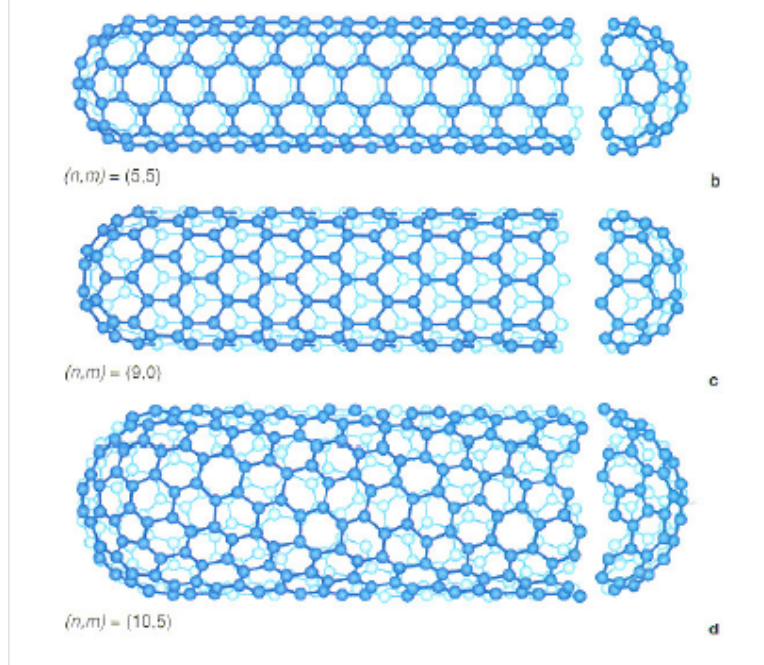


Figure 8. Wire diagram of how each of the three different types of CNTs are described by their chirality, or how they are rolled up by the primary direction of the atomic bonding vectors showing the chiral vectors (n, m) here for each type. Tube b represents the zigzag chirality, which can be metallic or semiconducting based on tube diameter, but tends to behave like a very narrow band semiconductor. Tube c represents the armchair chirality, which is primarily metallic. Tube d represents a chiral tube, which is almost always semiconducting. The effective band gap being dependent on the specific chiral vector.

When growing CNTs by any method described, the statistical average yield of CNTs electric properties tends to be 2/3 semiconducting and 1/3 metallic. The specific properties are based on the momentum space zone folding method. This method describes how the valence and conduction bands appear in relation to each other in momentum space.

2.4.1 Metallic CNTs

For metallic CNTs, the energy bands are conical and touch at a Fermi-Dirac point. This allows conduction freely from the valence to the conduction bands and results in metallic behavior shown graphically in Figure 9 through a Mathematica[®] code based

on the zone folding technique.[23] The complexity of the various roll geometries of CNTs influence their representation in real space as well as momentum space (k-space) because the unit cell of a CNT changes due to chirality with a vast number of possibilities. The zone folding technique involves using graphene as a basis for both real space and k-space representation. Along the CNT tube axis, the k-space is a one dimensional reciprocal lattice. Perpendicular to the axis direction, periodic boundary conditions are exact due to the rolled up nature of the CNT. The zone folding technique allows calculation of allowed k-states for any corresponding tube chirality. The approximate band structure of carbon nanotubes is obtained by using the band structure of graphene along allowed lines in k-space.[24] [25]

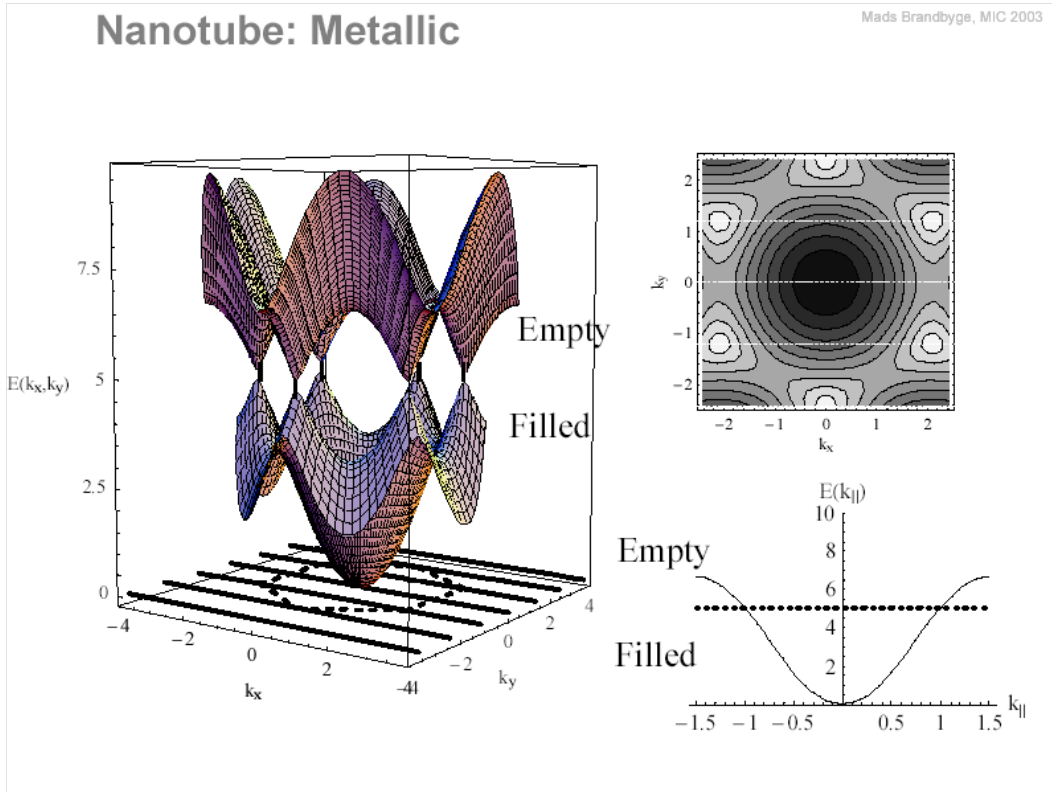


Figure 9. Mathematica[®] rendering of the momentum space of a carbon ring using the tight binding and zone folding techniques for understanding the energy band structure of metallic SWCNTs. The conduction and valence bands touch at a Fermi-Dirac point along the atomic k points. Reproduced with permission.[23]

The band structure of graphene, and that of metallic SWCNTs, has the valence and conduction bands touch at the edges of the first Brillouin zone and have a conical shape. The linear dispersion has profound consequences. These electrons and holes cannot be described by Schrödinger's equation. In typical semiconductor physics, electron and hole transport is described by band theory where the momentum space representation includes parabolically curving valence and conduction bands. This applies well to three dimensional crystalline transport, where carriers move from state to state based on thermal excitation and applied external fields. [26] In CNTs, the transport is not three-dimensional, but quasi-one-dimensional. The charge carriers are described as massless Dirac fermions with an effective velocity equal to $1/300$ of the velocity of light. [7] The sp^2 hybridized state of bonding has 3 of the 4 electrons in strong bonds, while the 4th valence electron is in a p orbital, and bonded with what is known as a π bond. This particular state leaves the electron free to conduct very easily and facilitates the quasi ballistic movement of charges through the 1-d structure through the π bonds.

2.4.2 Semiconducting CNTs

The semiconducting single walled nanotubes have an energy band structure graphically illustrated by Figure 10 using the same Mathematica[®] code as before. This is particularly interesting in that the same graphene bonding structure, in a slightly different orientation due to the chirality of the CNT, can produce a very different energy band structure resulting in semiconducting behavior. As the chiral vector changes from crossing the k-vector points, the band structure separates and creates an energy gap producing the semiconducting nature of these single walled CNTs. [23] The allowed states in the CNTs are cuts of the graphene bands indicated by the white

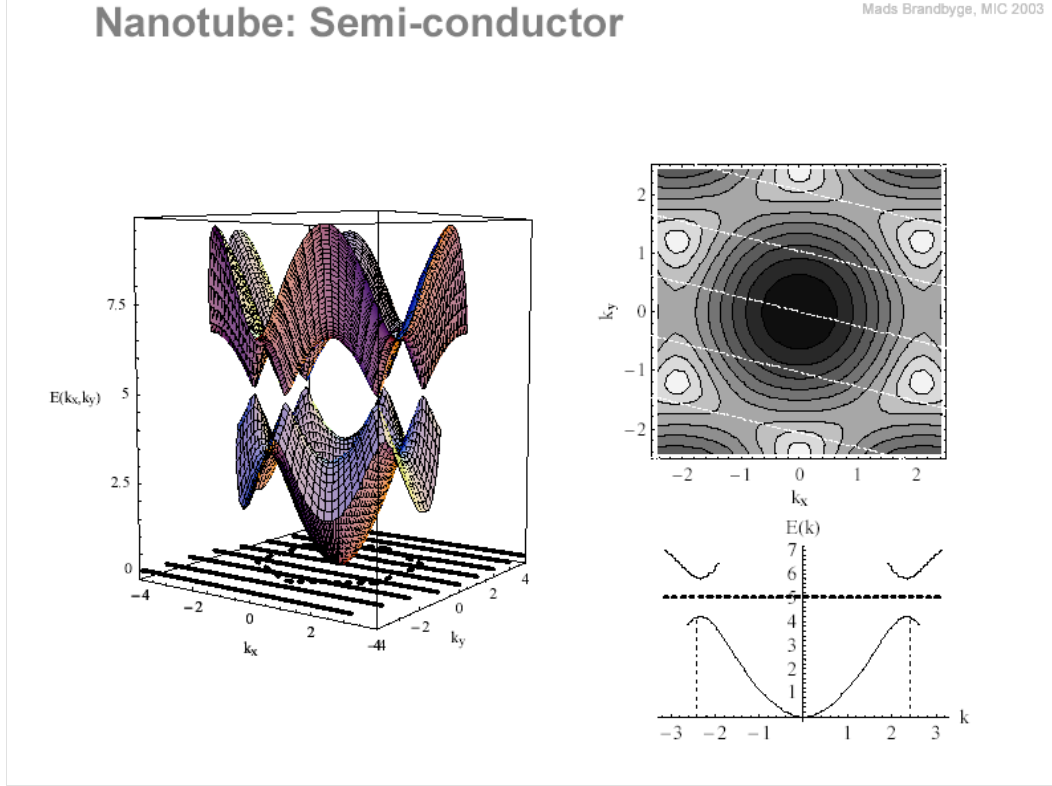


Figure 10. Mathematica[®] rendering of the momentum space of a carbon ring using the tight binding and zone folding techniques for understanding the energy band structure of semiconducting SWCNTs. The conduction and valence bands are separated based on the chirality of the CNT, which can vary significantly within a random network of CNTs such as a thin film. Reproduced with permission.[23]

lines. If the cut passes through a k -point, the CNT is metallic; otherwise, the CNT is semiconducting.[21]

Another property of the semiconducting CNTs arises from adsorption of ambient air molecules, primarily in the form of nitrogen and oxygen to the CNT walls due to electrostatic forces. This process allows some conduction pathways in semiconducting CNTs that would otherwise be forbidden by the band gap. This phenomenon can be prevented by keeping the CNTs in vacuum, or adding a non-conducting layer over the CNTs during the fabrication process to isolate them from adsorbents.[27] The image from Kang *et al.* in Figure 11 shows an example of an oxygen molecule adsorbed on a single CNT and how that changes the electronic band diagram. This adsorption

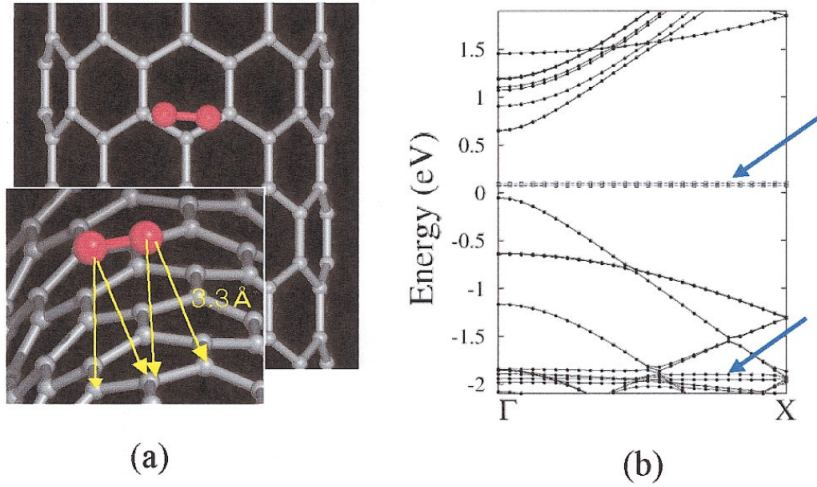


Figure 11. Adsorption geometry of oxygen molecule on the wall of the (10,0) nanotube and ab initio band structure calculation of the oxygen adsorbed nanotube system. Arrows in (b) indicate oxygen molecular states. Reproduced with permission from Kang *et al.*[28]

of nitrogen and oxygen is a difficult challenge to overcome in the functionalization of CNTs in semiconductor devices.[28]

The electronic properties of single-walled carbon nanotubes are shown to be extremely sensitive to the chemical environment in the paper by Collins *et al.* from 2000. Exposure to air or oxygen dramatically influences the nanotubes' electrical resistance, thermo-electric power, and local density of states, as determined by transport measurements and scanning tunneling spectroscopy. These electronic parameters can be reversibly “tuned” by surprisingly small concentrations of adsorbed gases, and an apparently semiconducting nanotube can be converted into an apparent metal through such exposure. Many supposedly intrinsic properties measured on as-prepared nanotubes may be severely compromised by extrinsic air exposure effects. [29] Hence the electronic properties of a given nanotube are not specified only by the diameter and chirality of the nanotube but depend critically on gas exposure history.[29]

Oxygen-saturated SWCNTs have a higher electrical conductance than do SWCNTs with less adsorbed oxygen.[29] Typically prepared SWCNT networks are invari-

ably air doped with an extrinsically induced hole like carrier concentration due to their preparation in an ambient air environment. Once SWCNTs have been exposed to oxygen, it is not possible to fully de-oxygenate them at room temperature even under high vacuum conditions (for example, simply placing air-exposed SWCNTs in a high-vacuum environment at room temperature does not suitably clean them; the samples must be heated in vacuum above 110 to 150 °C for several hours for most of the oxygen to be desorbed).[29] Water molecules can also be adsorbed on the nanotube and act like electron donors in a p-type semiconductor.[30]

2.5 Electron Interaction

When a highly energetic particle such as an electron or ion strikes the atoms of a target, different mechanisms of energy or momentum transfer take place. The most important primary radiation effects are:

- electronic excitation or ionization of individual atoms,
- collective electronic excitations, e.g. plasmons,
- breakage of bonds or cross-linking,
- generation of phonons, leading to heating of the target,
- displacement of atoms in the bulk of the target,
- sputtering of atoms from the surface.

Secondary effects are:

- emission of photons, e.g. x-rays or visible light,
- emission of secondary or Auger electrons, leading to a charging of the target.

When radiation effects in carbon are considered, it is useful to divide these contributions into those that lead to a displacement of atoms (knock-on effects) and those that do not (excitations).[4]

Atom displacements occur by knock-on collisions of highly energetic electrons or ions with the nuclei of the atoms in the specimen. This is the most substantial radiation effect in carbon nanostructures because of the 3d nature of the CNTs.[4]

The damage formation in CNTs is quite different from that observed in most other semiconductor solids. Because of the open structure of the CNT, even recoils which have received energy only slightly above the threshold energy can be displaced quite far, which is in contrast to many other types of materials.[31] In a well characterized crystalline solid such as silicon, the atoms are more tightly bound than those of the sp^2 bonded carbon atoms in CNTs. The empirical data presented by B. W. Smith *et al.* show that the threshold electron energy for knock-on damage to an isolated SWCNT is 86 keV. As the electron energy is increased from 86 to 139 keV with the upper bound assuming an isotropic graphene sheet, atoms first on the top and bottom surfaces and then on the side walls of the CNTs become susceptible to ballistic ejection. The top and bottom here are assumed to be normal to the radiation source, while the side walls are assumed to be in plane with the angle of the radiation. Above 139 keV, the probability increases for all atoms to be ejected.[32]

Two factors must be considered in determining whether or not the primary knock-on atom (PKA) will be ejected: (1) the energy transferred from the electron beam to the PKA and (2) the energy barrier that the PKA must overcome to escape from the CNT. In the former, only the maximum transferable energy for a given knock-on geometry is of interest since it is most important to calculate the minimum incident electron energy for which an ejection can occur. The ejection geometry is shown in Figure 12. The quantitative expression expressed in eV is a function of the incident

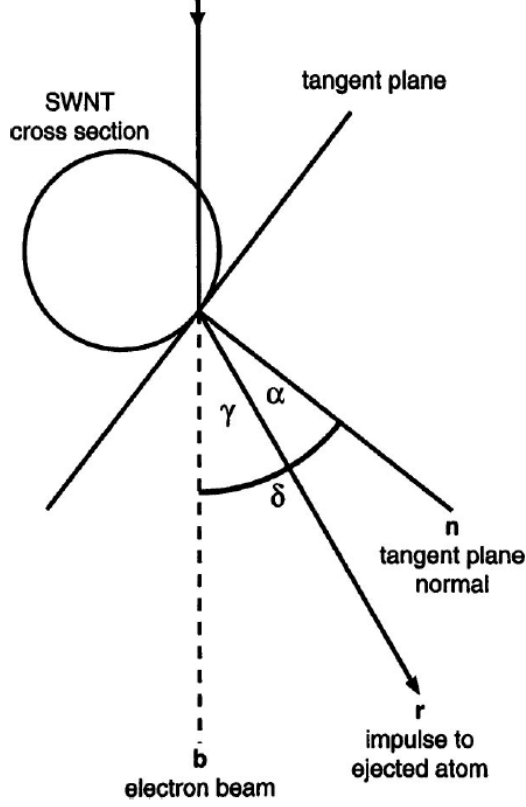


Figure 12. Geometry of the ballistic ejection of a carbon atom from a single wall nanotube, illustrated in cross section. Note that angles α and γ are not necessarily coplanar. The electron beam is incident from the top, and causes carbon atom cascade knock-on effects into other CNTs in the vicinity of the primary knock on atom. Reproduced with permission from Smith *et al.*[32]

electron energy V and the angle γ .

$$E_{transfer} = \frac{2V(V + 2m_0c^2)}{m_c c^2} \cos^2 \gamma \quad (3)$$

where m_0 is the mass of the electron and m_c is the mass of the carbon PKA.[32] This equation yields a value of 136 eV for carbon atoms, and 58 eV for silicon for comparison.

The Akkerman-Barak method of calculating the non-ionizing energy loss (NIEL) is used to quantify the probability of an atomic displacement caused by an energetic

electron. For electrons, the maximum energy transfer T_{max} is calculated by:

$$T_{max} = \frac{2T_0(T_0 + 1.022)}{M_0c^2A}, \quad (4)$$

where T_0 is the electron kinetic energy in MeV, A is the atomic mass in amu of the lattice-atom and $M_0c^2 = 931.5$ MeV is the equivalent energy for 1 amu.[33] This T_{max} is then substituted into the equation for NIEL:

$$NIEL_{e^-}(T_0) = \frac{N_A}{A} \int_{\theta_{min}}^{180^\circ} d\Omega Q[T(T_0, \theta)] T(T_0, \theta) \left(\frac{d\sigma}{d\Omega} \right)_{T_0} \quad (5)$$

where Ω is the solid angle of scattering. From the two body kinematics, T depends on the center of mass (CM) scattering angle θ through

$$T(T_0, \theta) = T_{max} \sin^2 \left(\frac{\theta}{2} \right). \quad (6)$$

The value of θ_{min} is obtained using

$$T(T_0, \theta_{max}) = 2T_d. \quad (7)$$

A plot of the NIEL as a function of electron energy is shown as Figure 13.[33]

2.6 Defect Annealing

There are differences in defect annealing with CNTs compared to traditional materials. In semiconductors like silicon, a vast majority of all Frenkel pairs produced are known to recombine below room temperature. In dense metals, nearly all the interstitials and vacancies produced during the ballistic phase of the cascade recombine with each other after only a few picoseconds, regardless of the sample temperature.

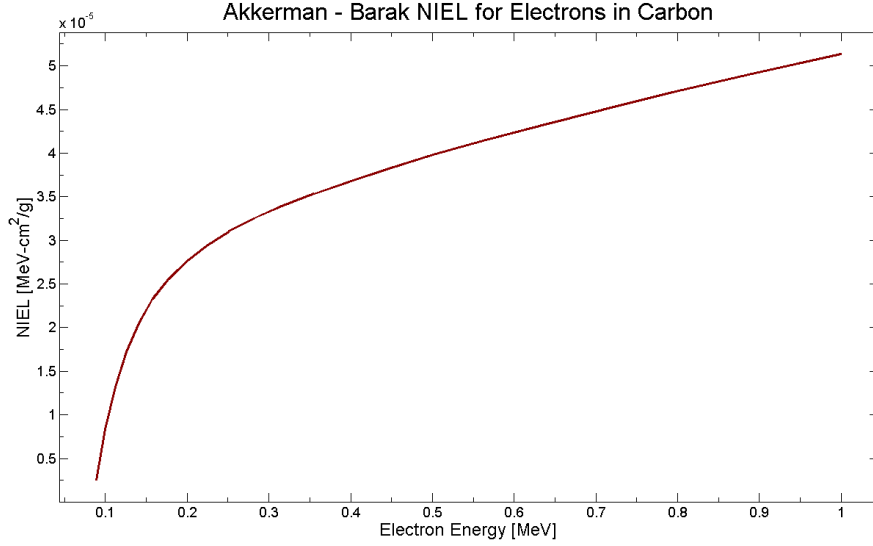
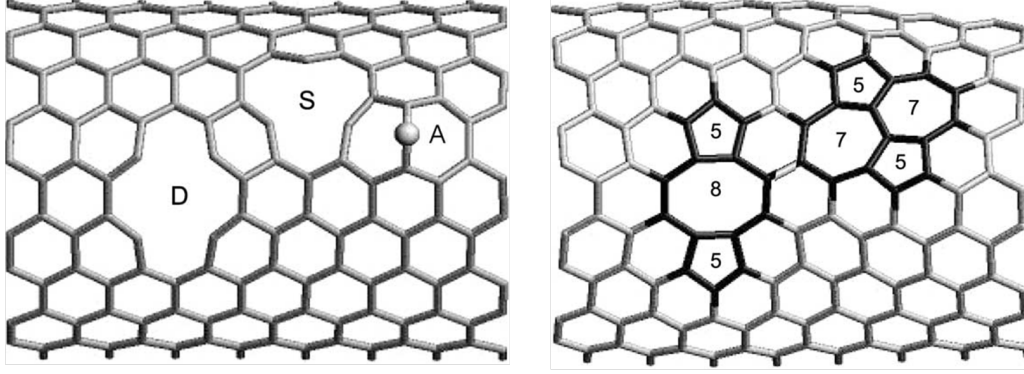


Figure 13. Graph of carbon non-ionizing energy loss using Akkerman-Barak method.

Defects in CNTs can also anneal; but it happens at elevated temperatures and the annealing mechanisms are somewhat different from those in metals.[31]

Previous research on electron irradiation of both SWCNTs and MWCNTs done by Krasheninnikov *et al.* in 2002 indicate that irradiation induced damage in nanotubes can easily be annealed at temperatures higher than 300 °C. Two mechanisms seem to govern the defect annealing.[34] The first mechanism is vacancy healing through dangling bond saturation and by the formation of non-hexagonal rings and Stone–Wales (S–W) defects. The Stone–Wales defects are formed when the normal hexagonal carbon bonding structure is broken by a displaced atom, or broken bond. Upon annealing this defect, pentagons and heptagons will form around the vacancy to achieve the lowest energy state of the CNT lattice structure.

An illustration of this mechanism is shown in Figure 14 where the front walls of the same SWCNT just after energetic particle impact (left) and after annealing (right) are shown. During annealing the double vacancy in the middle of the carbon network has been transformed to an agglomeration of non-hexagonal rings. The annealing also



Damage + Anneal = CNT diameter reduction = RBM peak increase

Figure 14. Front walls of the same SWCNT just after energetic particle impact (left) and after annealing (right). During annealing the double vacancy (D) in the middle of the carbon network transformed to an agglomeration of non-hexagonal rings. The single vacancy (S) and the nearby carbon ad atom (A) in the upper right hand corner of the network transformed to a StoneWales 57 defect. Reproduced with permission from Krashenninnikov *et al.*[31]

gives rise to the transformation of the single vacancy and the nearby carbon ad-atom in the upper right hand corner of the network to a S–W defect.[31] The annealing leads to local diameter reduction which is consistent with the work of Gerasimov in 2010. That work used transmission electron microscopy on CNTs to observe the reduction of CNT diameter as a function of electron fluence until the CNTs collapsed from instability below 0.4 nm in diameter.[35] The annealing should eventually result in disappearance of the S–W defect, especially if an extra carbon ad atom (which works as the catalyst for the transformation thus substantially reducing the defect annihilation barrier) is nearby.[31]

2.7 Conduction in SWCNT Thin Films

Non-ionizing damage effects in single walled carbon nanotube thin films appear to be dominated by two separate conduction mechanisms. The first is a fluctuation assisted tunneling model used to describe the difference in carbon nanotube electronic states. The second is a variable range hopping model that is used to describe the

conduction of charge carriers between neighboring CNTs.[5] The conductivity, $\sigma(T)$, is therefore a function of temperature in two terms:

$$\sigma(T) = B \exp\left(-\frac{T_b}{T_s + T}\right) + H \exp\left(-\frac{T_0}{T}\right)^\gamma \quad (8)$$

where B and H are fitting constants, T_b is related to the thermal conduction barrier, T_s is related to the zero temperature conductivity, and γ is variable range hopping term that is generally assumed to be one for CNTs.[7] The variable range hopping (VRH) model is used to describe a system where conduction cannot be explained by more traditional methods such as the crystalline transport used to describe conduction in metals and silicon devices.[36]

Hence, there are two primary conduction mechanisms in SWCNTs. These are starting points for building models based on experimental results. Conduction in CNT networks also depends on different growth techniques, purity levels, chirality and diameter distributions, as well as the thickness of CNT networks. These factors all play significant roles in describing the conduction in CNT thin films.

2.8 Hall Measurements

When a current-carrying semiconductor is kept in a magnetic field, the charge carriers of the semiconductor experience a force in a direction perpendicular to both the magnetic field and the current. At equilibrium, a voltage appears at the semiconductor edges.[37] From this voltage, the Hall coefficient can be determined.[26] The Hall coefficient is related to the electron and hole concentration, n and p , and the electron and hole mobility μ_e and μ_h by:

$$R_H = \frac{p\mu_h^2 - n\mu_e^2}{e(p\mu_h + n\mu_e)^2} \quad (9)$$

Van der Pauw

The Van der Pauw method of measuring resistivity and the Hall coefficient was developed in 1958 by Leo J. van der Pauw and has become a widely used method due to the ability to measure many variations of sample size and shapes. The sample must have a uniform thickness and be uniformly flat. [37] To measure resistivity, a current is applied to the edge of the sample while voltage is measured across the opposite edge of the samples according to Ohm's Law as shown in Figure 15.

For improved accuracy in resistance measurements, the polarity of the current is reversed and measured again for a total of 8 voltage measurements. By using a known current value, 10 micro-amps, and the measured voltages, Ohm's law is used to solve for 8 resistances.

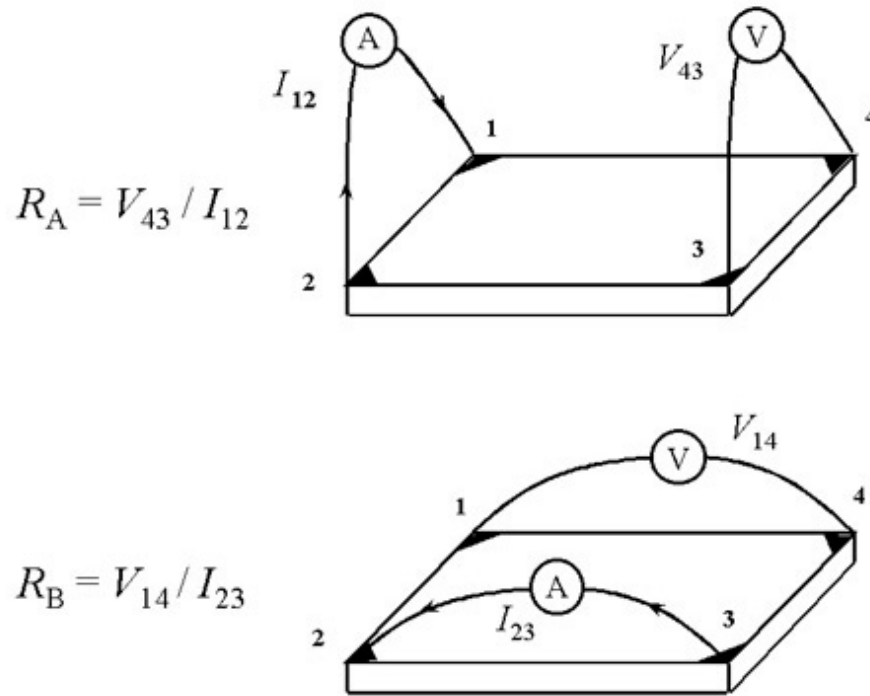


Figure 15. Resistivity measurements setup using Van der Pauw methods. The four contacts are on the corners and are much smaller than the overall area of the sample. The contacts are numbers 1-4. Measurements from 1-2/2-1 and 4-3/3-4 represent vertical orientation while 1-4/4-1 and 2-3/3-2 represent horizontally oriented measurements. Reproduced from Van der Pauw *et al.*[37]

From these 8 calculated values of resistance, the overall horizontal and vertical resistances, or R_A and R_B , respectively can be determined using the equations:

$$R_A = \frac{R_{12,34} + R_{34,12} + R_{21,43} + R_{43,21}}{4} \quad (10)$$

$$R_B = \frac{R_{23,41} + R_{41,23} + R_{32,14} + R_{14,32}}{4} \quad (11)$$

After determining R_A and R_B , the sheet resistance, R_S , is determined using an iterative routine to solve the Van der Pauw formula,

$$e^{-\pi R_A/R_s} + e^{-\pi R_B/R_s} = 1. \quad (12)$$

2.9 Substrate Effects

The substrate that the CNTs are deposited on can have an influence on the electrical properties of CNT thin films. This is particularly important when dealing with oxides in a radiation environment. The CNTs for this research have been deposited on a 300 nm SiO₂ layer grown on a Si substrate. The effect of radiation, in this case high energy electrons, will tend to cause charge buildup in the SiO₂ layer.[38] This could cause local electric fields in the oxide layer that will affect conduction in the CNTs. This effect is shown graphically in Rius *et al.* from 2007, where an atomic force microscope, along with a Kelvin probe microscope is used to map the local charging effects of a silicon dioxide layer after irradiation with an electron beam from a scanning electron microscope as shown in Figure 16.[39] Due to the high probability of the electrons passing through the CNT thin films without interaction, the substrate charging effects are potentially significant with the 500 keV electrons used in this research.

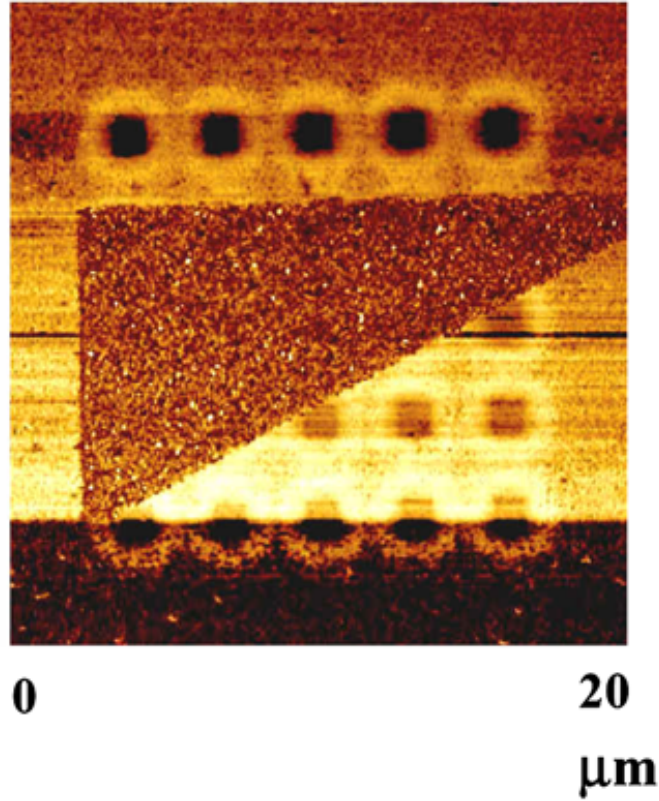


Figure 16. Phase imaging of electron beam irradiation at 10 keV on a 200 nm SiO_2 layer on a Si and metal surface (triangle). The dark circles at the top show oxide charging effects. The metal distributes the electron beam charge, preventing the substrate from local charge buildup. The SiO_2 will charge due to interactions with an electron beam, and subsequently affect anything on the surface of the oxide with local electric fields. Reproduced with permission from Ruis *et al.*[39]

2.10 Raman Spectroscopy

2.10.1 General Raman Theory

The Raman effect occurs when light impinges upon a molecule and interacts with the electron cloud and the bonds of that molecule. It relies on inelastic scattering, or Raman scattering, of monochromatic light, usually from a laser in the visible, near infrared, or near ultraviolet range. The laser light interacts with molecular vibrations, phonons or other excitations in the system, resulting in the energy of the laser photons being shifted up or down. The difference in energy between the original state and this

new state leads to a shift in the emitted photon's frequency away from the excitation wavelength. [40]

If the final vibrational state of the molecule is more energetic than the initial state, then the emitted photon will be shifted to a lower frequency in order for the total energy of the system to remain conserved. This shift in frequency is designated as a Stokes shift. If the final vibrational state is less energetic than the initial state, then the emitted photon will be shifted to a higher frequency. This is designated as an Anti-Stokes shift. [40]

The Raman spectrum of a sample is typically given in inverse centimeters (cm^{-1}), which is known as wavenumbers. The Stokes lines are typically stronger, and tend to be the most widely published and analyzed numbers. It is straightforward to convert from wavenumbers to units of energy, eV by using the Plank relation:

$$E = hc\nu \quad (13)$$

where h is Plank's constant in eV*s: 4.136×10^{-15} , c is the speed of light, and ν is the wavenumber. The dominant Stokes line for silicon is at 520 cm^{-1} , which gives an energy of the phonon transition at 0.0645 eV.

2.10.2 Raman Spectroscopy on Single Walled Carbon Nanotubes

The primary reason for using Raman spectroscopy on single walled carbon nanotubes is the strength and clarity of the spectrum on high purity SWCNTs.[41] There are between 100 and 150 phonons known in SWCNTs. Only about 12 of these phonon modes are Raman active in armchair and zigzag CNTs. Semiconducting CNTs have 15 Raman active phonon modes. Of these many Raman active phonon modes, there are only a few that are useful for this particular research project: the RBM, D, G, and G' peaks. The spectrum shown in Figure 17 is from freestanding, randomly oriented,

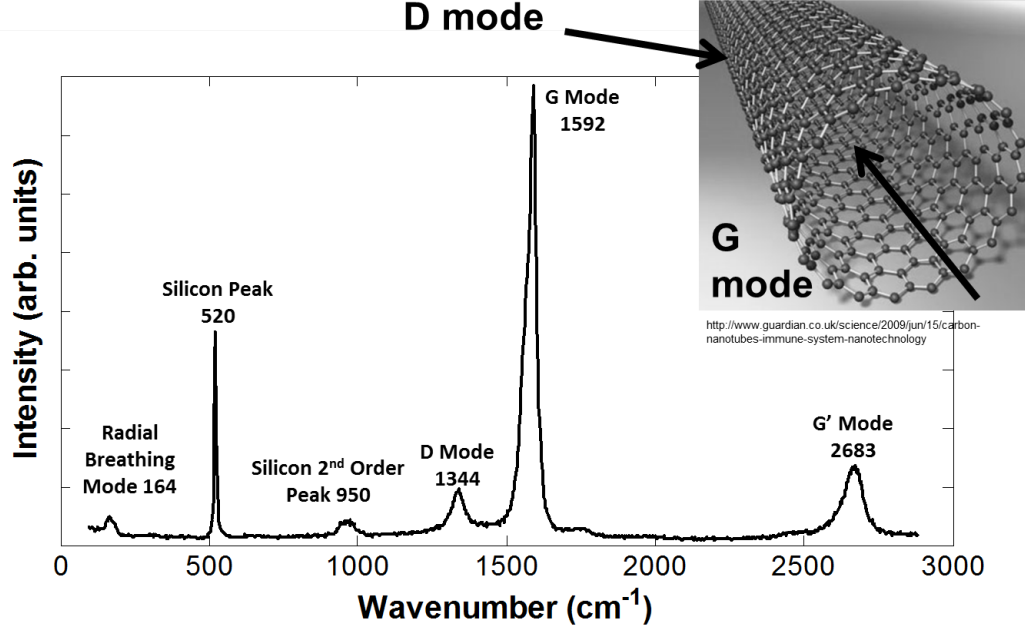


Figure 17. This is a full spectrum Raman measurement with a 514.5 nm laser from 0 to 3000 cm^{-1} with an inset wire image labeling where the D and G phonon peaks arise from. The D peak is from defects causing scattering, while the G comes from the transfer of phonons down the long axis of the CNTs.

semiconducting CNTs from Nano-Integris fabricated into a Hall effect thin film test structure. This has a very clear peak for the radial breathing mode at 164 cm^{-1} which allows computation of the average diameter of the SWCNTs by using Equation 14. [42]

$$d_{avg}(nm) = \frac{248(\text{cm}^{-1}) * nm}{RBM_{peak}(\text{cm}^{-1})} \quad (14)$$

The radial breathing mode (RBM) is so named because it corresponds with phonon interactions along the radius of the CNT, a sort of stretching and relaxing of the radius of the CNT. This particular feature is unique to CNTs, and particularly clear with high purity SWCNTs.

The spectrum also has a very strong D peak, at 1351 cm^{-1} which corresponds to phonon scattering from defects in the crystalline like CNT lattice. When there is a defect in the CNT structure, dislocation, Frenkel pair, or kink in the CNT with

a non-ideal bonding structure, this shows up in the D peak. Correspondingly, the stronger the D peak is in any SWCNT spectrum, the more defects are present in the CNTs being observed.

The G peak is located at 1596 cm^{-1} which corresponds to the high energy mode in the CNTs. This indicates the phonon interactions down the long axis of the CNTs. There is also a G' peak located at approximately 2696 cm^{-1} . This peak is the 2nd order Raman mode of the D peak, which shows the interaction of 2 phonons, or phonons coupled with photons.

2.11 Silicon damage from electrons

The effect of electron radiation on silicon is used as a baseline to determine the relative radiation sensitivity of CNT thin films over silicon based technology. Wertheim *et al.* reported a linear relationship between damage and fluence with 500 keV electrons at a fluence from $5 \times 10^{17} \text{ e}^-/\text{cm}^2$ to $1 \times 10^{18} \text{ e}^-/\text{cm}^2$ incident on n type silicon producing a 20% reduction in mobility.[43]

Interest also emerged in correlating the damage produced by various types of radiation and in operating devices in radiation environments, including space. The non-ionizing energy loss rate can be calculated analytically from first principles based on differential cross sections and interaction kinematics. NIEL is that part of the energy introduced via elastic (both Coulombic and nuclear) and nuclear inelastic interactions that produce the initial vacancy-interstitial pairs and phonons (e.g., vibrational energy). NIEL can be calculated for electrons, protons, neutrons, etc., using the following analytic expression that sums the elastic and inelastic contributions:

$$NIEL = \left(\frac{N}{A} \right) [\sigma_e T_e + \sigma_i T_i] \quad (15)$$

where σ_e and σ_i are total elastic and inelastic cross sections, and T_e and T_i are elastic and inelastic effective average recoil energies corrected for ionization loss, N is Avogadro's number, and A is the atomic weight of the target material. Note that the units for NIEL, typically $\text{MeV}\cdot\text{cm}^2/\text{g}$, are the same as those for stopping power or linear energy transfer (LET) that describe energy transfer by ionization and excitation per unit length.[44]

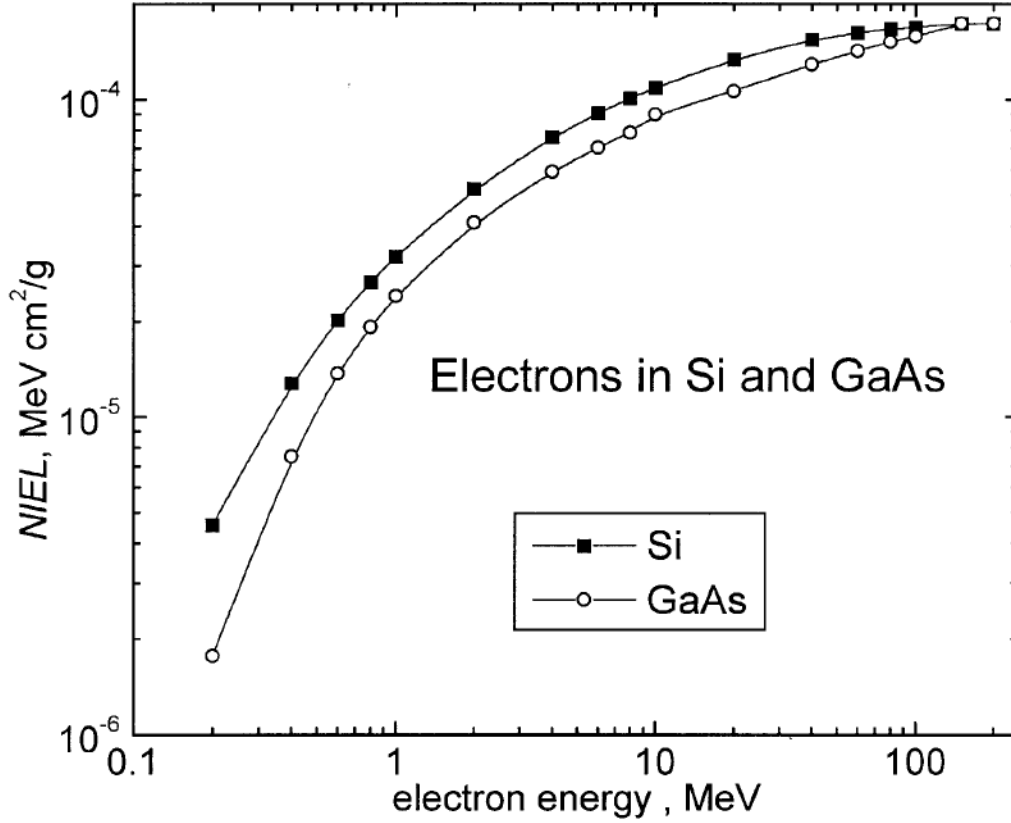


Figure 18. Plot of non-ionizing energy loss of electrons in silicon and gallium arsenide. Electrons at 500 keV produce a NIEL of $1 \times 10^{-5} \text{ MeV}\cdot\text{cm}^2/\text{g}$. Reproduced with permission from Akkerman *et al.*[33]

The Akkerman-Barak method of calculating NIEL that is used in this research was also applied to silicon and gallium arsenide. Figure 18 shows the NIEL calculations of electrons in silicon. [33] This chart, when compared with Figure 13 show that SWCNTs have a similar value of NIEL. The low density and three dimensional open

geometry of CNTs change the threshold for knock-on damage. Silicon is generally quoted as having a threshold energy for displacement of 21 eV, while most literature quotes 16.9 eV for the threshold energy of CNTs.

2.12 Previous Research

There has been a significant amount of research in CNT physics, devices, and radiation effects. The primary research for this thesis follows that of Cress[2], [7] and Rossi[3]. These papers use the same material as this research, with similar CNT fabrication techniques, along with Raman spectroscopy and temperature dependent conductivity. The idea of plotting the D/G and D/G' peak intensity ratios as a function of radiation fluence came directly from these published papers.

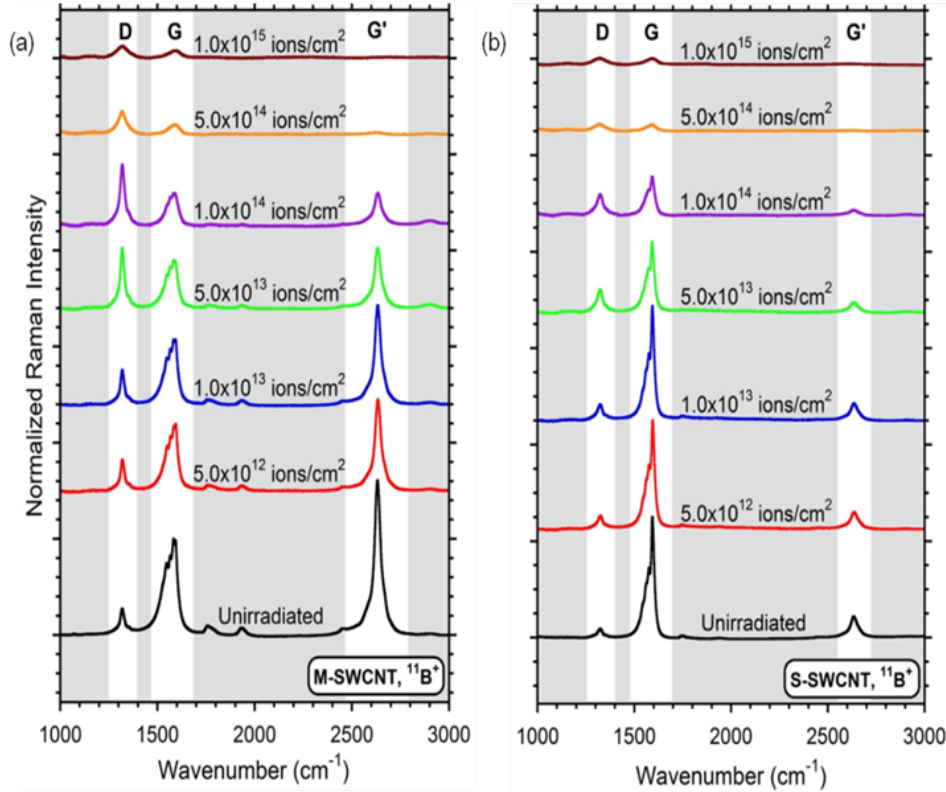


Figure 19. Results of Raman spectra changes with ion fluence on SWCNT thin films. Reproduced with permission from Rossi *et al.*[3]

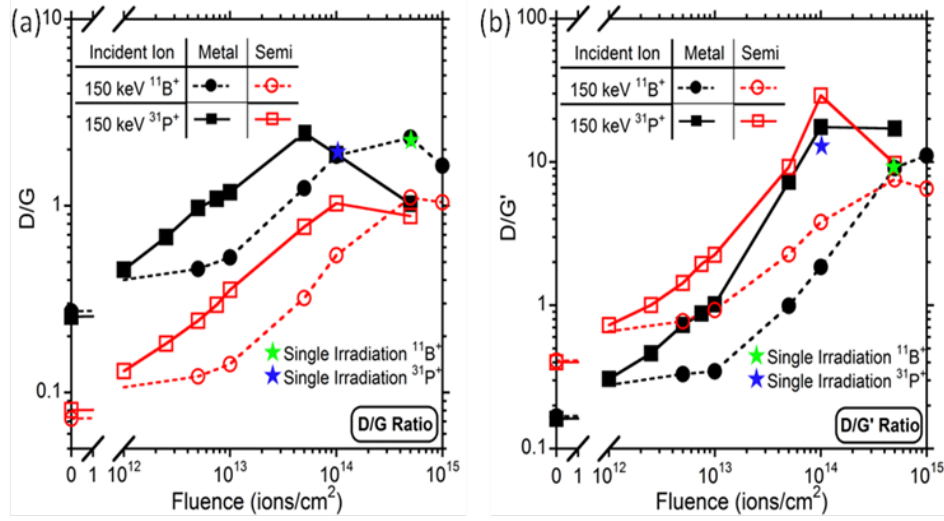


Figure 20. Results of an ion study with SWCNT thin films plot of Raman Spectra $\frac{D}{G}$. This figure shows the damage to SWCNTs created by ions at different fluences by comparing the ratio of the peak intensity of the D peak, with the peak intensity of the G peak in a Raman spectrum. As CNT damage increases, the ratio of the D to G peaks will correspondingly increase. Reproduced with permission from Rossi *et al.*[3]

The figures in this section demonstrate the expectations for this research. The primary difference is the particle used for irradiation. For Cress *et al.*, alpha particles were used in the irradiations. The resulting changes in conductivity are shown in Figure 21. Rossi *et al.* used boron and phosphorous ions to irradiate the CNT thin films. These results are shown in Figures 19 and 20. One of the most important equations to come from the Rossi *et al.* paper is the calculation of displacement damage dose (DDD) in MeV/g. DDD is described as a measure of the total energy per unit mass imparted by a given fluence of ionizing radiation (including electrons, ions, neutrons, and energetic photons) and is representative of the number of Frenkel-pairs produced in a material during irradiation. The DDD includes the energy lost in the production of vacancies by both the primary particle strikes and the ejected primary knock-on atoms, but does not include the energy lost due to ionization or the production of lattice vibrations in the form of heat. DDD is a useful unit in that it is independent of the source of radiation damage and can be used to compare the

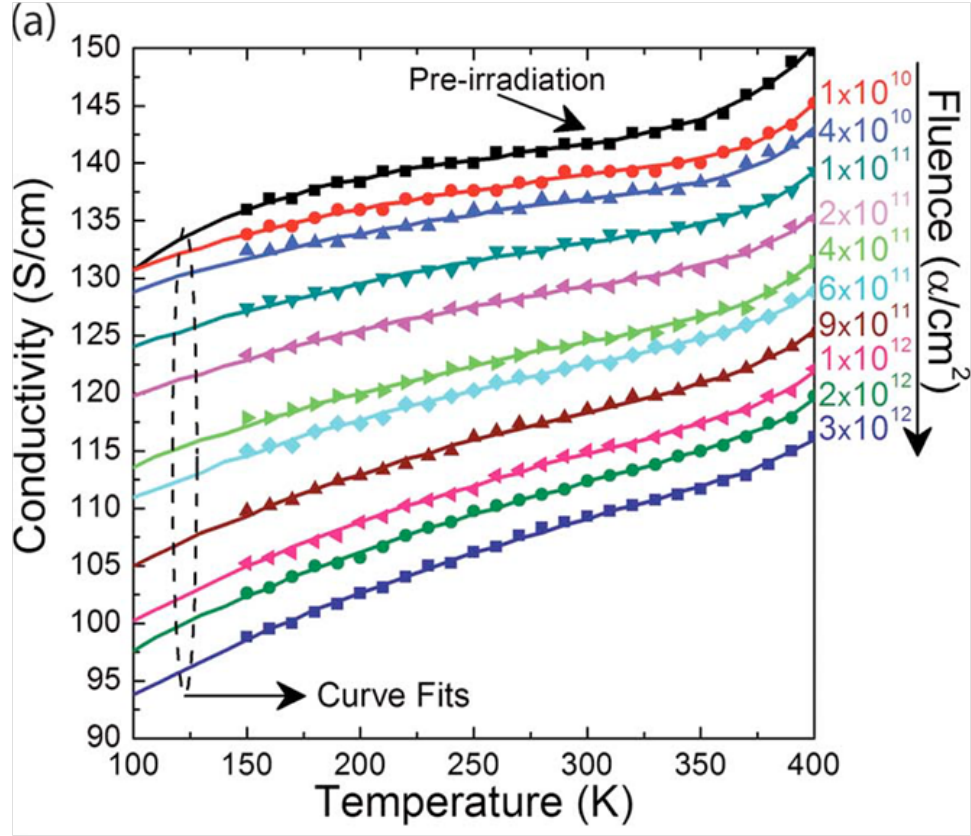


Figure 21. Results of temperature dependent conductivity as it changes with ion fluence on the sample. Reproduced with permission from Cress *et al.*[2]

rates of degradation with other materials.[3] In a simple form, the DDD results from multiplying the NIEL by the fluence of the incident radiation, in this case electrons. Rossi shows that significant damage is evident on similar CNT networks at a DDD of 2×10^{15} MeV/g using boron and phosphorous ions. A significant goal of this research is to correlate the amount of electron radiation damage to changes in the Raman spectrum and sheet resistivity. This is shown here by Rossi in Figure 22.

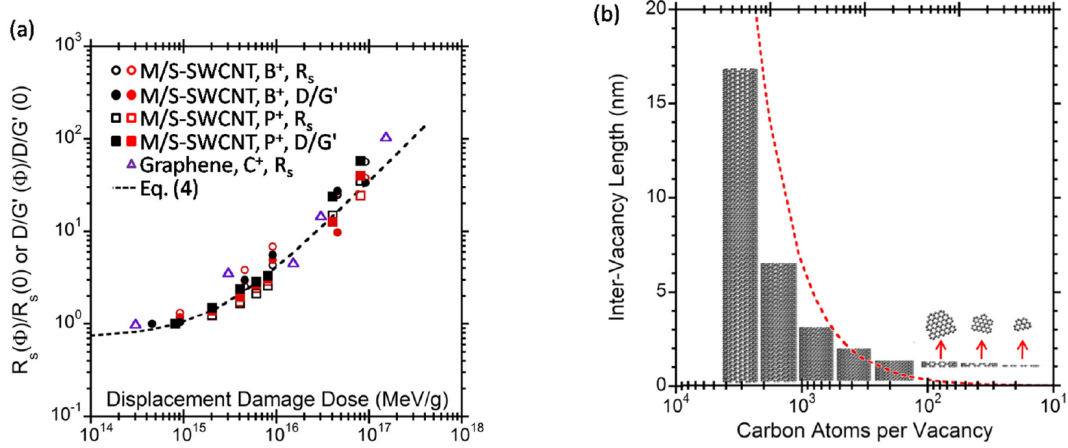


Figure 22. The left figure (a) represents ion radiation results from Rossi *et al.* showing the changes in D/G, D/G', as well as R_s as a function of DDD, which is calculated from particle fluence. (b) shows the calculated average CNT tube length without vacancies caused by damage as a function of DDD. Reproduced with permission.[3]

III. Experiment

3.1 Purpose

The objective of this research is to investigate the electrical properties of single walled carbon nanotube thin films before and after high fluence electron irradiation using Raman spectroscopy and temperature dependent Hall measurements. The thin films are described first, in order to gain an appreciation for the steps that went into the fabrication process. The experimental equipment is described next, followed by the methods and procedures followed throughout the different experiments that comprise this body of research.

3.2 Thin Films

The carbon nanotube thin films that are used throughout this research were fabricated at the NanoPower Laboratory of the Rochester Institute of Technology. Separated metallic and semiconducting SWCNTs created from the arc discharge method were purchased from NanoIntegris, and dispersed via ultrasonication in sodium dodecyl sulfate and sodium deoxycholate, respectively. Ultrasonication separated the SWCNT bundles to form individualized SWCNTs stabilized by surfactants in solution. This ultrasonication is required because the CNT bundles tend to bind together due to the strong Van der Waals forces between the carbon nanotubes. The samples were ultracentrifuged to remove the remaining carbonaceous impurities and metal catalyst particles from the bundled SWCNTs. The processing steps result in isolated, suspended, 99% pure single walled CNTs. The top 80% of the suspension was processed into thin-films on silicon substrates with a 300 nm silicon dioxide layer for electrical isolation between the silicon and the CNT thin films. The CNT dispersion was vacuum filtered onto a mixed cellulose ester membrane (MCE, 0.1 μm pore-size)

to achieve a SWCNT coverage of $10 \frac{\mu g}{cm^2}$. A 10×10 mm section was cut from the center of the SWCNT coated MCE membrane, transferred face down onto the silicon substrate, and the MCE membrane was dissolved in acetone. This process is shown graphically in Figure 23. The samples were oxidized for 2 hours at 300 °C to remove

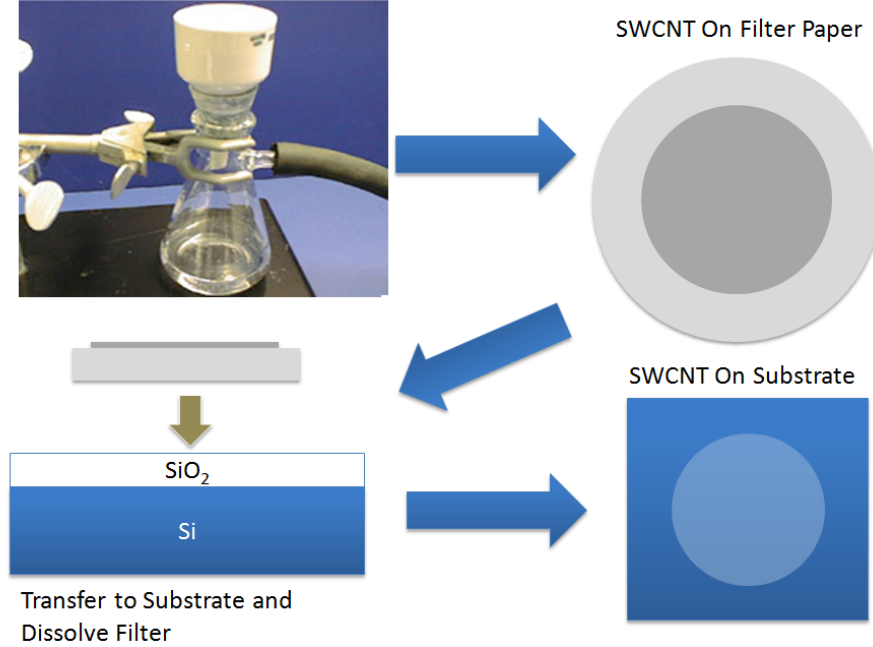


Figure 23. Illustration of the fabrication technique used to create CNT thin films. Micro pore vacuum filtration to remove the CNTs from their surfactant solution is shown in the top left. The filter membrane is shown on the top right with the CNTs deposited on it. The filter membrane is then pressed down onto the silicon substrate, and acetone is used to dissolve the membrane. The bottom right graphic depicts the CNTs deposited on the substrate ready for further processing. Reproduced with permission.[2] [3]

the residual MCE membrane and moisture.

The Raman samples were not trimmed down. The entire membrane was placed down on the silicon substrate. The Hall samples were trimmed to squares with 7 mm sides. Palladium contact pads (500 nm thick) were deposited through a shadow-mask onto each of the four corners of the SWCNT thin films using electron beam evaporation as shown in Figure 24. The contact pads extend onto the silicon substrate

to allow for consistent electrical connection during multiple radiation/characterization iterations. The Pd thickness is sufficient to maintain a constant contact resistance throughout the thermal cycling and irradiation. [3]

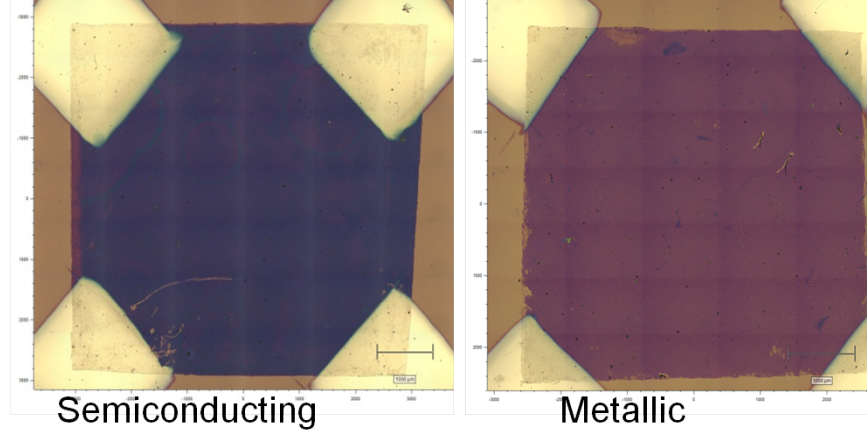


Figure 24. Optical photograph of the SWCNT thin films for Hall measurements, both 7 mm square. The semiconducting thin film is on the left, while the metallic thin film is on the right. The corner contacts are made from 100 nm of palladium deposited over the CNTs on a silicon dioxide layer grown over silicon.

The thin films used in this research appear on an Atomic Force Microscope image as a random matrix of single walled CNTs as shown in Figures 25 and 26. These figures show the randomness of the CNT network in the thin films. Figure 25 represents a 5 μm square atomic force microscope image of a low density network of the same SWCNT type used in this research. Figure 26 is an atomic force microscope image of the actual samples used in this research that have a much higher density and thickness than the network in Figure 25. The conduction pathways are dependent on many factors, including the density of the CNT mat, and the amount of orientation in the CNTs.

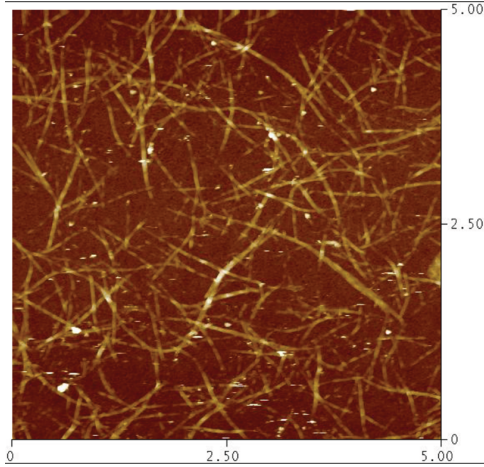


Figure 25. Atomic force microscopy image of medium density single walled carbon nanotubes on a silicon substrate to illustrate the random nature of the CNT thin films used in this research. The scale is in microns.

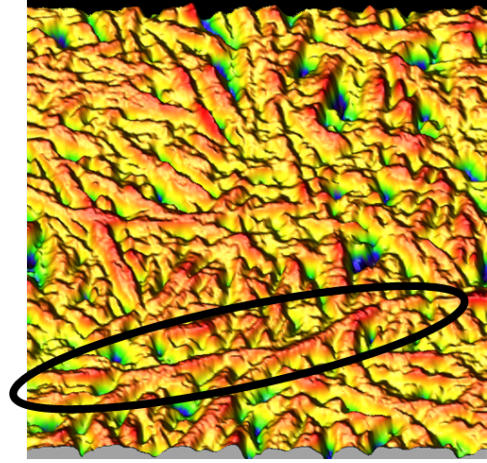


Figure 26. Atomic force microscope 3 dimensional representation of the semiconducting sample 127B. The oval highlights an average CNT with an approximate length of $1\text{ }\mu\text{m}$ and an average diameter of 1.5 nm .

3.2.1 Raman Spectroscopy

All Raman spectroscopic measurements were done on a Renishaw inVia Raman microscope located at the Air Force Research Laboratory Sensors Directorate at Wright Patterson Air Force Base. Several individual spectra were taken initially on each sample to determine the ideal laser wavelength to use, as well as optimizing the other parameters such as objective, laser power, and spectral range from different gratings with static scans. There were 4 lasers available: 488 nm, 514.5 nm, 633 nm, and 785 nm wavelengths. The 488 nm laser produced good resolution for a single point run, but tended to burn the samples, locally heating the CNT thin films to the point where the carbon disassociated and ablated off the substrate, even below 50% laser power. The 633 nm and 785 nm lasers both produced spectra that lost some of the features most often associated with high quality Raman measurements in published scientific literature such as the G^- peak and overall they had lower intensity for the same amount of time on the sample.[45] The three laser line spectra in Figure 27 shows the spreading of the 633 nm spectrum relative to the 514.5 nm

spectrum as well as the lower relative intensity for the same time integration. There

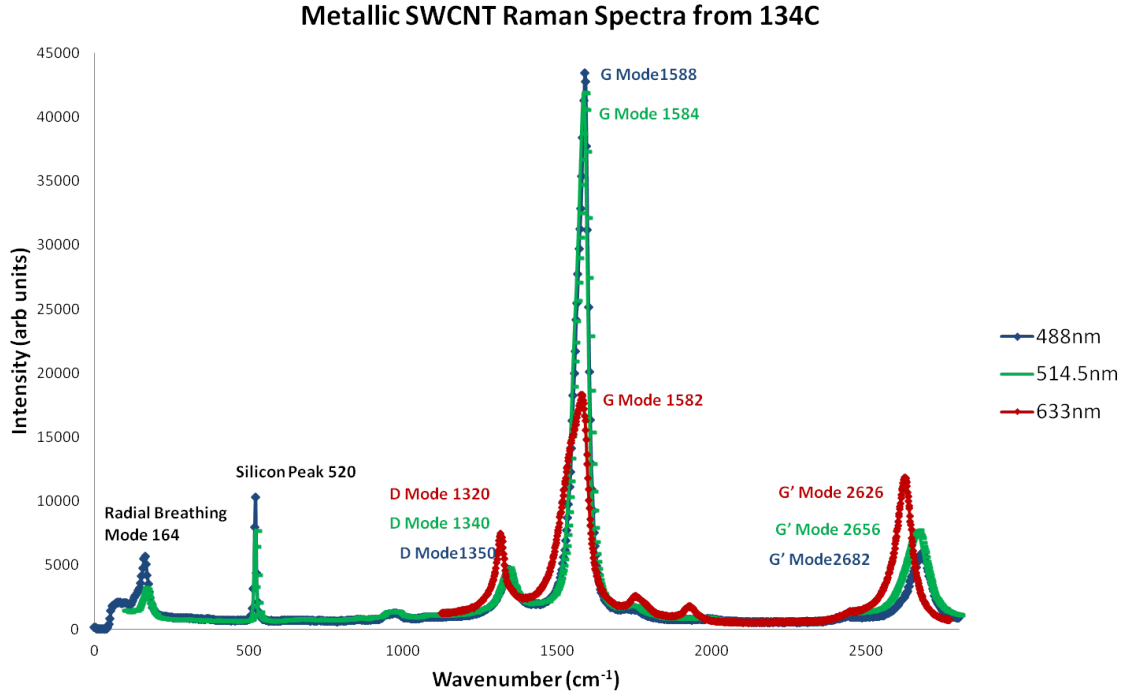


Figure 27. Raman spectral plot of 3 laser lines used on metallic single walled carbon nanotube thin film. This shows the D peak, the G peak, and G' peaks with three different laser wavelengths available on the Raman system. The shift in the D and G' peaks with wavelength are due to energy dependent defect mode phonon interactions.

is also an incident wavelength specific shift in the resulting Raman spectrum shown in Figure 27. This spectral shift is evident primarily in the D and G' peaks due to the defect mode phonon interactions being a function of the incident laser wavelength. This phenomenon is explained in detail by Dresselhaus *et al.*[40] The spectrometer uses a grating to separate the return signal into individual frequencies before being read by the Raman detector. This grating is similar to a quartz prism breaking up white light into individual color components. For this research, the 1200 lines/mm grating produced the widest spectrum while using the 514.5 nm laser on a static scan. When using different gratings, a higher line/mm grating such as the 1800 lines/mm grating gives slightly better spectral resolution, but significantly narrows the spectral

range. In order to capture most of the available spectrum in the highest resolution possible with a static scan, the 1200 lines/mm grating was chosen for many of the spectra taken. This combination of settings reduced spectral statistical error in the final measurements while producing very reliable spectra.

All measurements were therefore made with a 514.5 nm (green) laser for the excitation, at between 50% and 100% laser power (10 mW - 21 mW) using a 50X microscope objective lens at room temperature and ambient humidity. The microscope was set with a 20 μm slit width on the high confocal setting with either a 1200 lines/mm or a 1800 lines/mm grating on the spectrometer. The spectra are centered between 1600-2100 cm^{-1} with a spectral resolution of $\pm 1.5 \text{ cm}^{-1}$ and a spatial resolution of 1 μm through the objective lens.

A representative spectrum from a metallic SWCNT thin film is shown in Figure 17 using the typical settings described above. After the initial pre-irradiation characterization of each sample, it was taken to the linear electron accelerator facility.

3.2.2 Dynamitron

The Dynamitron linear electron accelerator was designed and manufactured by Radiation Dynamics Incorporated (RDI) in 1971 for the Air Force Research Laboratory. It has undergone a series of upgrades since its initial construction including new high voltage components, and solid state electronics in 1996 to replace the vacuum tubes that were originally in the design. This accelerator uses high voltage radio frequency antennas to multiply the voltage down the tube in order to accelerate the electrons emitted from the tungsten filament at the back end of the accelerator column shown in Figure 28.

All of the components are housed within a large pressure tank which holds the inert gas sulfur hexa-fluoride (SF_6) at 95 psi tank pressure shown in Figure 29. The

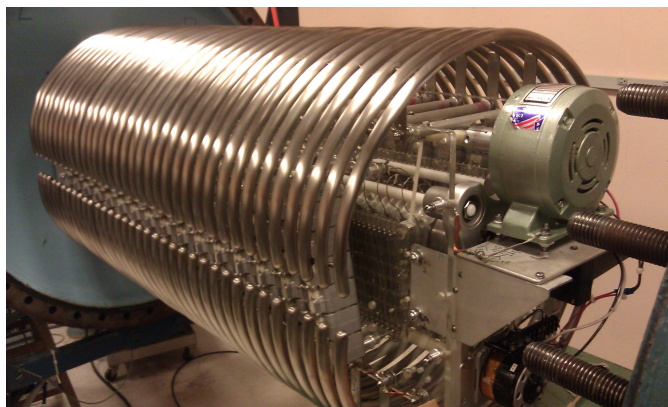


Figure 28. Image of the working parts of the Dynamitron electron accelerator showing the generator, the RF antennas surrounding the acceleration column, and the banks of diodes under the RF antennas.

SF₆ serves to suppress arc discharges from the RF antennas while operating at high voltages.



Figure 29. Image of the large blue tank housing the working parts of the Dynamitron accelerator, including the tungsten filament, RF antennas, and diode banks. The tank is filled with SF₆ at a pressure of 95 psi to minimize arcing in the accelerator.

The accelerator column is kept at the lowest pressure possible which is currently 5×10^{-7} torr to minimize the ambient particles which would interact with the electron beam and cause down scattering of the electrons. This electron beam is approximately 2 mm in diameter with a Gaussian profile, which is steered down the tube and rastered over a sample using a Lissajous pattern through an aluminum collimator using strong

electromagnetic steering coils. The sample is placed on a horizontally mounted stage that is plumbed for cold water or liquid nitrogen. Cold water, as is typically used through a closed loop water chiller, is used to keep the heat buildup caused by the energetic electrons impacting the sample and copper cold head from damaging the sample. The collimator used for these irradiations shown in Figure 30 was fabricated from a block of $\frac{5}{8}$ " aluminum stock with a 7 mm diameter hole in the center serving as the collimator. The current measured at the sample stage through an analog current

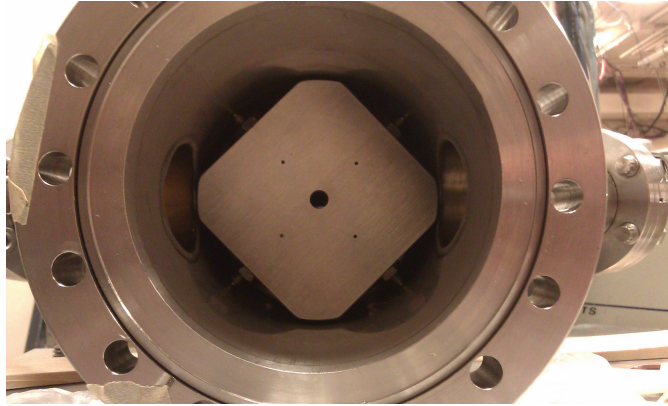


Figure 30. Image of the 7mm diameter aluminum collimator used in all irradiations as mounted in the electron beam column.

integrator allows calculation of the flux of electrons incident on the sample. This is calculated in Appendix D.

3.3 Hall System

There were three different Hall systems used throughout this research. The primary system used was the Lakeshore temperature dependent Hall system located at AFRL in the Sensors directorate. A sample is connected using thin teflon coated aluminum wires soldered to the palladium pads on the samples with pure indium solder using a soldering iron at ≈ 800 °C. This system was set up to initially cool a sample down to liquid nitrogen temperature (77 K) before starting the measurements.

Each measurement run took approximately 8 hours, and the Hall characteristics were measured every 10 K up to room temperature. Both 134D, the metallic sample, and 134H, the semiconducting sample were measured overnight before irradiation by the electron beam. The metallic sample was measured with a 2 mA current for the temperature dependent Hall measurement, while the semiconducting sample was measured with a 1 mA current. Prior to installing the sample on the Lakeshore Hall system, an initial characterization measurement was made using an Accent HL 5500 Hall system at ambient temperature and pressure. The results of this are shown in Table 1. The general values displayed in Table 1 were repeated with multiple other

Table 1. Table of the initial Hall measurements taken on an Accent HLS5500 Hall system before irradiation.

Pre-Rad	Hall	Measurements	2 mA	0.486 T
Sample	Rs	Ns	Mobility	Conductivity
134D	621.3 Ω/sq	$8.63 \times 10^{16} / \text{cm}^2$	0.116 $\text{cm}^2/\text{V-s}$	160.95 S/cm
134H	548.6 Ω/sq	$2.70 \times 10^{16} / \text{cm}^2$	0.421 $\text{cm}^2/\text{V-s}$	182.30 S/cm

systems, including the Keithley 4200 semiconductor measurement system, and the Ecopia HMS 3000 which is described later.

3.4 Setup and Design of Experiment

The experiment was conducted in four primary phases: Pre-irradiation measurements, electron irradiation, followed immediately by post irradiation measurements. A fourth phase was added to make in-situ Hall measurements in vacuum to discover the nature of adsorbents on the CNT thin films. Both the Raman study and the Hall study had pre- and post-irradiation Raman measurements on each thin film in order to separate the damage to the individual CNTs from other effects.

3.4.1 Raman Study

The Raman study was conducted with circular thin films specifically designed for the purpose of irradiating different spots with different fluences of electrons to determine the amount of damage sustained by the SWCNT thin films as a function of electron energy and fluence. Figure 31 shows an optical microscope image of the

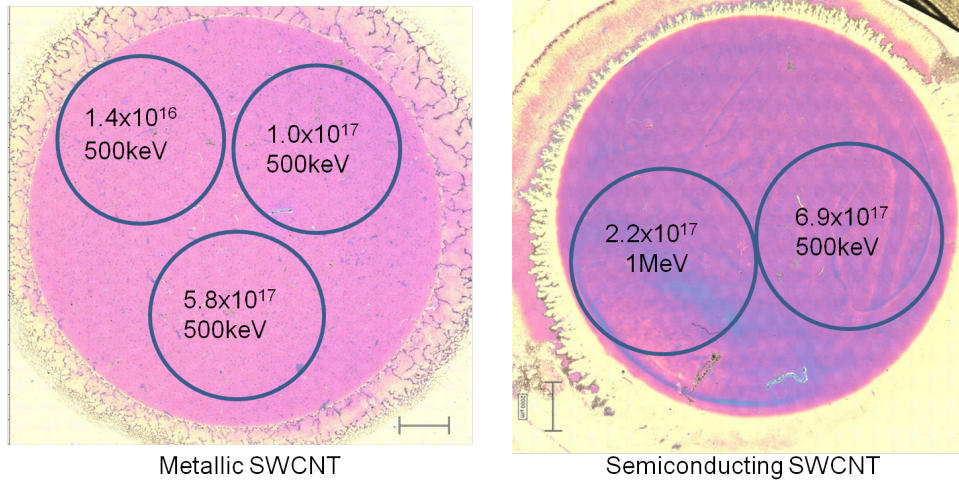


Figure 31. Thin film Raman samples with representative circles indicating areas of electron irradiation with corresponding fluence and energy.

thin films used in this study, with the circles indicating the fluence, electron energy, and relative position of the irradiated spots. All of the spots had a diameter of approximately 7 mm because of the 7 mm diameter collimator that was used.

With the Raman study, the 2.5 cm diameter CNT networks were measured with more than 2500 individual spectral acquisitions spread uniformly over the sample with each measurement separated by a horizontal and vertical distance of 300 μm .

All of the resultant Raman spectra were analyzed by subtracting the background which was relatively small for each spectrum, followed by normalization to the G peak of each spectrum for plotting or comparison. Normalization was required because experimental error is introduced from the environment, different laser power settings,

and the differences in focal length on samples that were not perfectly level. This is one of the reasons why the D/G and D/G' peak intensity ratios are used in CNT research as opposed to absolute values, as ratios give a consistent metric for analysis of the damage of individual CNTs.

3.4.1.1 Metallic SWCNT Raman Study

The pre-irradiation Raman maps were collected a week before the irradiations. The specific setup for this metallic Raman sample, 127A, was an 1800 line/mm grating at 50% laser power with the spectra centered at 2000 cm^{-1} using a 20x objective with an aquisition time of 5 sec. For the metallic SWCNT thin film, all three spots were irradiated in order of increasing fluence before measuring the post-irradiation Raman spectra. Prior to irradiation, a test spot is irradiated on a piece of transparency film which shows the exact beam size and location. The sample is mounted on the steel cold head as shown in Figure 32 using vacuum grease to adhere the sample to the head, and then shielded with a piece of aluminum foil folded multiple times to achieve a thickness of $\approx 1\text{ mm}$. This setup is shown in Figure 33. The foil is there to ensure only the desired area is electron irradiated. The simulations and calculations for determining the amount of aluminum needed to shield the 500 keV electrons are presented in Appendix C. The first irradiation was $1.4 \times 10^{16} \frac{e^-}{\text{cm}^2}$, followed by breaking the vacuum, repositioning the sample on the cold head, and then resealing the chamber for a 3 hour pump down to the operating pressure of 9×10^{-7} torr. The next spot was irradiated to $1.0 \times 10^{17} \frac{e^-}{\text{cm}^2}$ followed by the same repositioning procedure to irradiate the third spot to $5.8 \times 10^{17} \frac{e^-}{\text{cm}^2}$. This sample was taken immediately to the Raman spectrometer following the final irradiation using a full map function with approximately 3300 individual spectra taken with $300\text{ }\mu\text{m}$ spacing.

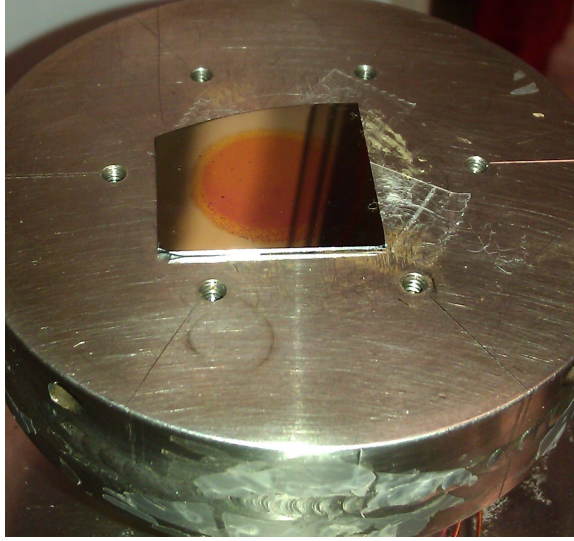


Figure 32. Representative digital photo of the experimental setup for the Raman study on the Dynamitron electron beam accelerator. This image shows sample 127A, with metallic SWCNTs in a thin film on Si/SiO₂, mounted on the cold head used in the irradiation study.

3.4.1.2 Semiconducting SWCNT Raman study

The semiconducting SWCNT thin film, 127B, was measured using an 1800 lines/mm grating at 50% laser power with the spectra centered at 2050 cm⁻¹ using a 50x objective with an acquisition time of 2 sec using focus track for every spot. Focus track requires almost a minute per calibration, so with the 3000 measurements taken the pre- and post-irradiation Raman measurements took over 48 hours and were run over weekends. This sample was irradiated in two different spots, with two different electron energies. This was done because the Dynamitron was not able to provide sufficient current at the target due to mechanical issues, and partially because the low fluence irradiations on the metallic sample showed very little change in the Raman spectra in the initial analysis. The first irradiation was at 500 keV to a fluence of $6.9 \times 10^{17} \frac{e^-}{cm^2}$ over a period of 8 hours, with a very low current which produced a low flux of electrons on the CNT target. The maximum current available was under

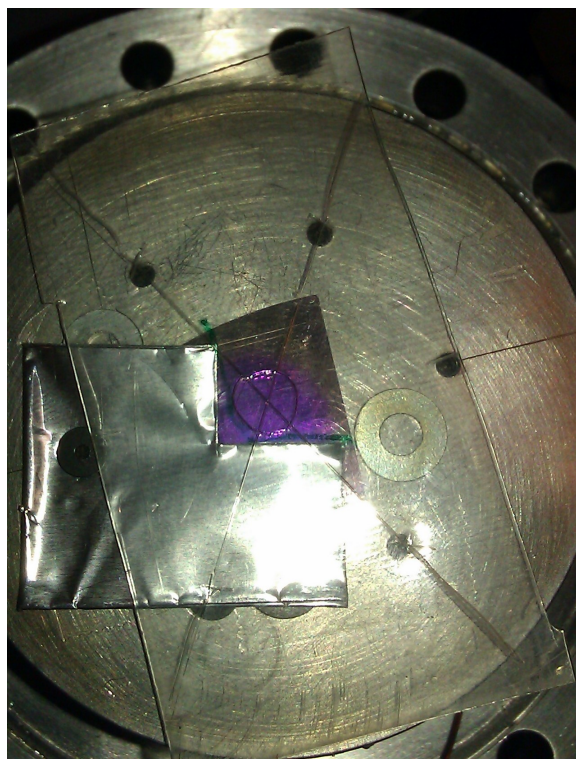


Figure 33. Representative digital photo of the experimental setup for the Raman study on the Dynamitron electron beam accelerator. This image shows sample 127A, with metallic SWCNTs in a thin film on Si/SiO₂, mounted on the cold head with an aluminum shield to isolate the other quadrants on the sample in the irradiation study.

3 μ A. A photograph of the sample immediately following irradiation and breaking vacuum is shown in Figure 34.

This spot shown in Figure 34 is interesting because of the water condensation. It is known and published that CNTs are naturally hydrophobic, which can explain the water beading up on the surface of the un-irradiated part of the sample. The irradiated circle appeared to not allow any condensation on it. Initially this was believed to be residual heat from the electron irradiation, but after several days, the sample still did not allow any condensation on the surface. After some review of published literature and further testing, this is believed to be primarily an optical change within the CNT thin film. Further water testing revealed that large amounts of water bead up on the surface, but small droplets (i.e. breathing on the sample)

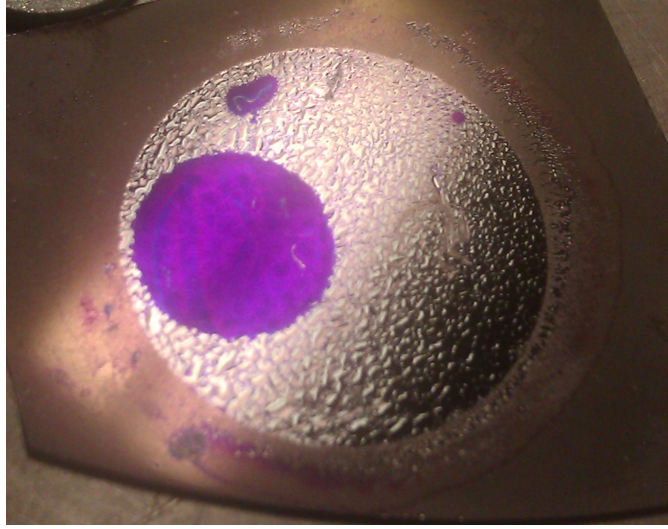


Figure 34. Photograph of the semiconducting Raman sample immediately following radiation and breaking vacuum while the sample is still mounted to the cold head. This clearly shows an area where water is adsorbed on the sample, corresponding to the area of irradiation at $6.9 \times 10^{17} \frac{e^-}{cm^2}$

only bead up on the unirradiated area as the smaller water drops are being adsorbed onto the irradiated CNT surface. This is likely a change of the CNTs to a hydrophilic rather than fully hydrophobic state. These results are still evident after a 90-day room temperature anneal.

The electron energy in the second irradiation was increased to 1 MeV with a total fluence of $2.2 \times 10^{17} \frac{e^-}{cm^2}$. This took a similar amount of time as the previous irradiation because of significant leakage current in the Dynamitron forcing it to be operated at an extremely low current. Following this irradiation, Raman and AFM measurements were taken. There was no substantial findings in this study, but some of the images produced are included in Appendix B.

3.4.2 Hall Measurements

The Hall measurements were conducted in a Van der Pauw configuration to measure the resistivity, mobility, carrier concentration, and Hall coefficient of the thin film samples. This was achieved easily because of the vapor deposited palladium pads that

were placed over the CNT thin films during fabrication at RIT and shown in Figure 24. All of the Hall measurements were made ex-situ. The samples were measured locally using the Keithley 4200 SMU, as well as the Ecopia Hall Measurement System (HMS) 3000 using a 0.54 Tesla magnet. The samples were taken to the AFRL Hall measurement lab in the Sensors directorate where they were measured with a room temperature system using a 0.54 T magnet before placing them into the Lakeshore temperature dependent Hall measurement system which uses a 0.58 T magnet. Both the room temperature measurements and the temperature dependent Hall measurements yielded results on the same order of magnitude as the measurements on the Ecopia and Keithley. These results gave great confidence in all of the measurements, and the experimental setup; essentially getting the same results with four different Hall measurement systems within experimental error.

After making the pre-radiation Hall measurements on both the semiconducting and the metallic thin films, both were irradiated on the Dynamitron to different fluences.

3.4.2.1 Semiconducting Thin Film

The CNT thin films used for the Hall study, 134H, were characterized with Raman measurements using both 514.5 nm and 633 nm lasers. The 514.5 nm laser had further spectrometer settings of 1200 lines/mm grating, 50% power, with a spectral center of 1600 cm^{-1} , 50x objective for 2 seconds of laser acquisition time. The purpose for using the 1200 line/mm grating was to capture the entire available spectrum, from 0 to 2800 cm^{-1} . The 1200 lines/mm grating allows a wider spectral range than the 1800 lines/mm grating, while sacrificing some resolution to achieve this. These measurements were done in three parts. After orienting the sample in the spectrometer, calibration using the internal silicon reference, and focusing the objective lens on the

sample, the sample was measured along a horizontal line. A vertical line was also measured, from edge to edge of the sample, followed by a $100\text{ }\mu\text{m}$ box in the center of the sample using $2\text{ }\mu\text{m}$ spacing between spectral acquisitions.

The semiconducting thin film was irradiated after completing the Raman measurements. This irradiation was completed at 500 keV electrons with the highest current on the target that was possible under the operating conditions of the Dynamitron at the time. The maximum current that could be run was approximately $2\text{ }\mu\text{A}$ measured at the current integrator on the target stage. The total fluence after approximately 7 hours of steady irradiation was $2.5 \times 10^{17} \frac{e^-}{\text{cm}^2}$.

Following the irradiation, the sample was taken directly to the Hall lab at AFRL for immediate set up in the machine. There was approximately one hour between ending the irradiation, and beginning the overnight Hall measurement run.

After the Hall measurement was complete, the Raman measurements were conducted using the same settings as the pre-irradiation Raman measurement approximately 12 hours after the irradiation.

3.4.2.2 Metallic Thin Film

The pre- and post Raman measurements used the same settings as the semiconducting films for the metallic sample 134D. The Raman spectrum was measured first, followed by pre-irradiation temperature dependent Hall measurements. The metallic thin film was then irradiated after the semiconducting thin film. The goal of the research was to attain the same fluence for both samples. After $2.5 \times 10^{16} \frac{e^-}{\text{cm}^2}$, the electron beam failed due to filament burnout. The same post-radiation procedure was used for the semiconducting sample. The temperature dependent Hall measurements were collected immediately following irradiation, followed by Raman measurements the day after the irradiations.

3.4.3 Vacuum Study

After the primary objective of measuring the effects of the electron radiation on the CNT thin films was accomplished, a subsequent study was undertaken to understand the effects of pressure and temperature on the resistivity of these thin films. The theory presented in Chapter II suggests a significant resistivity dependence on temperature, pressure, and ambient air molecule adsorption.

This study started with a set of unirradiated samples, 134F (metallic) and 134J (semiconducting). These samples were placed in the Ecopia HMS 3000 Hall measurement system on a specially designed pin board shown in Figure 35. The Ecopia

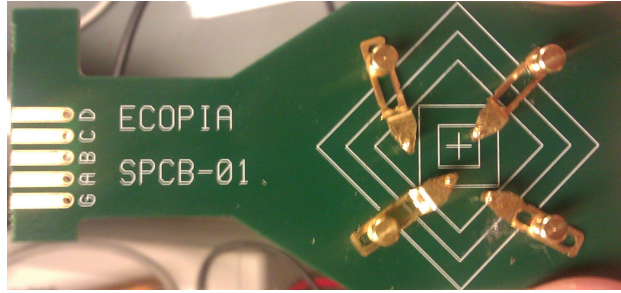


Figure 35. EcopiaHMS 3000 pin board used to measure room temperature and liquid nitrogen Hall resistivity on samples.

system uses a 0.54 Tesla magnet that is manually switched during measurements to provide the opposite fields necessary to subtract hysteresis in the measurements. Both samples were measured at room temperature first. Each sample was measured 15 times, with 5 measurements using $100.0\ \mu\text{A}$, 5 measurements using $500.0\ \mu\text{A}$, and 5 measurements using $1.0\ \text{mA}$.

After these measurements, the Ecopia system was filled with liquid nitrogen (LN), and kept filled throughout all of the subsequent measurements. Each sample was kept submersed in pure LN throughout 15 measurements with the same applied currents as before: $100.0\ \mu\text{A}$, $500.0\ \mu\text{A}$, and $1.0\ \text{mA}$.

This provided a good comparison to the other samples that were measured and

irradiated. The results are reported in Chapter IV. In general, the results were consistent with published literature, and measurements made on the previous Hall samples.

Following this baseline study, each sample was wired using pure indium, with a soldering iron set to 800 °C. The samples were then installed on the cold head of the electron beam. The electron beam was still not functional, but the vacuum system was maintained at 1×10^{-6} torr as shown in Figure 36. The samples were wired



Figure 36. Experimental setup for Hall vacuum study with the sample mounted with thermal paste inside of a 1.0 T toroidal magnet placed on the copper cold head.

into the cold head apparatus through the vacuum feed-through. A fixed 1.0 Tesla

toroidal magnet was installed over the samples. An IV plot is taken on each sample to characterize the experimental setup.

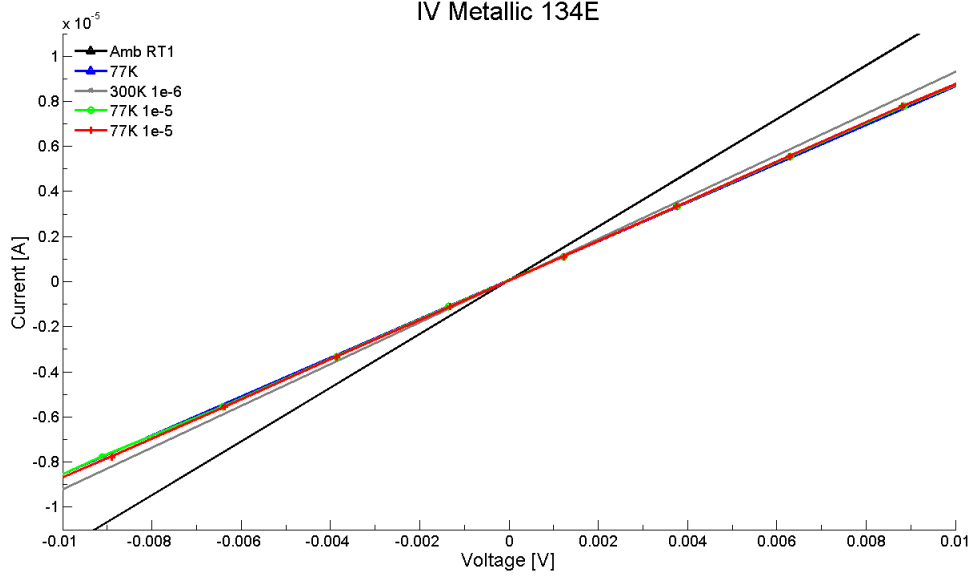


Figure 37. IV curves taken with the Ecopia system while performing Hall measurements on the cold head with the metallic sample 134D. This shows both ambient temperature and pressure, along with 77 K measurements at ambient pressure and in vacuum. The results show that with a metallic CNT thin film, the 77 K and the pressure both serve to add resistance to the sample, but the pressure does not affect the metallic sample as much as the semiconducting sample shown in Figure 38.

Once each sample was properly mounted, the cold head was attached to the vacuum system. Initially, 15 measurements were taken in ambient pressure, at room temperature, using the same applied currents as used previously to allow a direct comparison. After the ambient pressure measurements, the load lock was pumped down to 1×10^{-5} torr. Measurements were taken at this pressure. The IV curves are shown in Figures 37 and 38. The load lock was then opened to the main vacuum system, and allowed to equilibrate at 1×10^{-6} torr followed by the same measurements. On the metallic sample, liquid nitrogen was available for use, so within the 1×10^{-6} torr vacuum, LN was pumped through the cold head for 30 minutes. Fifteen measurements were taken with sample 134F at 77 K in the vacuum.

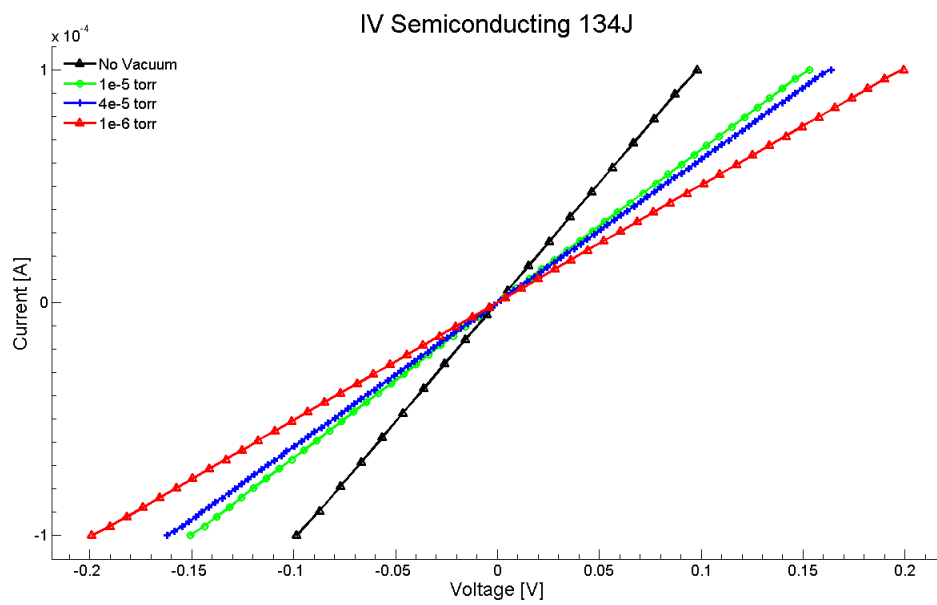


Figure 38. IV curves taken with the Ecopia system while performing Hall measurements on the cold head with the semiconducting sample 134H. This shows the sample becoming more resistive as the pressure is decreased.

IV. Results and Analysis

4.1 Raman Study

The Raman study allowed the determination of damage effects in the individual CNTs as measured by Raman spectroscopy. The results of this study showed a direct correlation between electron fluence and the relative increase in the D phonon peak on a spectrum normalized to the G peak intensity. This correlated with the results described at the end of Chapter II as reported by Rossi *et al.* The results from both the metallic and semiconducting Raman samples served as a basis for the Hall study. It was important to determine the minimum amount of electron fluence to cause noticeable damage in the CNT networks, as well as allowing quantification of the change in D/G and D/G' peak intensity ratios.

4.1.1 Metallic Film

The metallic SWCNT thin film was characterized by Raman spectroscopy as described in Chapter III and showed a very clear spectrum that was characteristic of extremely pure free standing single walled carbon nanotubes. This facilitated direct observation of the variation of the D/G and D/G' peak intensity ratio changes as a function of electron fluence. Table 2 shows the results of the irradiation study. The D/G and D/G' peak intensity ratios before and after radiation are shown in Table 2. The D peak was particularly small as shown in the pre-irradiation spectrum in Figure 39. After three separate irradiation runs described in Chapter III, the greatest difference between the pre- and post-irradiation spectra came from the high fluence irradiation. The color maps shown in Figures 40 and 41 indicates the D/G peak intensity ratio followed by the D/G' peak intensity ratio and clearly indicates spectral differences in the three areas of irradiation. The un-irradiated areas retain the D/G

Table 2. D/G and D/G' peak intensity ratios for metallic fluence sample 127A showing the unirradiated and electron irradiated values. The associated fluences are indicated, with all irradiations done with 500 keV electrons. These all show an increase in the D/G and D/G' peak intensity ratios with radiation, indicating damage to the CNTs.

127 A Metallic 500 keV						
Fluence	D/G	\pm	% change	D/G'	\pm	% change
Pre 0.00	0.205	0.043	0.0%	1.071	0.102	0.0%
Post 0.00	0.165	0.034	-20.5%	1.021	0.201	-4.7%
1.41×10^{16}	0.191	0.004	-6.8%	1.269	0.062	18.5%
1.02×10^{17}	0.200	0.006	-2.4%	1.356	0.082	26.6%
5.82×10^{17}	0.231	0.011	12.7%	1.452	0.066	35.6%

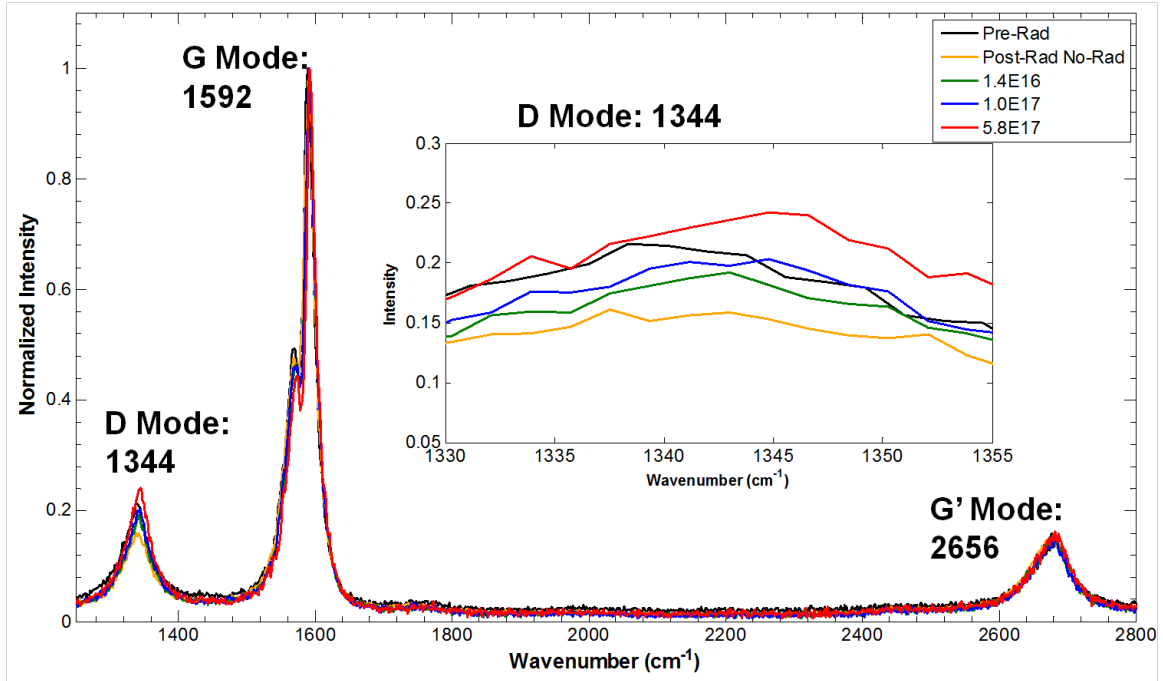


Figure 39. Normalized Raman spectra for the metallic Raman sample showing pre- and post-radiation spectra so that the increase in the D peak is obvious. The inset is the D peak. An annealing effect is seen in the post irradiation spectrum without direct radiation having an intensity lower than the pre-irradiated D peak intensity. The G' peak does not change substantially between pre- and post-radiation.

peak intensity ratio average of 0.165. The top left of the post irradiated portion of each figure shows very little change in the D/G peak intensity ratio at $1.4 \times 10^{16} \frac{e^-}{cm^2}$, where the average D/G peak intensity ratio turned out to be 0.19. The D/G' peak intensity ratio seems to display a higher shift in the low fluence area, from 1.02 to

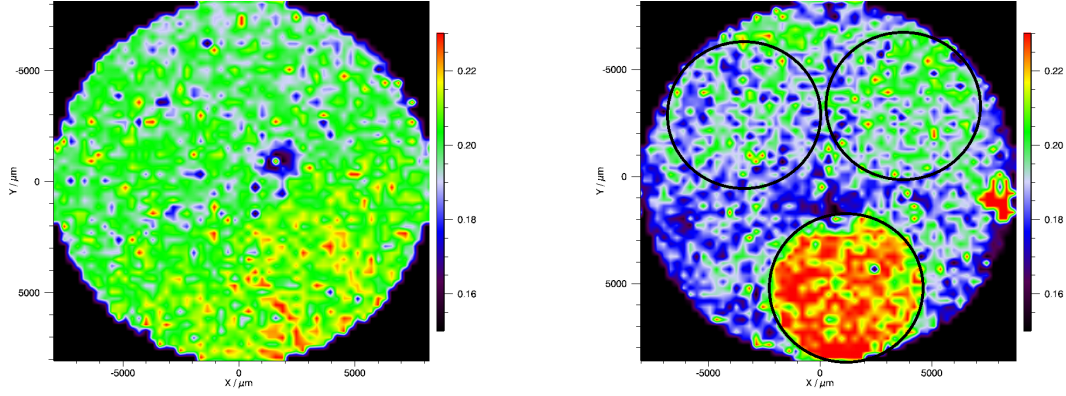


Figure 40. Pre- and post- irradiation 2-dimensional map representation of the metallic SWCNT thin film used in the Raman study showing the D/G peak intensity ratio. This corresponds to three different areas of damage, with the highest electron fluence causing the most damage in the CNTs indicated in the bottom part of the figure.

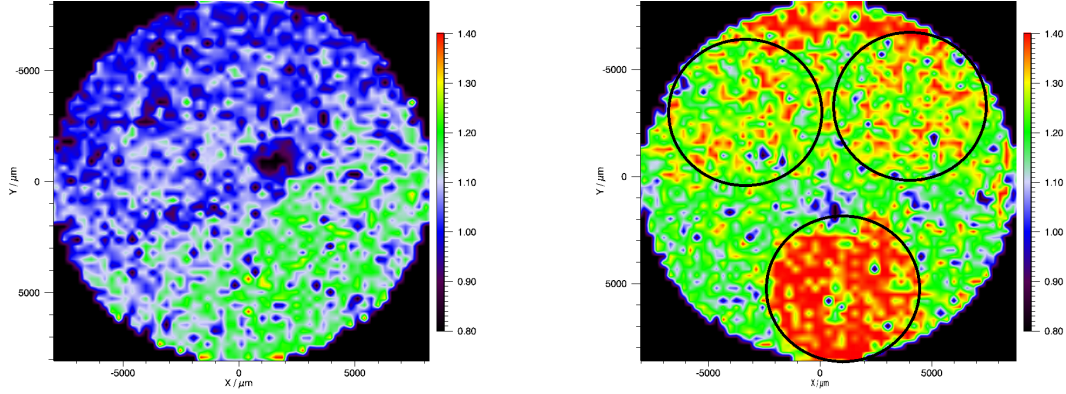


Figure 41. Pre- and post- irradiation 2-dimensional map representation of the metallic SWCNT thin film used in the Raman study showing the D/G' peak intensity ratio. This corresponds to three different areas of damage, with the highest electron fluence causing the most damage in the CNTs indicated in the bottom part of the figure.

1.26. The top right of the plot corresponds to the $1.0 \times 10^{17} \frac{e^-}{cm^2}$ fluence. This area had a bit more noticeable change in the D/G peak intensity ratio, at 0.20 while the D/G' peak intensity ratio increases to 1.35. Most notable is the bottom area of the map, which corresponds to the high fluence electron irradiation of $5.8 \times 10^{17} \frac{e^-}{cm^2}$. This area had a D/G peak intensity ratios average of 0.23 and a D/G' peak intensity ratios average of 1.45. This indicates a higher percentage of vacancies and broken bonds within the nanotubes. The most interesting result is the D/G' peak intensity ratios, which more clearly indicate the damage within the CNTs. This happens due

to the fact that the D peak intensity increases with damage, while the G' and G peak decrease in intensity.

4.1.2 Semiconducting Film

The semiconducting film was irradiated first with 500 keV electrons to the highest fluence attainable in a single day run, which amounted to 8 hours of continuous electron beam at a current of 3 μA as measured at the sample through a current integrator. This produced a calculated fluence of $6.9 \times 10^{17} \frac{e^-}{\text{cm}^2}$. This was done because the metallic sample did not show any substantial damage until the fluence was significantly above $1.0 \times 10^{17} \frac{e^-}{\text{cm}^2}$ at 500 keV. A Raman map was taken overnight,

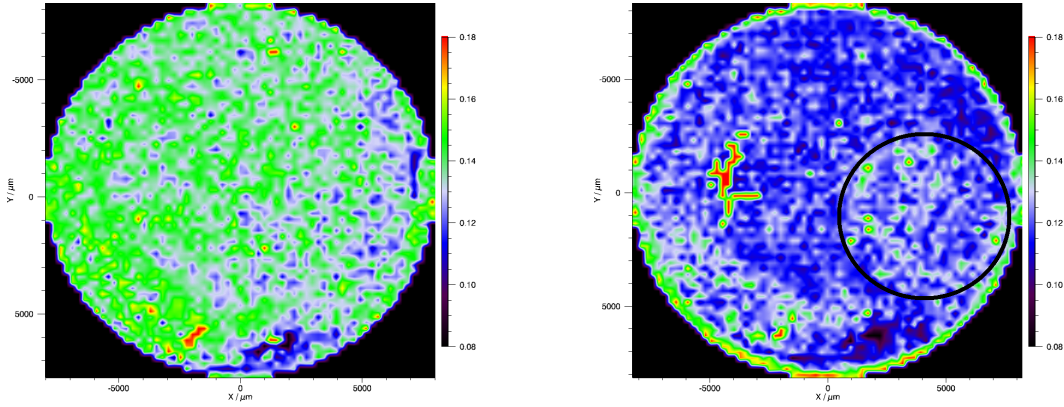


Figure 42. Pre- and post- irradiation Raman maps of the D/G peak intensity ratios after the first irradiation at 500 keV to a fluence of $6.9 \times 10^{17} \frac{e^-}{\text{cm}^2}$ over a period of 8 hours. This 2-dimensional map representation of the semiconducting SWCNT thin film used in the Raman study corresponds to the first area of irradiation on the lower right. The total D/G peak intensity ratio decreases after the first radiation.

to observe the effect of irradiation, before proceeding with the 1 MeV irradiation. In Figure 42 there is an obvious difference between the two images. Both of these images are rendered in false color indicating the local intensity of the D/G peak intensity ratio. The scale, from low to high, is 0.08 to 0.18. The left image is pre-radiation, while the right image is post radiation. The length of the radiation, in a deep vacuum (1.0×10^{-6} torr) and the heat generated from the energetic electrons

streaming through the sample and impacting the steel cold head are believed to be the cause of the decrease in the D/G peak intensity ratio outside the irradiated area. This uniform decrease in the D/G peak intensity ratio from the first irradiation was not anticipated and is counter-intuitive. Most likely, there was significant desorption of ambient air molecules, as well as significant heating effects during the irradiation. The cold head is plumbed with chilled water, but does not remain significantly cold during the irradiation. Local heating within the SiO₂ and Si substrate could have had an annealing effect on the CNTs causing the structure to actually improve by annealing out additional intrinsic defects. This is also evident in the D/G' peak intensity ratio spectrum shown in Figure 43. The scale on the D/G' peak intensity

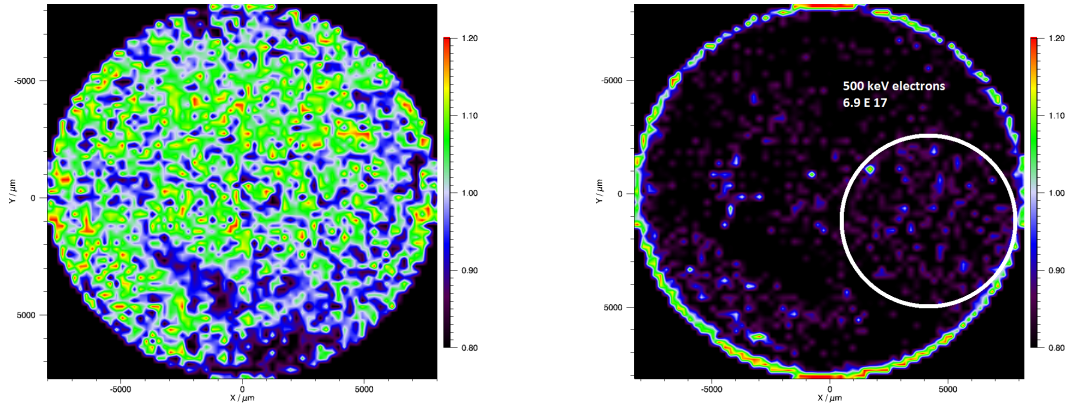


Figure 43. Pre- and post- irradiation 2-dimensional map representation of the semi-conducting SWCNT thin film used in the Raman study after the first 500 keV electron irradiation to a fluence of $6.9 \times 10^{17} \frac{e^-}{cm^2}$ over a period of 8 hours. This shows an annealing effect of the heat and low pressure in the D/G' peak intensity ratio.

ratio is 0.80 to 1.2, which clearly shows the annealing effect discussed above. The change in the D/G' peak intensity ratio appears to be a bit stronger from viewing the difference in false color maps.

The second irradiation was done at 1 MeV to compare the difference between the 500 keV and 1 MeV electron energies. These irradiation values and their associated D/G and D/G' peak intensity ratios are shown in Table 3.

Table 3. Table of the D/G and D/G' ratios for semiconducting fluence sample 127B showing the unirradiated and electron irradiated values. The post radiation values are separated into the 500 keV irradiation and the 1 MeV irradiation with associated fluences indicated. These show an increase in the D/G ratio and D/G' with radiation, indicating damage to the individual CNTs. The D/G and D/G' ratios increased substantially with the 1 MeV irradiation as expected indicating significant damage to the CNTs within the thin film network.

127 B		Semi					
500 keV	D/G	\pm	% change	D/G'	\pm	% change	
Pre 0.00	0.130	0.006	0%	0.726	0.029	0%	
Post 0.00	0.103	0.005	-20.8%	0.661	0.022	-9.0%	
6.89×10^{17}	0.125	0.008	-3.8%	0.876	0.159	20.7%	
1 MeV							
2.18×10^{17}	0.149	0.018	14.6%	1.047	0.119	44.2%	

The plan was to irradiate to the same total fluence as the 500 keV irradiation, but this was significantly cut short due to the leakage current on the Dynamitron exceeding safe parameters necessitating a total shut down of the accelerator. The resultant fluence at 1 MeV was $2.2 \times 10^{17} \frac{e^-}{cm^2}$ with the damage shown in Figure 44. The result of this 1 MeV irradiation produced significantly more damage. This result is shown graphically as D/G peak intensity ratio in Figure 45 with the lower right corresponding to the 500 keV irradiation, while the left side shows the 1 MeV irradiation. This is followed by Figure 46 which shows the D/G' peak intensity ratio.

The significant damage indicated by the 1 MeV irradiation prompted the comments in Chapter V for follow on work by completing Hall measurements at 1 MeV electron energy. The images in Figures 45 and 46 show the difference between the first irradiation Raman maps and the second irradiation at 1 MeV. There does not appear to be significant further annealing of the bulk film, but there is a color change from the first to the second in Figure 45 when looking exclusively at the lower right area which corresponds to the 500 keV irradiation suggests that there was a small amount of annealing in this damaged area. The scale in Figure 46 at 0.60 to 0.90 is

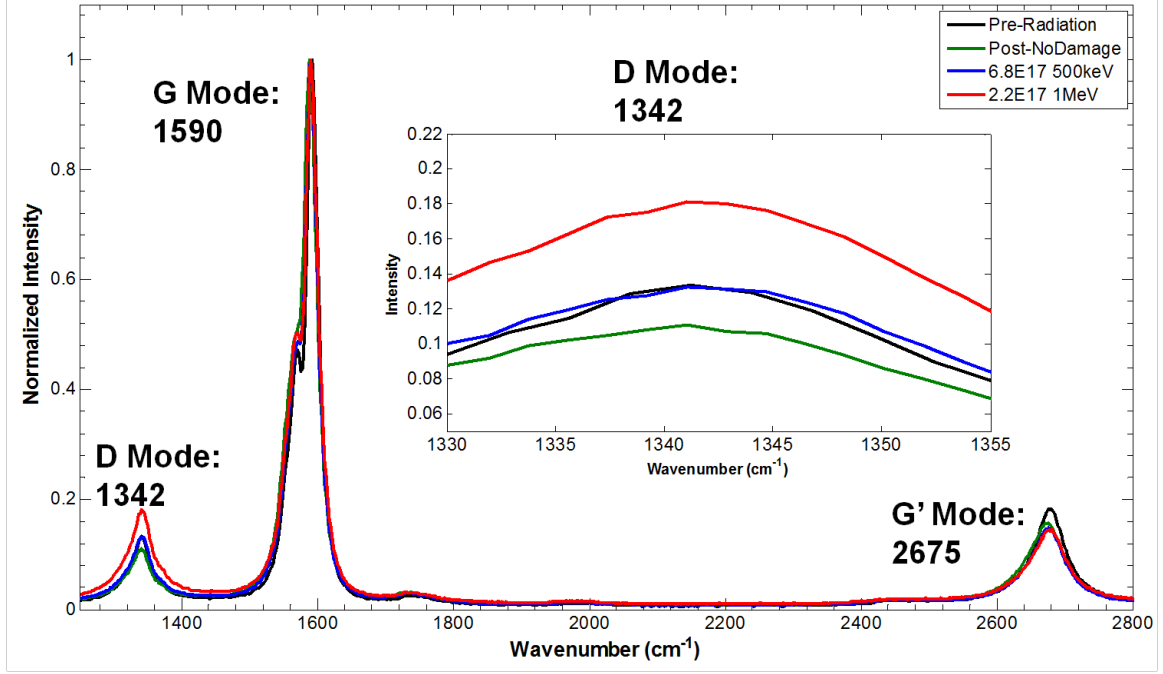


Figure 44. Normalized Raman spectra for the semiconducting Raman sample showing pre- and post-radiation spectra so that the increase in the D peak is obvious. The inset here is the D peak. An annealing effect is seen in the post irradiation spectrum without direct radiation having an intensity lower than the pre-irradiated D peak intensity. The G' peak does not change substantially between pre- and post-radiation.

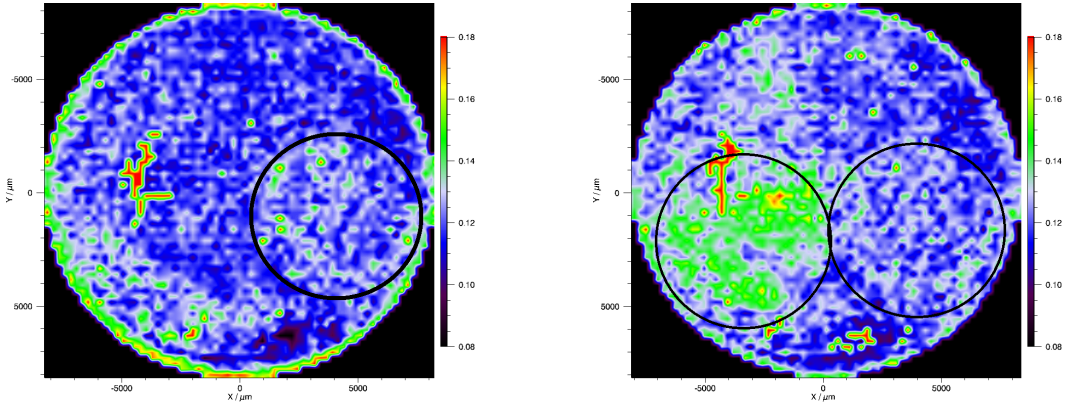


Figure 45. Raman maps of the D/G peak intensity ratios after the first irradiation at 500 keV to a fluence of $6.9 \times 10^{17} \frac{e^-}{cm^2}$ over a period of 8 hours on the left. The right image is after the 1 MeV irradiation to a total electron fluence of $2.2 \times 10^{17} \frac{e^-}{cm^2}$ over a period of 6 hours. The scale is the same as Figure 42 from 0.08 to 0.18 in D/G peak intensity ratio.

slightly lower than the previous images in order to focus on the changes in the 1 MeV irradiation.

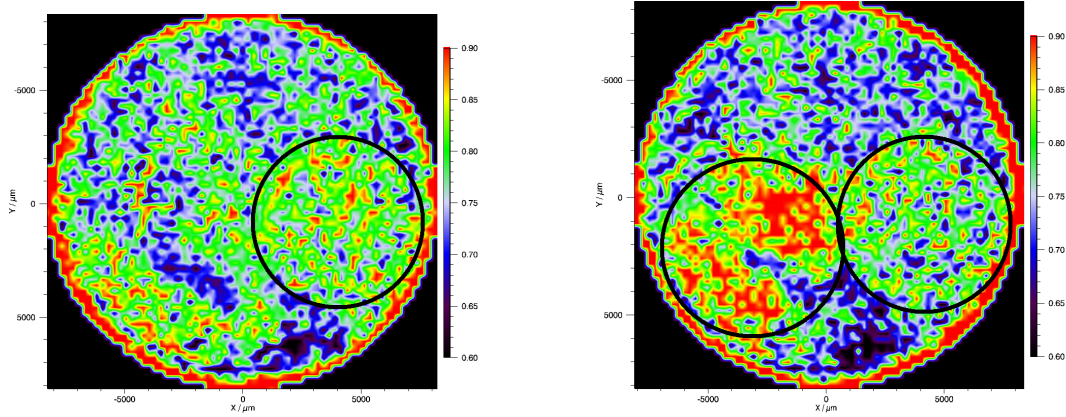


Figure 46. Raman spectra maps of the D/G' peak intensity ratios after the first irradiation at 500 keV to a fluence of $6.9 \times 10^{17} \frac{e^-}{cm^2}$ over a period of 8 hours on the left. The right image is after the 1 MeV irradiation to a total electron fluence of $2.2 \times 10^{17} \frac{e^-}{cm^2}$ over a period of 6 hours. The scale is lower than Figure 43 from 0.60 to 0.90 in D/G' peak intensity ratio. This highlights the two separate irradiation areas more clearly.

The 1 MeV result shown here demonstrates the concept put forth in Chapter II of NIEL. The higher energy electrons create more damage in the CNT networks through much more energetic interactions and higher probability of dislocating a carbon atom through a direct impact causing knock on damage. This knock on damage, at higher electron energy, causes significantly more cascade effects, akin to low energy carbon ion irradiations.

4.2 Hall Study

The second phase of the experiment was irradiation of the Hall samples with 500 keV electrons. The Hall study resulted in significant changes in conductivity as a function of electron fluence. The semiconducting thin film was irradiated first, followed by the metallic thin film.

Both the metallic and semiconducting thin films were measured to be p-type, meaning that holes are the primary charge carriers, and not electrons. This is most likely due to adsorbates clinging to the CNT walls creating conduction pathways through the CNT network of the thin films. Under vacuum, particularly after an-

nealing in a forming gas such as argon, these adsorbates tend to disassociate which can turn the p-type CNT films into n-type. A summary of the Hall measurements for both films is shown in Table 4.

Table 4. This table summarizes the room temperature Hall measurements on both the semiconducting and metallic SWCNT thin films for the pre- and post-irradiation measurements with the corresponding changes noted.

	Metallic	Pre-Radiation	Post Rad 2.6×10^{16}	% Change
Raman D/G		0.14 ± 0.009	0.137 ± 0.009	2%
Conductivity (S/cm)		160	127	21%
	Semiconducting	Pre-Radiation	Post Rad 2.5×10^{17}	% Change
Raman D/G		0.077 ± 0.004	0.087 ± 0.013	13%
Conductivity (S/cm)		170	30	82%

4.2.1 Metallic Film

The fluence attained on the metallic thin film was an order of magnitude lower than the semiconducting sample. The sample was irradiated to $2.5 \times 10^{16} \frac{e^-}{cm^2}$. Figure 47 shows the change in conductivity after the irradiations. There was not a significant change in the slope of the plot of conductivity to temperature, but the magnitude changed by 27%. This result is consistent with results from a similar experiment with alpha particles.[2]

From the Hall measurements, the mobility and carrier concentrations are plotted in Figures 48 and 49. The mobility is slightly higher in the pre-radiation measurements. The carrier concentration is very noisy which makes a clear separation of the pre- and post-radiation values difficult.

The pre-radiation Raman intensity map of the D/G' peak intensity ratio, Figure 50, with the post-radiation peak intensity map right next to it, on the right, shows the differences caused by the radiation of $2.5 \times 10^{16} \frac{e^-}{cm^2}$. In this case, the figures are nearly indistinguishable from each other. There is almost no noticeable change in the

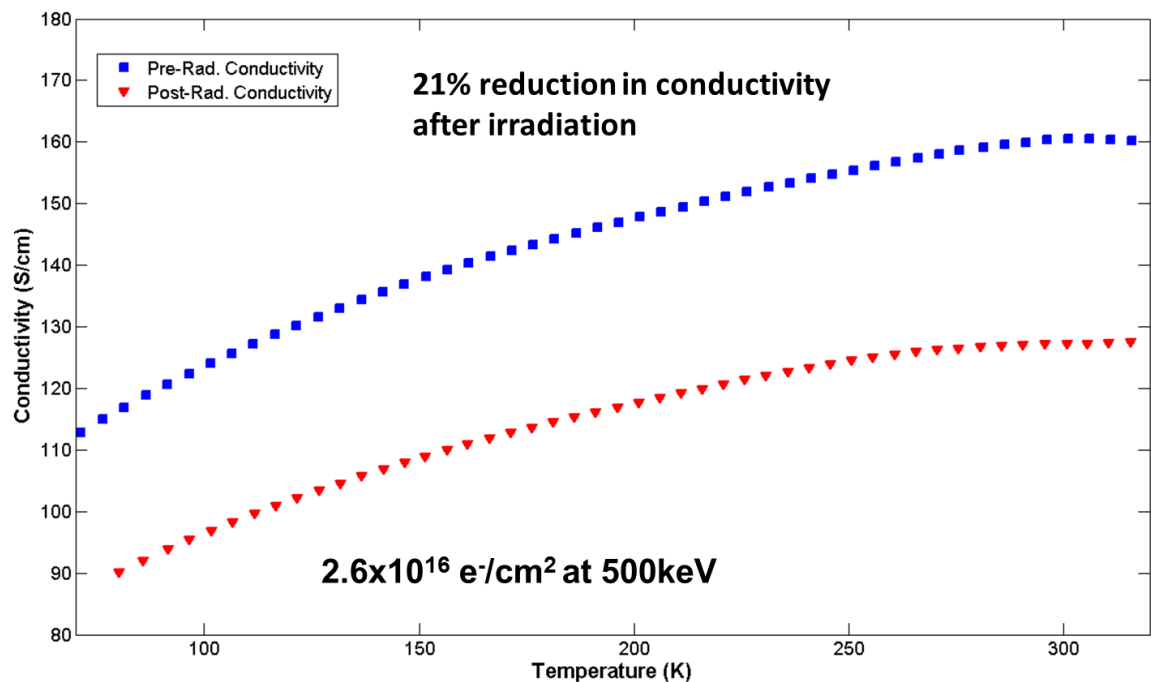


Figure 47. Plot of metallic SWCNT thin film (134D) irradiated with $2.5 \times 10^{16} \frac{e^-}{cm^2}$ showing a change in the conductivity post-irradiation.

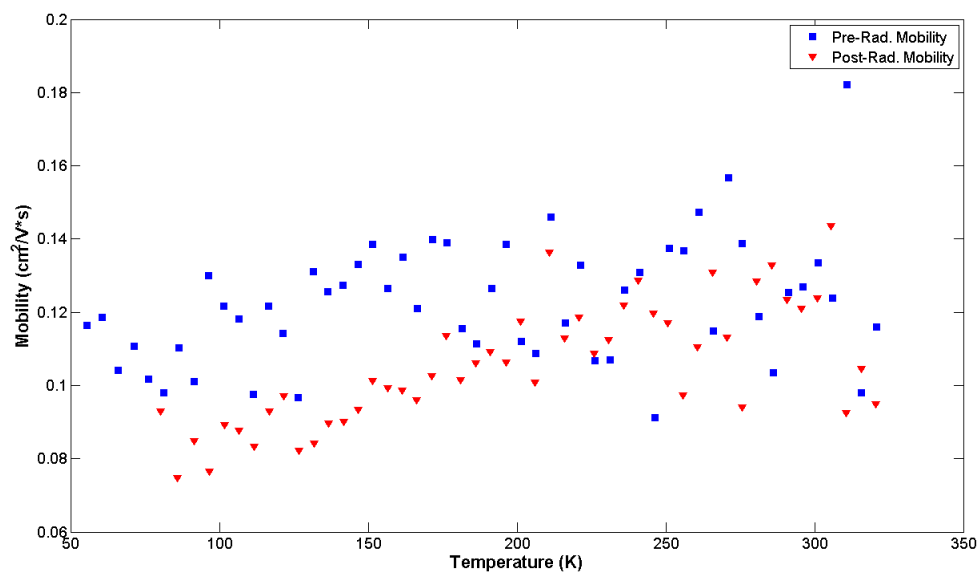


Figure 48. Plot of the metallic Hall sample (134D) pre-irradiation (blue) and post-irradiation (red) mobility as a function of temperature.

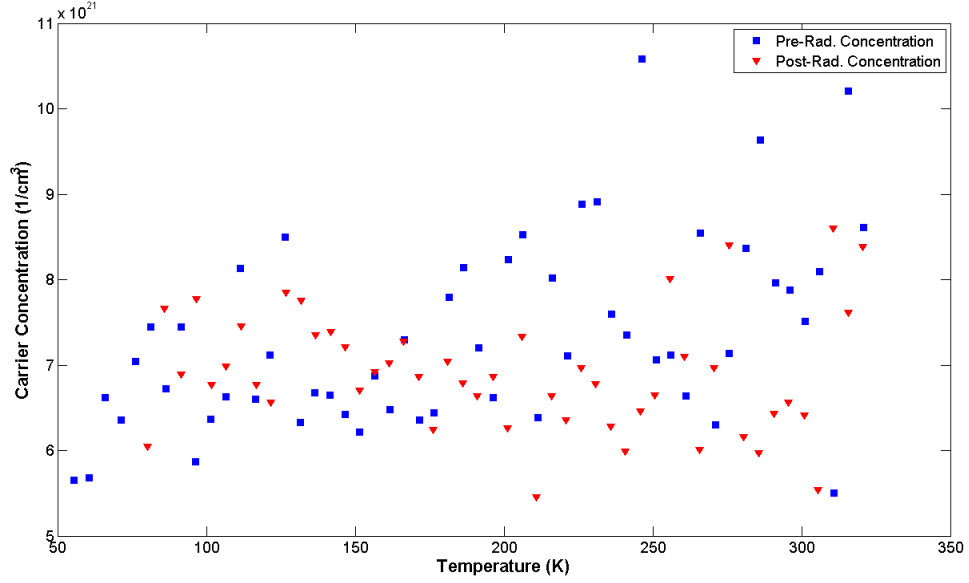


Figure 49. Plot of the metallic Hall sample (134D) pre-irradiation (blue) and post-irradiation (red) carrier concentration as a function of temperature.

D/G' peak intensity ratio with this low of an electron fluence which is consistent with the displacement damage dose calculations.

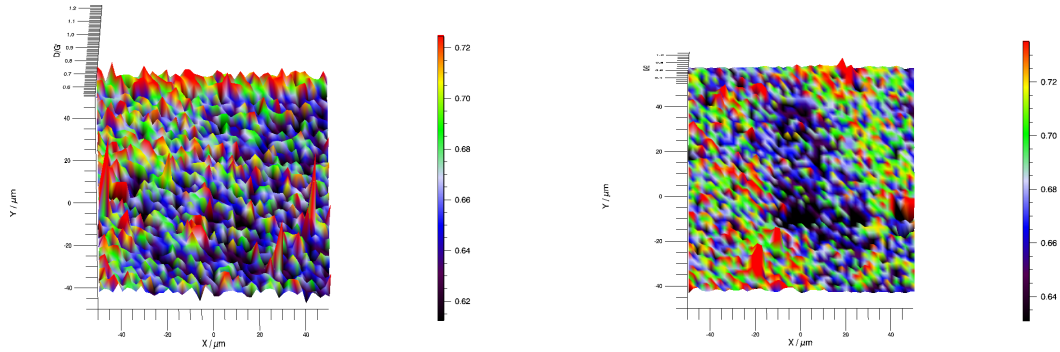


Figure 50. Metallic thin film sample 134D pre- and post-radiation Raman intensity map of the D peak intensity divided by the G' peak intensity created using the Renishaw WIRE program. The scale on the right hand side gives the color value of the D/G' peak intensity.

The summary of the change to the D/G and D/G' peak intensity ratios are shown in Table 5.

Table 5. Table of the D/G and D/G' ratios for metallic sample 134D showing the unirradiated and electron irradiated values. The post radiation values show a slight decrease in the D/G ratio, while the D/G' ratio increased indicating some damage within the individual CNTs within the thin film network.

134D Metallic 500 keV						
Fluence	D/G	\pm	% change	D/G'	\pm	% change
Pre 0.00	0.146	0.020	0%	0.664	0.044	0%
2.63×10^{16}	0.142	0.026	-2.7%	0.684	0.054	3.0%

4.2.2 Semiconducting Film

The first sample to be tested with Hall measurements was the semiconducting sample with palladium contacts. After an irradiation fluence of $2.5 \times 10^{17} \frac{e^-}{cm^2}$, this thin film showed almost an order of magnitude change in conductivity at room temperature, and an 82% change in the conductivity on the temperature dependent Hall measurements down to liquid nitrogen temperatures. There is also a significant visual change to the sample as shown in Figure 51.

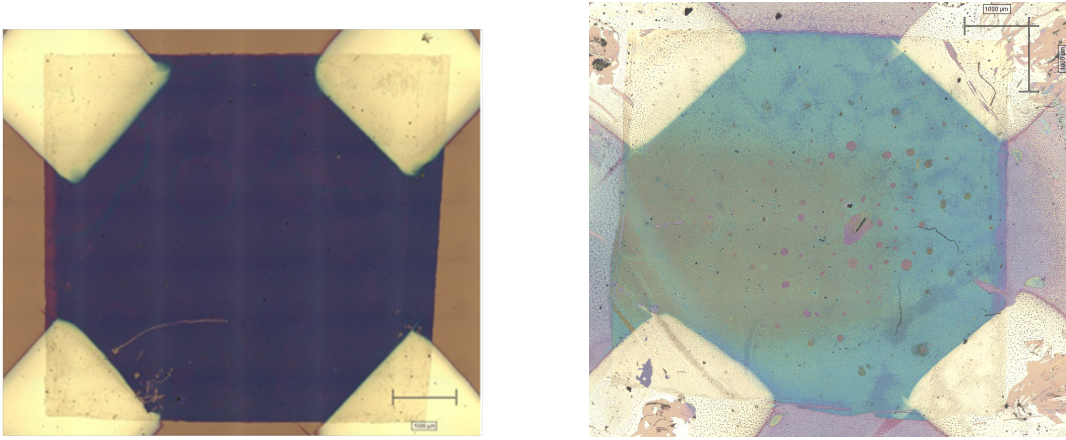


Figure 51. Pre- and post-irradiation optical photographs of the semiconducting CNT sample 134H. This demonstrates the obvious difference in the thin films after irradiation with electrons. In this case, the sample was irradiated with 500 keV electrons to a total fluence of $2.5 \times 10^{17} \frac{e^-}{cm^2}$

The Hall plots shown in Figure 52 show four distinct regions of conductivity related to temperature. The slope of the graph changes substantially from the pre-

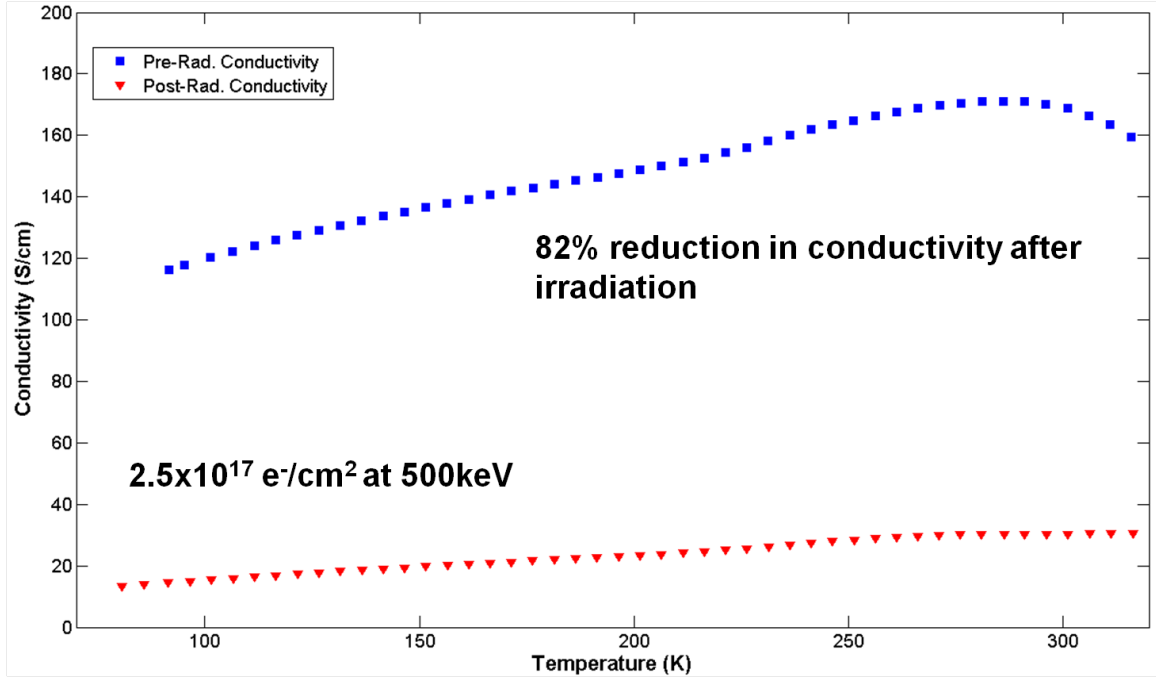


Figure 52. Plot of semiconducting SWCNT thin film (134H) irradiated with $2.5 \times 10^{17} \frac{e^-}{cm^2}$ showing a change in the conductivity post-irradiation of 82%

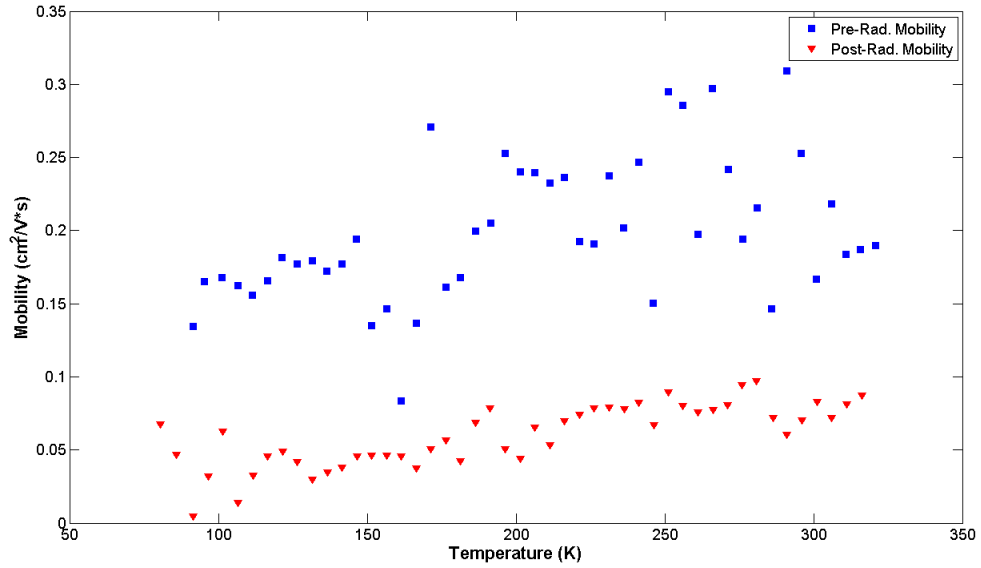


Figure 53. Plot of the semiconducting Hall sample (134H) pre-irradiation (blue) and post-irradiation (red) mobility as a function of temperature.

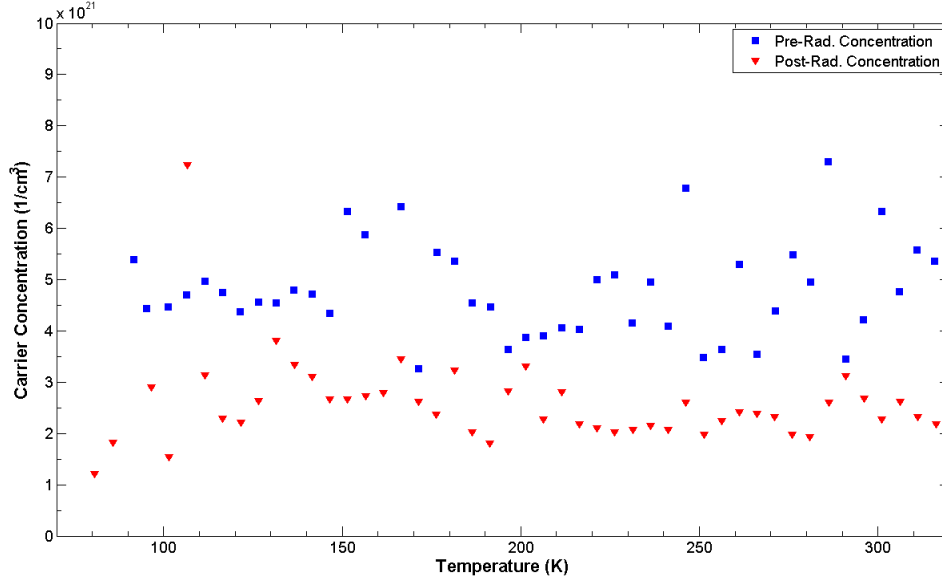


Figure 54. Plot of the semiconducting Hall sample (134H) pre-irradiation (blue) and post-irradiation (red) carrier concentration as a function of temperature.

irradiation to the post-irradiation measurements, indicating changes in the tube to tube conduction as well as an increase in scattering centers. There is an obvious difference in the mobility before and after irradiation shown in Figure 53. There is also a slight but noticeable decrease in the carrier concentration in Figure 54.

The Raman results are shown in Table 6. This indicates the change in D/G peak intensity ratio as well as the D/G' peak intensity ratio. This result is rather in-

Table 6. Table of the D/G and D/G' ratios for semiconducting sample 134H showing the unirradiated and electron irradiated values. The post radiation values show an increase in the D/G ratio, while the D/G' ratio remained the same within experimental error.

134H Semi 500 keV						
Fluence	D/G	±	% change	D/G'	±	% change
Pre 0.00	0.073	0.030	0%	0.467	0.032	0%
2.50×10^{17}	0.091	0.005	24.7%	0.459	0.031	-1.7%

teresting because the change in the CNT damage from comparison of the pre- and post-irradiation Raman spectra show only a 15% change in the D/G peak intensity

ratio. This implies that there is something else contributing to the decrease in conductivity besides the increase in scattering centers from defect formation within the CNTs. One plausible hypothesis is that there is significant positive charge buildup in the oxide layer causing localized electric fields that influence the charge carriers within the CNTs. Another hypothesis is that there is not a linear relationship between the change in conductivity and the change in the D/G and D/G' peak intensity ratios.

4.3 Vacuum Study

The vacuum study produced different results from those obtained with the Ecopia pin board measurements due to the significantly increased resistance of the experimental setup. This is compensated for through a constant multiplication in the results to normalize the results to those of the pin board, which are believed to be much more accurate.

The I-V curves show the same relationships in both samples. Resistance increases as the temperature is lowered from (300 K), to the liquid nitrogen temperature (77 K). This indicates that thermally assisted tunneling dominates the conduction, in that the samples become more resistive at lower temperatures without the thermal energy necessary to overcome the conduction barrier. This is most likely dominated by the tube to tube conduction, which should be temperature dependent.

The theory of adsorption increasing conduction in CNT networks is illustrated by the fact that as the vacuum increases, the resistance of the CNTs also increases. This suggests that the adsorbed molecules are desorbing, which is decreasing the density of conduction pathways through the CNT network, which increases the resistance.

According to the same theory discussed in Chapter II, work by Collins *et al.* indicates that once the CNTs are re-exposed to ambient air, that adsorption will happen almost instantly, reversing the resistivity change caused by the vacuum desorption.[29]

Interestingly, the semiconducting sample shows a significant time as well as pressure

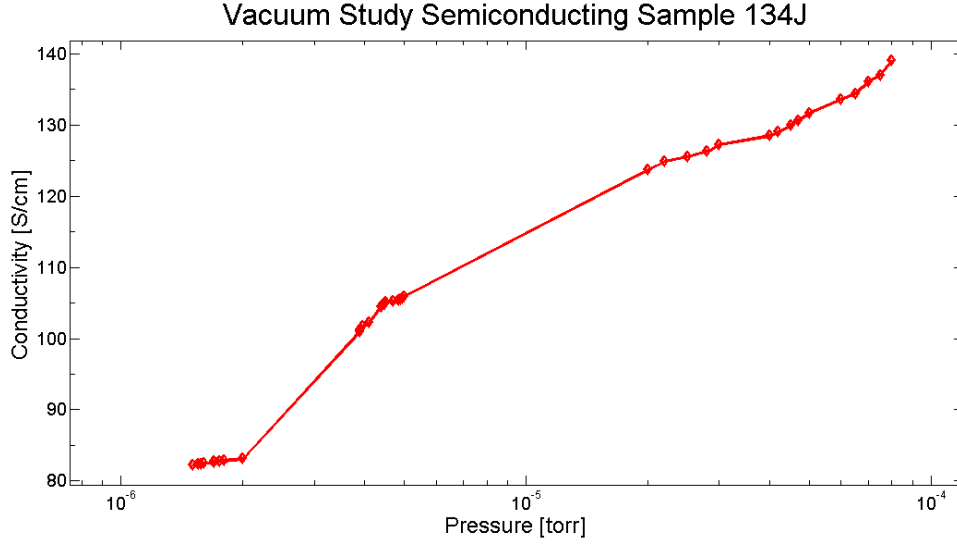


Figure 55. Plotted results of the vacuum study with the un-irradiated semiconducting sample 134J. This figure is plotted with conductivity on the vertical axis, as a function of pressure in torr on a log scale.

dependence with the decrease in conductivity which can be seen in Figure 55. In each set of 5 measurements, the conductivity goes down steadily. This suggests that the air molecules are desorbing from the CNTs.

4.4 Radial Breathing Mode Changes

Further analysis of the Hall sample spectra revealed an interesting phenomenon that is suggested in Chapter II. The Hall spectra of both the metallic and semiconducting Hall samples, 134D and 134H captured the entire spectral range from 0 to 2800 cm^{-1} which allows some further analysis. Particularly, the Radial Breathing Mode (RBM) phonon peak is captured. The pre- and post-irradiation Raman spectra in the RBM region for both the metallic and semiconducting Hall samples are shown in Figures 56 and 57. Although these peaks are not high intensity, they can be analyzed for information.

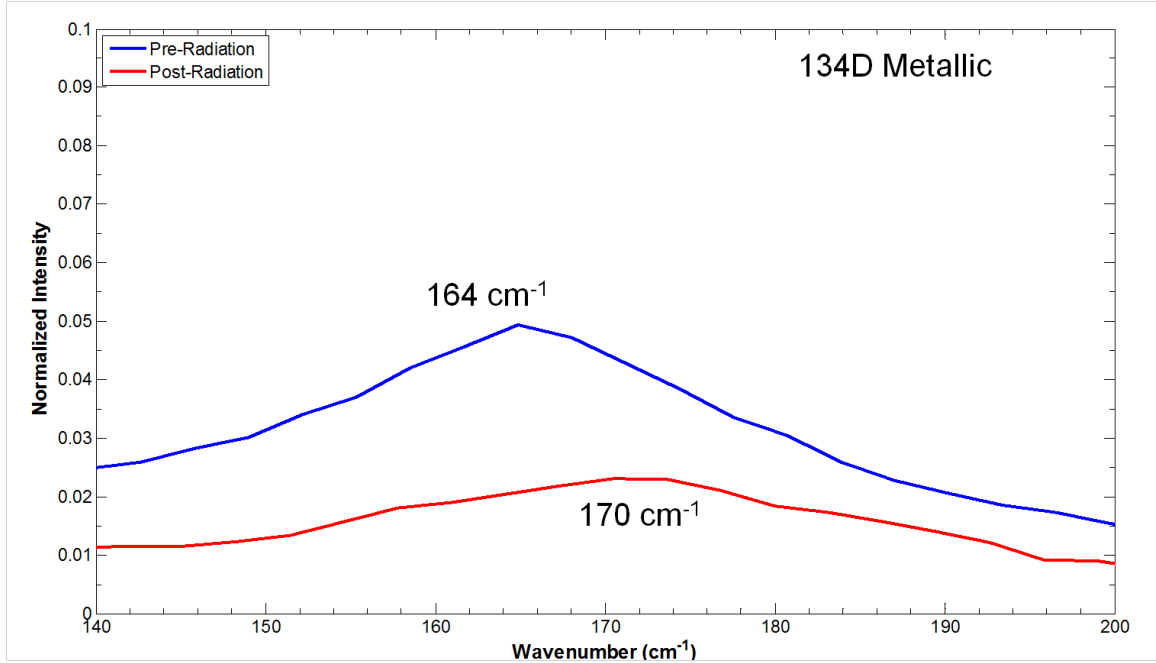


Figure 56. Plot of the radial breathing mode for sample 134D metallic CNTs. This shift is highlighted to show a potential annealing or diameter dependent degradation as a function of electron radiation damage.

Theory suggests that knock on damage can be annealed with high temperatures (above 300 °C) which can cause local shrinking of the CNT diameters. Sample 134D had a RBM peak at 164 cm^{-1} which suggests an average CNT diameter of 1.50 nm, while after the irradiation, it peaked up at 170 cm^{-1} . This corresponds to an average tube diameter of 1.45 nm. This trend is repeated in the semiconducting sample 134H where the pre-radiation RBM peak was 153 cm^{-1} with an average tube diameter of 1.62 nm. The post-radiation RBM peak shows up at 158 cm^{-1} indicating an average tube diameter of 1.57 nm. This does not appear to be overly dramatic, but does suggest that there is damage in the CNTs, and that the heat of the irradiation itself could be causing some annealing effects rendering the average tube diameters smaller. Another potential explanation for this phenomenon follows from Rossi *et al.* where they show that the larger diameter tubes are being damaged to the point of ablating off leaving the smaller tubes.[3] Without doing a high intensity RBM specific Raman

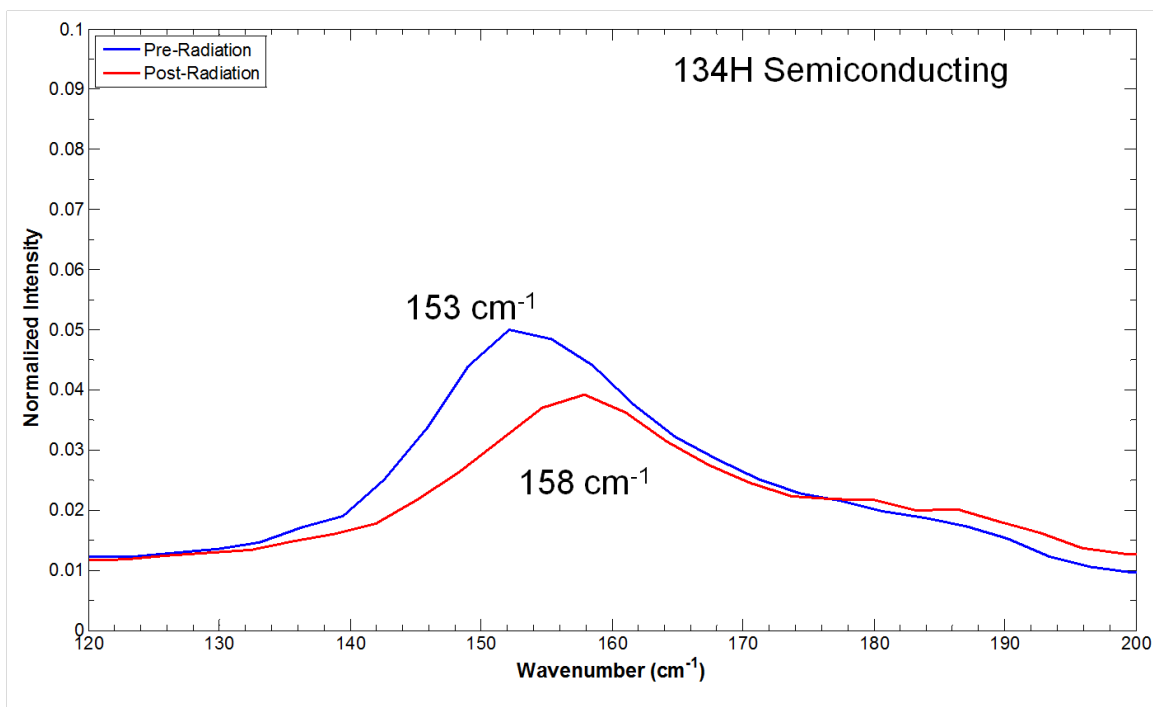


Figure 57. Plot of the radial breathing mode for sample 134H semiconducting CNTs. This shift is highlighted to show a potential annealing or diameter dependent degradation as a function of electron radiation damage.

study with the same type of radiation damage, it is difficult to clearly explain this shift.

V. Conclusions

5.1 Raman Study

The Raman study using 500 keV electrons with pre-and post irradiation Raman spectroscopy showed that above $1.0 \times 10^{17} \frac{e^-}{cm^2}$ there was measurable damage within the carbon nanotubes alone. The variation within the D/G peak intensity ratio maps as well as the D/G' peak intensity ratio maps is quite evident with the higher fluence. This confirmed the calculations of the non-ionizing energy loss in electrons causing damage to the nanotubes above a threshold fluence of energetic electrons. The 1 MeV irradiation on the semiconducting thin film was more damaging, which again corresponded to the higher NIEL calculation shown using the Akkerman-Barak theory as presented in the theory section along with the DDD presented by Rossi *et al.* Using a simple calculation of DDD presented by Rossi *et al.*[3]

$$DDD = NIEL \times e^- \text{ Fluence} \quad (16)$$

where the NIEL is calculated for 500 keV electrons using the Akkerman-Barak method.[33] This value is $4.0 \times 10^{-5} \text{ MeV-cm}^2/\text{g}$. The damage changes can be shown to begin at DDD values of $4.0 \times 10^{12} \text{ MeV/g}$ which corresponds to an electron fluence of $1.0 \times 10^{17} \frac{e^-}{cm^2}$. The 1 MeV NIEL calculation produces $5.1 \times 10^{-5} \text{ MeV-cm}^2/\text{g}$ and a DDD value of $1.1 \times 10^{13} \text{ MeV/g}$ at a fluence of $2.2 \times 10^{17} \frac{e^-}{cm^2}$. The results are summarized in Table 7.

The overall results of the D/G peak intensity ratios as well as the D/G' peak intensity ratios are normalized to their pre-radiation levels, and plotted as a function of DDD in Figure 58. Although the data is somewhat noisy, the general trend holds true that the increasing radiation damage dose increases the damage within the thin

Table 7. This table summarizes the Raman changes within all of the samples tested, specifically the ratio of the D/G and D/G' intensities.

500 keV	Fluence	D/G	\pm	Δ	D/G'	\pm	Δ	DDD
127 A	Pre 0.00	0.205	0.043	0%	1.071	0.102	0%	0.00
127 A	Post 0.00	0.165	0.034	-19.5%	1.021	0.201	-4.7%	0.00
127 A	1.41×10^{16}	0.191	0.004	-6.8%	1.269	0.062	18.5%	5.61×10^{11}
127 A	1.02×10^{17}	0.200	0.006	-2.4%	1.356	0.082	26.6%	4.06×10^{12}
127 A	5.82×10^{17}	0.231	0.011	12.7%	1.452	0.066	35.6%	2.31×10^{13}
134 D	Pre 0.00	0.146	0.020	0%	0.664	0.044	0%	0.00
134 D	2.63×10^{16}	0.142	0.026	-2.7%	0.684	0.054	3.0%	1.05×10^{12}
134 H	Pre 0.00	0.073	0.030	0%	0.467	0.032	0%	0.00
134 H	2.50×10^{17}	0.091	0.005	24.7%	0.459	0.031	-1.7%	9.93×10^{12}
127 B	Pre 0.00	0.130	0.006	0%	0.726	0.029	0%	0.00
127 B	Post 0.00	0.103	0.005	-20.8%	0.661	0.022	-9.0%	0.00
127 B	6.89×10^{17}	0.125	0.008	-3.8%	0.876	0.159	20.7%	2.74×10^{13}
1 MeV	2.18×10^{17}	0.149	0.018	14.6%	1.047	0.119	44.2%	1.12×10^{13}

film network. The fact that significant changes in the Raman spectra indicating damage was only obvious above a fluence of $1.0 \times 10^{17} \frac{e^-}{cm^2}$ confirms the radiation hardness of these particular samples in an electron environment that exceeds the expected total fluence in 30 years on a low earth orbit satellite by several orders of magnitude. Separating the substrate effects from the purely CNT effects indicates that given a substrate structure that resists charging effects from electron radiation will allow these CNT networks to be employed in a high flux electron environment as electronic devices with a low probability of CNT structural damage causing device failure.

5.2 Hall Study

The Hall study showed conductivity changes in the thin films at much lower fluences than those observed in the fluence study. This is believed to be a combination

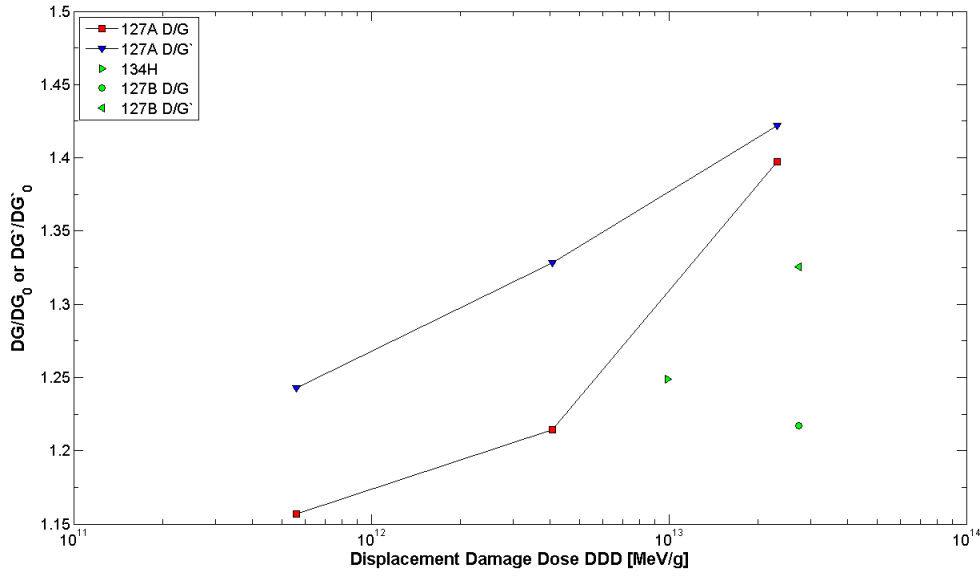


Figure 58. Displacement damage dose chart showing Raman measurements normalized to their pre-radiation values and plotted versus the calculated DDD. The general trend is an increase in damage as a function of radiation dose.

of positive charge buildup in the SiO₂ layer causing localized electric fields which influence the charge carriers in the CNTs, as well as a change in the thermally activated variable tube hopping parameter. As shown in Chapter II the positive charge buildup in silicon dioxide is significant enough to cause local electric fields. These local fields are most likely in the form of trapped positive charge (holes) at the interface of the SiO₂ and CNT network. The p-type nature of these CNT thin films is primarily due to oxygen and nitrogen adsorbents creating a doping effect. This likely causes the negative charge carriers in the CNT thin film to be pulled toward the substrate interface, while the positive charge carriers are repulsed and dominate the upper area of the CNT network. This charge separation likely causes the decrease in conductivity seen in the Hall study, since there is not enough evidence from the Raman results to point to significant charge scattering and bond breaking.

This change in conductivity was much more evident at fluences capable of producing measurable CNT defects. The fluence was higher, causing more measurable

damage to the individual CNTs, as well as a greater probability of charge trapping in the SiO₂ layer causing even stronger localized electric fields. These effects combine to break some of the percolation pathways within the CNT thin films. There is much more disorder introduced into the thin films at higher electron fluences which tends to decrease the conductivity of the thin film structure.

5.3 Future Work

The future work in this research area could be multi-faceted. Initially, this work should be repeated with an electron energy of 1 MeV, using in-situ temperature dependent Hall measurements, with pre- and post- Raman spectroscopy. This would significantly expand the scope of this research. With the Raman spectroscopy, a 633 nm laser should be used for all Raman measurements, while capturing the entire spectrum, from the RBM peak at 100 cm^{-1} to the full G' peak above 2700 cm^{-1} . This would allow comparison of the RBM shift, along with the D/G and D/G' peak ratios. The 633 nm laser should be closer to the peak absorption of the CNTs, which will likely give more reliable results. A substrate charging study would also be interesting to help separate substrate induced changes in the conductivity from the true CNT thin film conductivity changes. A more thorough temperature and pressure study would also help to explain the full effects of adsorption on the CNT thin films, as well the time dependence of the desorption of ambient molecules.

One particular area of interest is doing the same type of research on aligned CNT structures. Using the same deposition methods as are outlined in this thesis, one could fabricate CNT thin films that are aligned with a magnetic field to produce mono-directional devices to improve the charge transport in a single direction. Performing Hall measurements on these aligned thin films would potentially yield very useful

and promising results. Additionally, neutron and electron damage studies on these aligned thin films could yield useful results.

The construction of top gated field effect transistors out of these SWCNTs would also be useful. The optimum design for these transistors would be magnetically aligned SWCNT thin films on a flexible polyamide thin film substrate patterned using standard lithographic processing available at the AFIT clean room. The FETs could use hafnium oxide (HfO_2) that is a few angstroms thick using atomic layer deposition (ALD) available at AFRL sensors directorate. It would be very useful to explore passivation and isolation mechanisms to keep adsorbents from the CNT thin films during fabrication and subsequent testing. These FET structures could be tested as transistors, detectors, and integrated circuits, along with radiation testing. This structure could then potentially be tested for use as an alpha particle detector, neutron detector, or other charged particle detector.

5.4 Overall Conclusions

This study compares well to other published work referenced here. This research adds to the growing body of research on radiation effects in CNT thin films. There is a consistent decrease in the conductivity of CNT thin films under high radiation fluence. The fluence for all charged particle damage, including this work with electrons, is on the same order as the fluence required to significantly damage traditional semiconductor material such as silicon referenced in Chapter II.

The previous work with neutrons, boron and phosphorous ions, alpha particles, carbon ions, as well as the electrons shown here all demonstrate the same general trends of decreasing conductivity of CNT networks at high radiation fluences well in excess of total fluences known to exist in a lifetime of satellites in Earth orbit. When taken together with well known charging effects in oxides and electrical characteriza-

tion of CNT networks, evidence is compelling for using CNT networks as transistors, detectors, and other electrical devices in high radiation environments. A satellite in a low earth orbit will only accumulate 7.3×10^{12} electrons per cm^2 at or above 500 keV over its lifetime. This is an ideal number, because the radiation environment is actually a full spectrum of electron energies, as well as other charged particles. However, 4 orders of magnitude is significant enough to say that there is a large margin of safety for employing devices made from CNT networks. This depends, as has been shown, on the substrate that the CNTs are supported on. With a substrate that is not prone to charging effects which could degrade the devices prematurely, functional electronics could be made for space environments as well as high radiation terrestrial environments.

Appendix A. Raman

1.1 D, G, and G' Maps

Here are additional images that are useful for reference and to understand the Raman spectra.

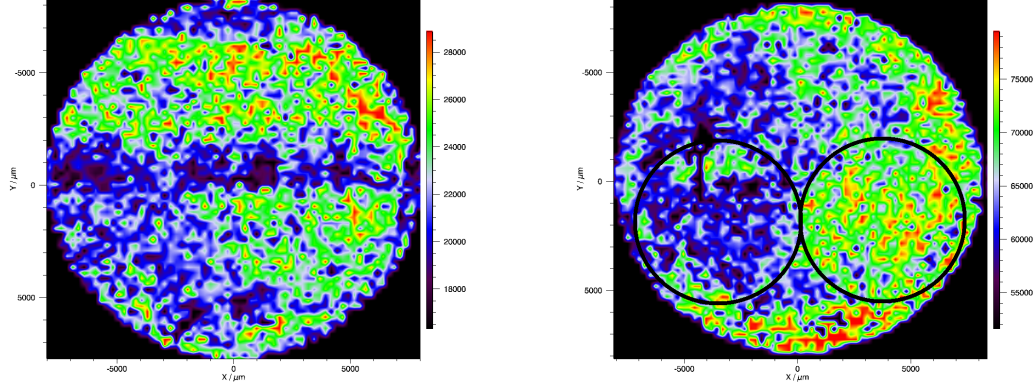


Figure 59. Raman maps of the semiconducting Raman sample 127B showing G peak intensity at 1592 cm^{-1} before and after the two separate irradiations. The left figure is pre-irradiation, the right figure is post irradiation. The irradiations were 500 keV on the lower right, and 1 MeV on the lower left of the right figure.

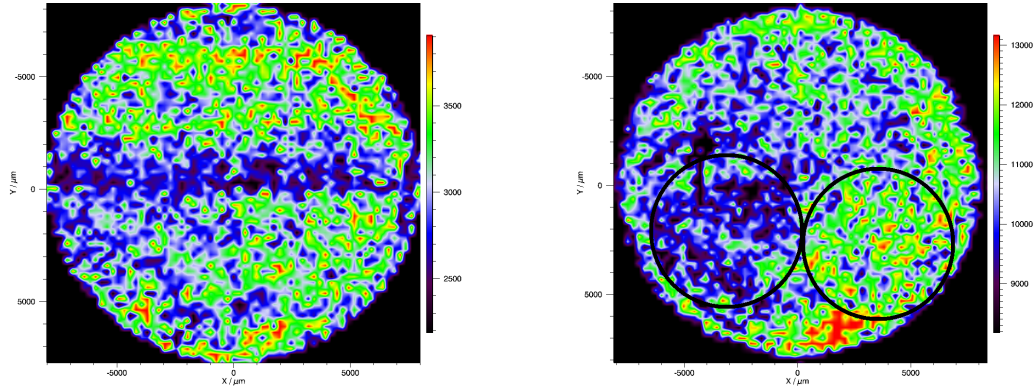


Figure 60. Raman maps of the semiconducting Raman sample 127B showing G' peak intensity at 2677 cm^{-1} before and after the two separate irradiations. The left figure is pre-irradiation, the right figure is post irradiation. The irradiations were 500 keV on the lower right, and 1 MeV on the lower left of the right figure.

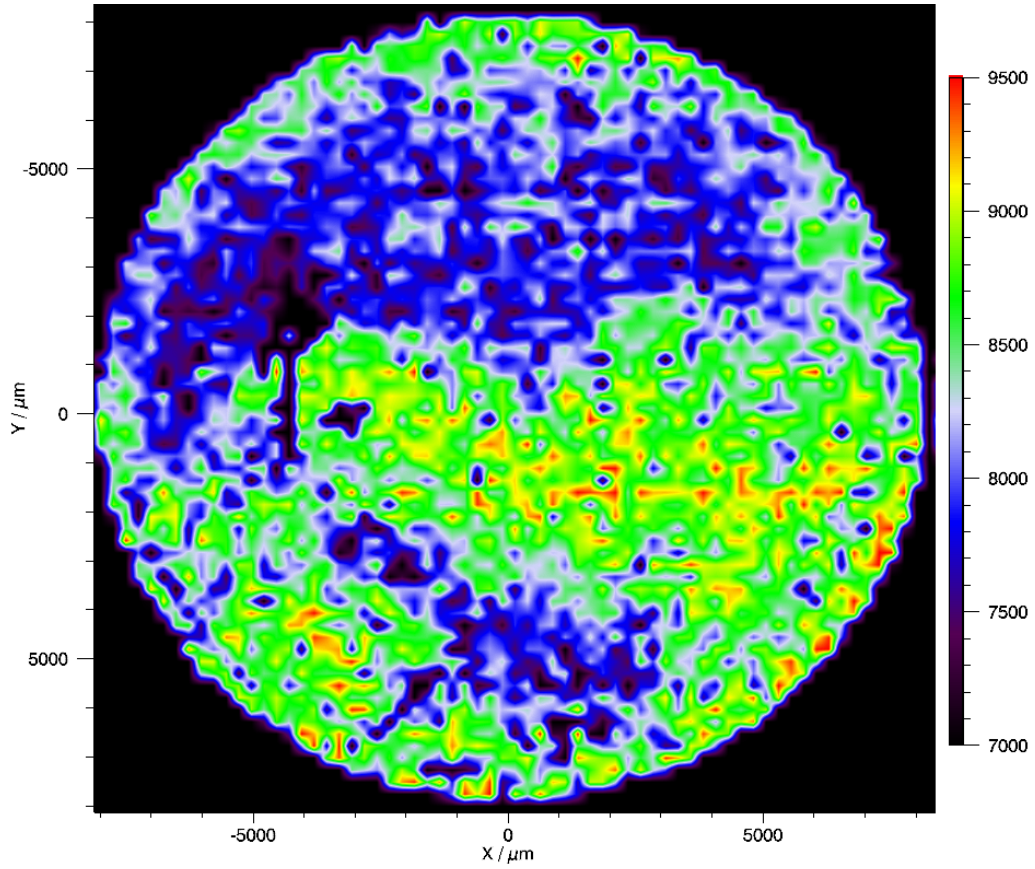


Figure 61. False color Raman peak intensity map of the semiconducting sample 127 B highlighting the D peak alone at 1341 cm^{-1} after the 2 irradiations, one at 500 keV (lower right) and one at 1 MeV (lower left). The scale on the right is the peak intensity count in arbitrary units.

Appendix B. Appendix AFM

2.1 Atomic Force Images

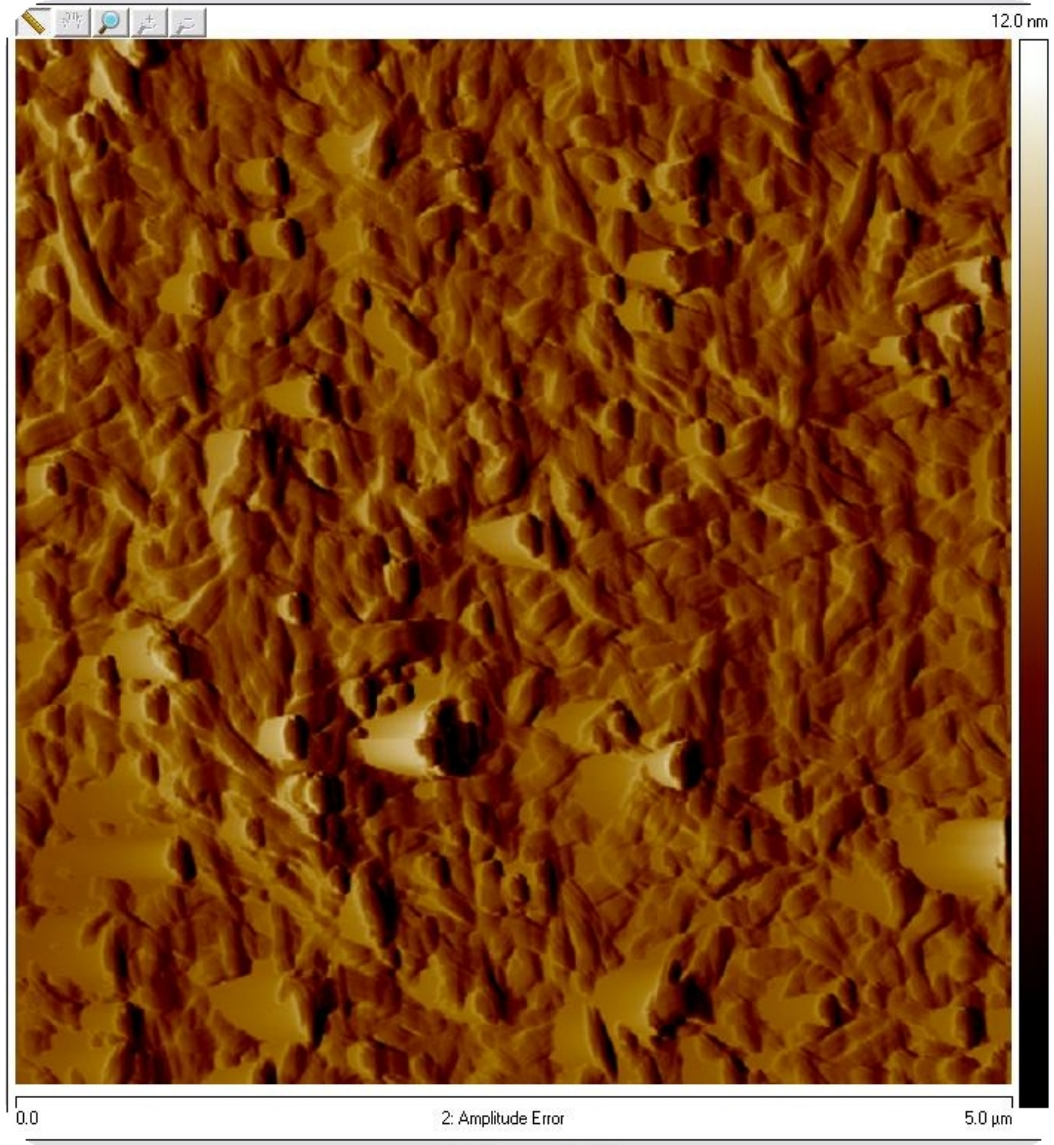


Figure 62. Atomic force microscope image of metallic SWCNTs after $5.8 \times 10^{17} \frac{e^-}{cm^2}$ irradiation.

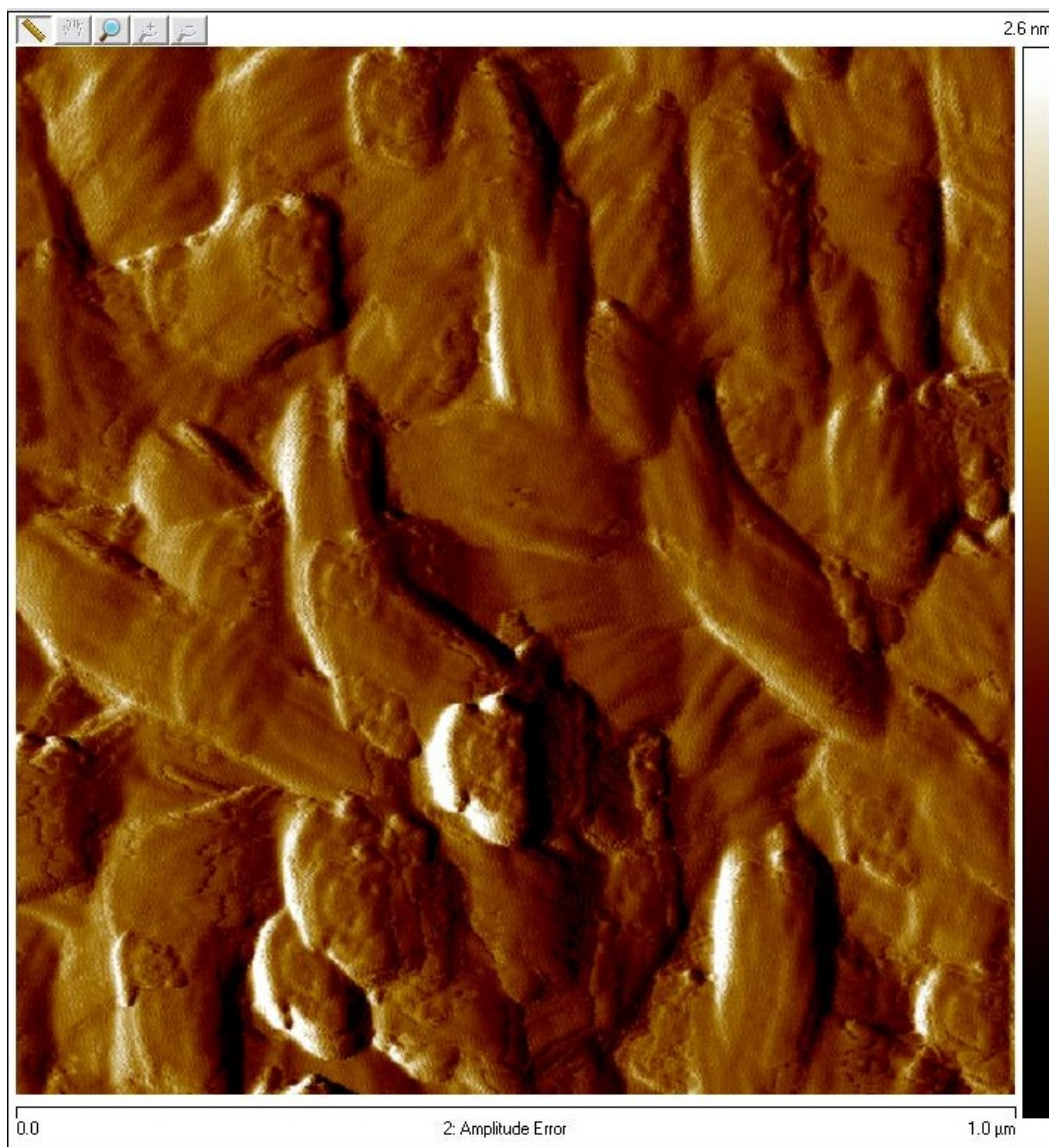


Figure 63. Atomic force microscope image zoomed in to $1\ \mu\text{m}$ of metallic SWCNTs after $5.8 \times 10^{17}\ \frac{e^-}{\text{cm}^2}$ irradiation.

2.2 Kelvin Probe Images

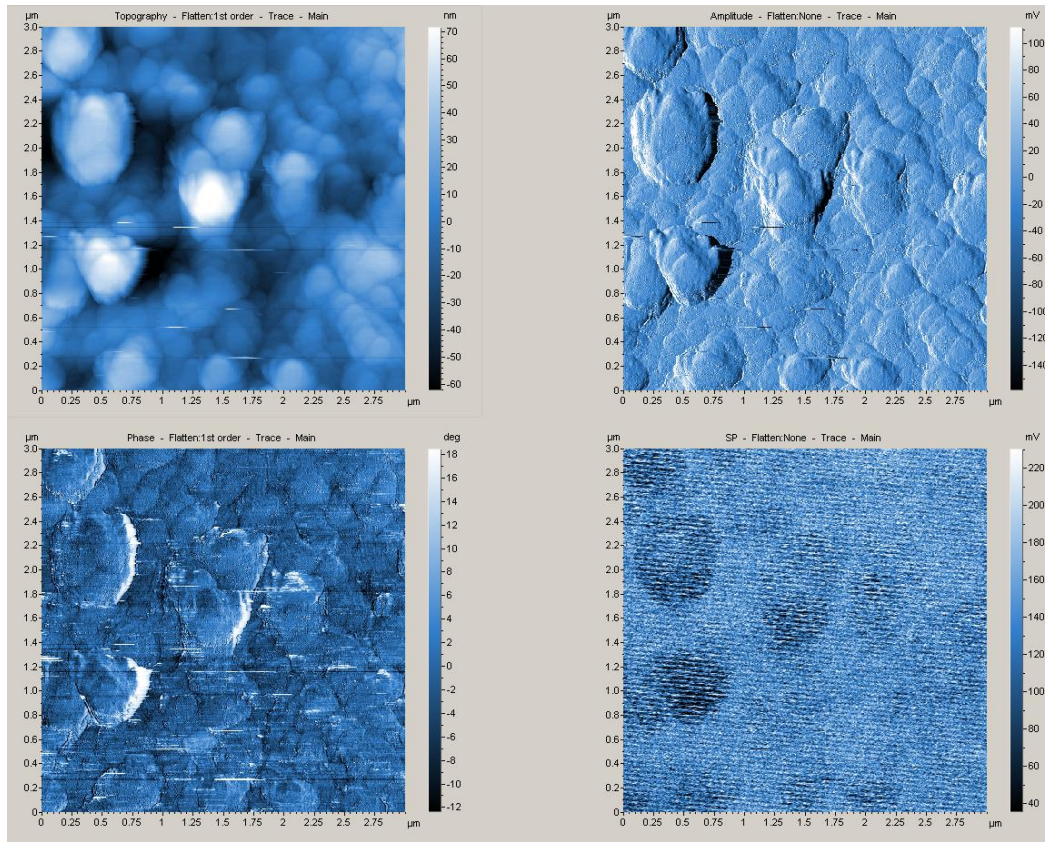


Figure 64. Kelvin Probe microscopy of the metallic sample 127 A on the unirradiated part

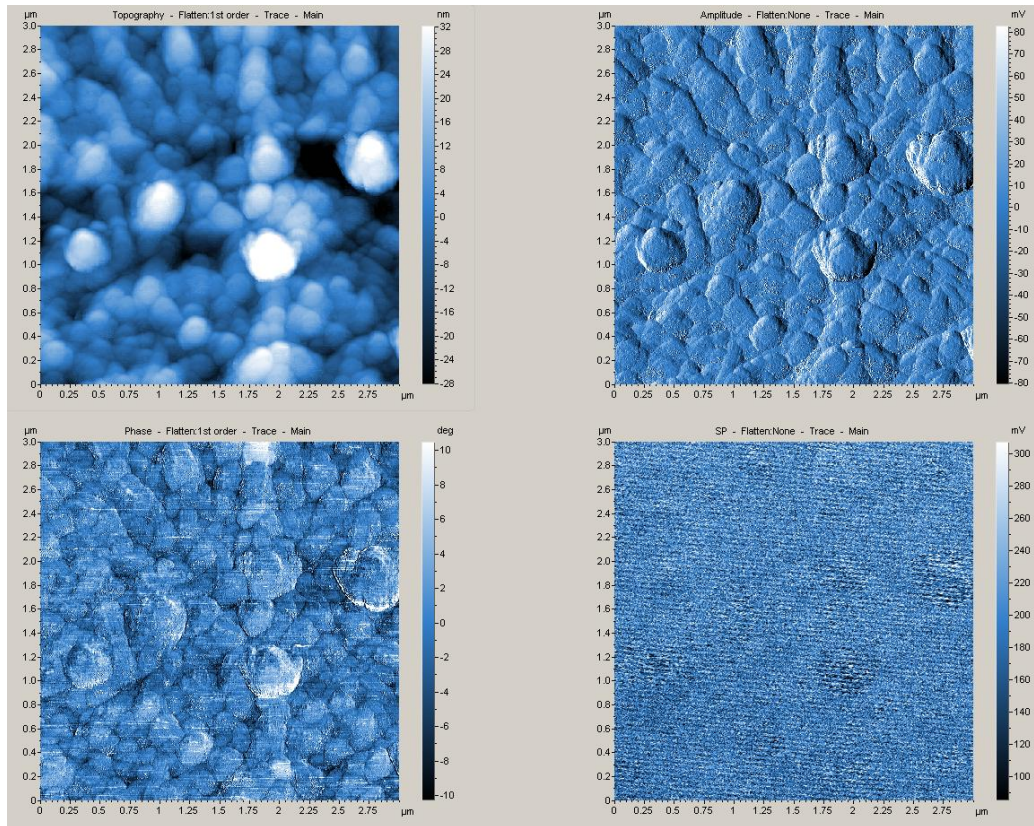


Figure 65. Kelvin Probe microscopy of the metallic sample 127 A on the $1.0 \times 10^{16} \frac{e^-}{cm^2}$ irradiation.

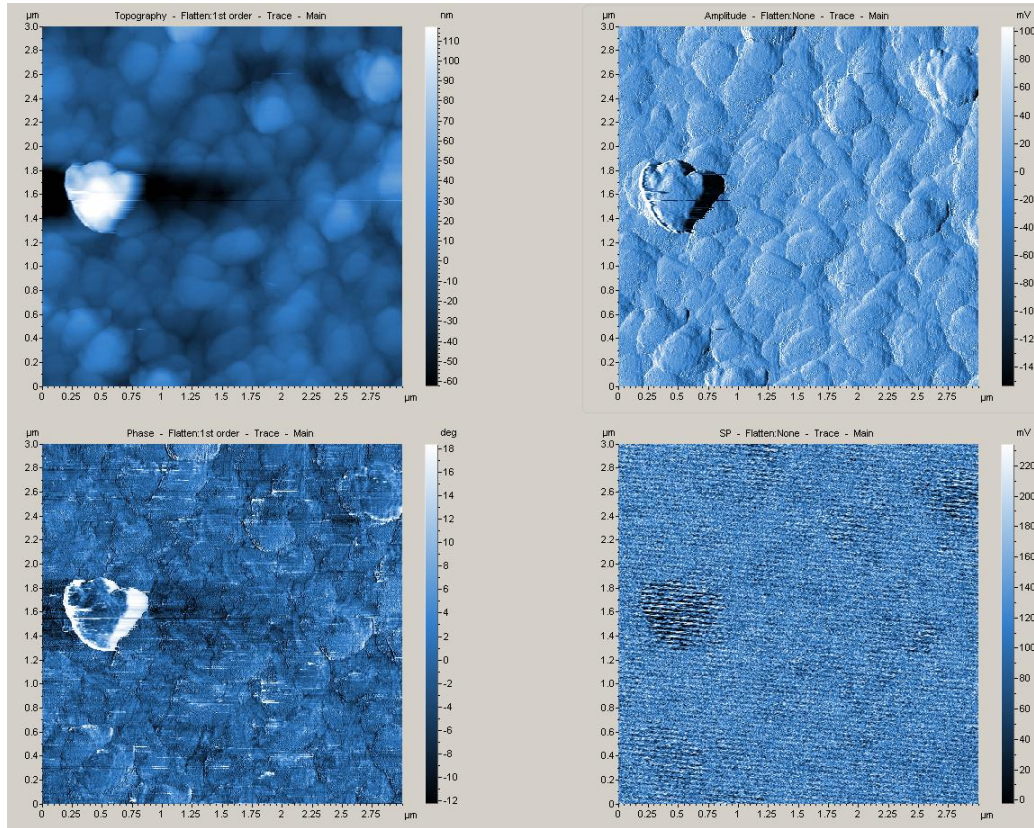


Figure 66. Kelvin Probe microscopy of the metallic sample 127 A on the $1.0 \times 10^{17} \frac{e^-}{cm^2}$ irradiation.

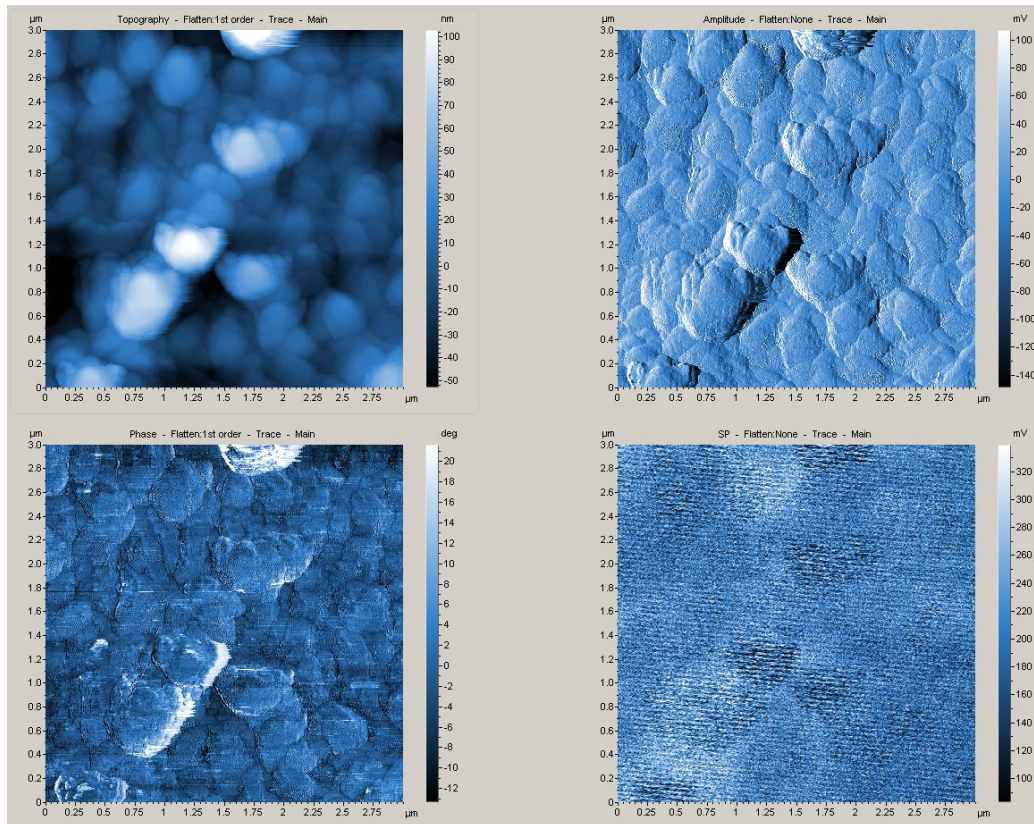


Figure 67. Kelvin Probe microscopy of the metallic sample 127 A on the $5.8 \times 10^{17} \frac{e^-}{\text{cm}^2}$ irradiation.

Appendix C. Modeling

3.1 Monte Carlo Modeling: CASINO

CASINO is a Monte Carlo modeling code that uses iteration algorithms to converge on a solution. Specifically, this is used to model electrons accelerated through different velocities and their interactions in materials. The code used for this experiment is version 2.42. This code includes many different adjustable parameters in the simulation. The most notable parameters for this experiment are the acceleration voltage, material thickness, and number of electrons per unit time (flux). These parameters influence the interaction probability with the carbon nanotubes as a function of time and energy.

The results of the Casino Model show that most of the electrons pass through the samples without interacting at all, until they get to the silicon substrate, where there are enough interactions to slow the electrons down. This is where they deposit most of their energy, which contributes to heating of the Si substrate.

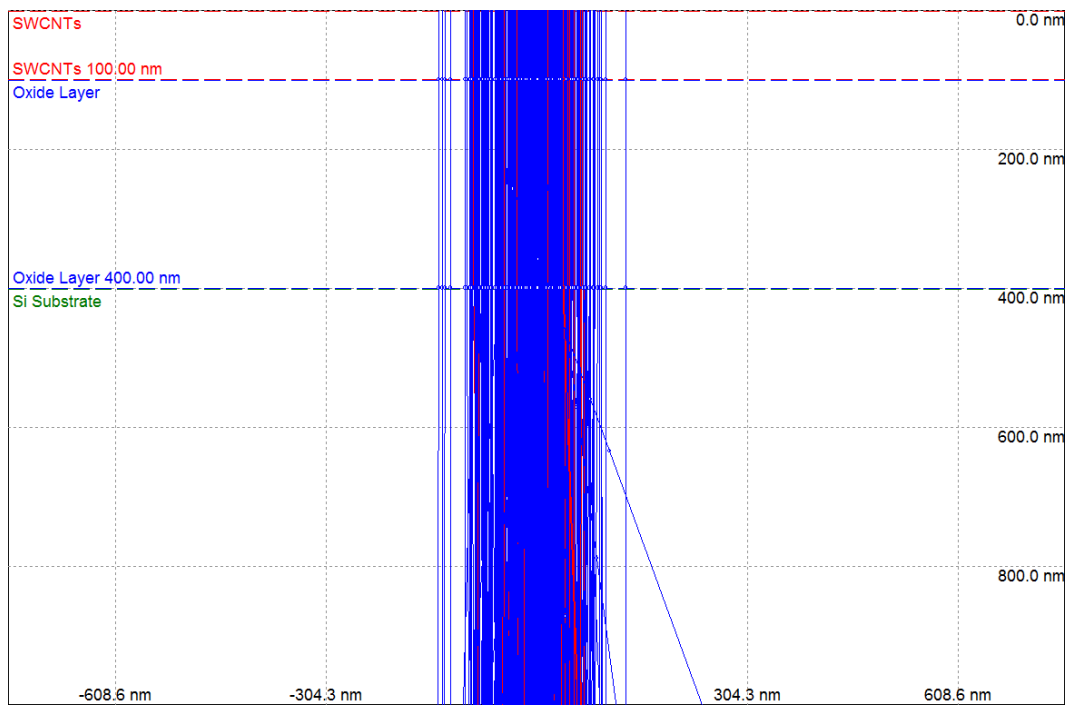


Figure 68. Casino model of 500 keV electrons incident from the top with the sample geometry as described in Chapter II. There are 200 electrons displayed here, with 1000 simulated. All of the simulated electrons pass through the CNT layer with little to no interaction. The CNT density is calculated from the physical sample geometry to be 1 g/cm^3 .

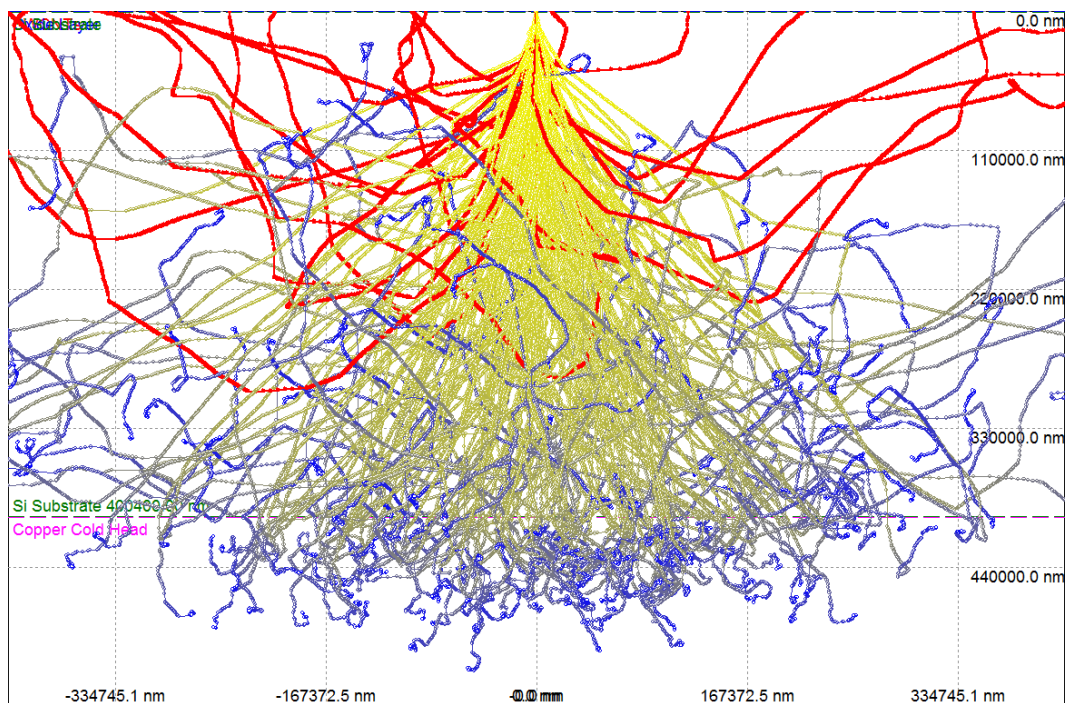


Figure 69. Casino model of 500 keV electrons incident from the top with the sample geometry as described in Chapter II. There are 200 electrons displayed here, with 1000 simulated. The CNT density is calculated from the physical sample geometry to be 1 g/cm^3 . This image shows where the electrons are stopping and depositing most of their energy. The color indicated the average intensity of the electrons as they slow down and interact with the sample geometry.

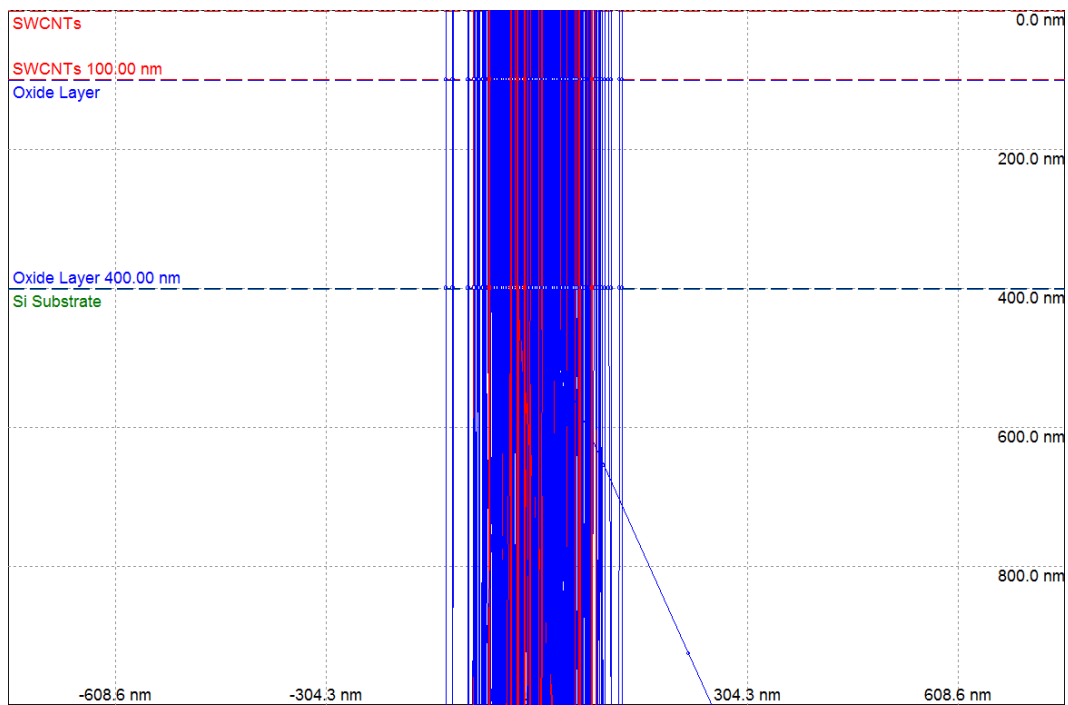


Figure 70. Casino model of 1 MeV electrons incident from the top with the sample geometry as described in Chapter II. There are 200 electrons displayed here, with 1000 simulated. All of the simulated electrons pass through the CNT layer with little to no interaction. The CNT density is calculated from the physical sample geometry to be 1 g/cm^3 .

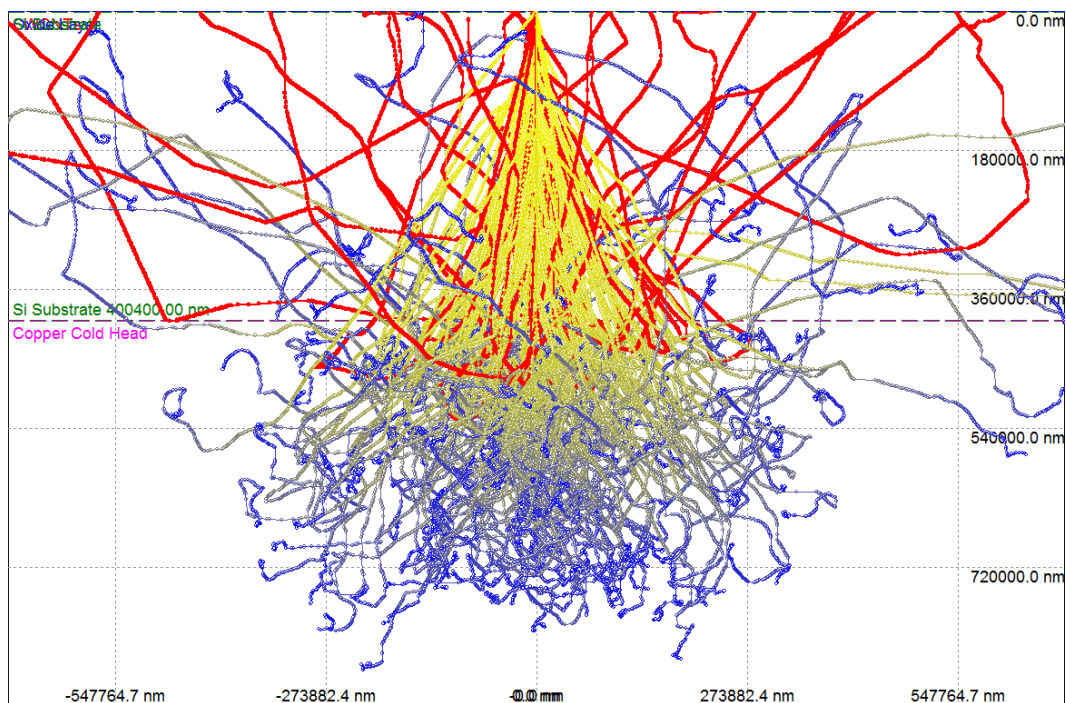


Figure 71. Casino model of 1 MeV electrons incident from the top with the sample geometry as described in Chapter II. There are 200 electrons displayed here, with 1000 simulated. The CNT density is calculated from the physical sample geometry to be 1 g/cm^3 . This image shows where the electrons are stopping and depositing most of their energy. The color indicated the average intensity of the electrons as they slow down and interact with the sample geometry.

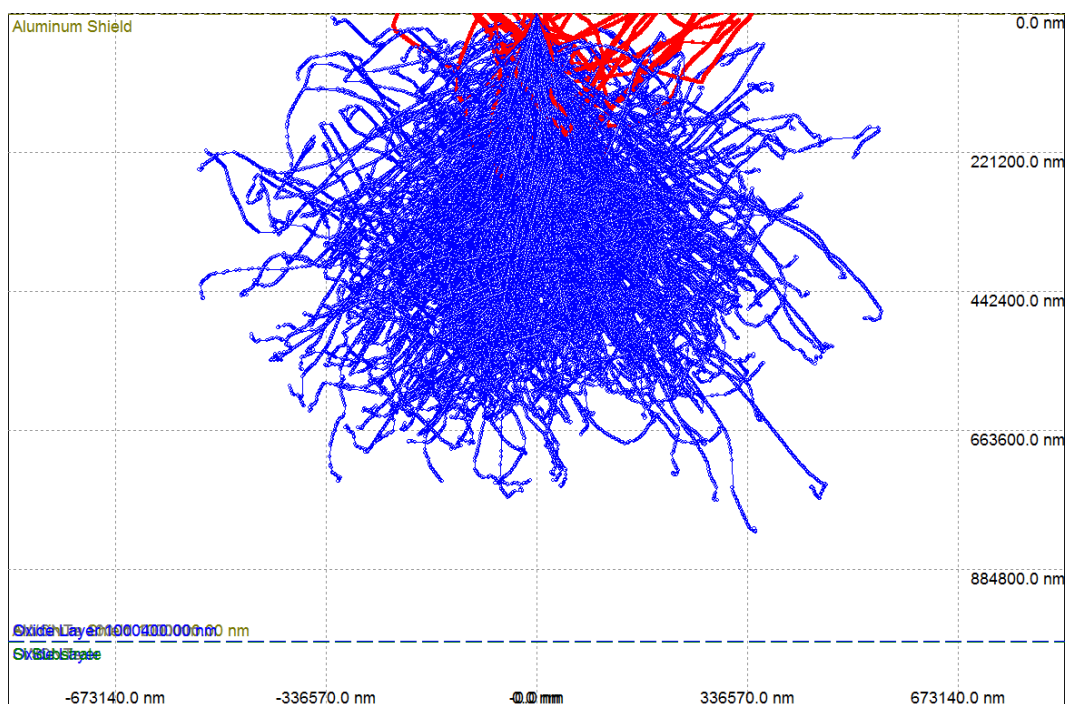


Figure 72. Casino simulation of 500 keV electrons onto the experimental setup using a 1 mm sheet of aluminum to shield the sample from the incident electrons. This shows that the electrons stop before .7 mm of aluminum and none reach the sample structure, proving the viability of aluminum to shield the sample.

Appendix D. MathCad Dynamitron Calculations

The fluence from the Dynamitron is calculated using the following equations in sequence: The diameter of the spot is measured directly from the collimator. In this case all irradiations were done with a 7 mm diameter collimator. This number is used to calculate the area of the irradiated spot.

$$A_{spot} = \frac{\pi d^2}{4} \text{ cm}^2 \quad (17)$$

with A being the spot area, and d being the spot diameter.

The current divided by the irradiated spot area gives the current density.

$$J = \frac{I}{A_{spot}} \quad (18)$$

in units of $\frac{\text{amps}}{\text{cm}^2}$. While the dose rate on the sample, The current density can be used to calculate the power density with:

$$\text{Power Density} = J * E \frac{\text{Watts}}{\text{cm}^2} \quad (19)$$

Where E is the electron energy. Here the energy is at 500 keV.

$$\text{Dose Rate} = \frac{J}{q(1.602 \times 10^{-19})} \quad (20)$$

which has units of $\frac{e^-}{\text{cm}^2 * \text{sec}}$. The equation used to calculate the time of irradiation in hours based on a specific current obtainable on the system, and the desired total fluence is given by:

$$\text{Time} = \frac{\text{Fluence}(\frac{e^-}{\text{cm}^2}) * A_{spot}(\text{cm}^2)}{\frac{I}{q(\text{Coulombs})} * \frac{3600s}{hr}} \quad (21)$$

The total current from the beam line is gathered through the cold head which is

isolated in a Faraday cup fashion, meaning the sample stage and cold head are electrically isolated from the rest of the system. A current integrator with an analog readout is wired to the cold head through long wires into the Dynamitron control room.

$$\begin{aligned}
 & \text{ddyn} := 2.7 \\
 & \text{inputs-->} \quad i := .2 \cdot 10^{-6} \quad \text{amps} \quad \text{dspot} := .5 \quad \text{cm} \quad d := .75 \\
 & \text{Dose} := 2.06 \cdot 10^{16} \quad \frac{\text{electrons}}{\text{cm}^2} \quad \text{Aspot} := \frac{\text{dspot}^2 \cdot \pi}{4} \quad \text{Aspot} = 0.196 \quad \text{cm}^2 \\
 & \text{Scale} := 6 \cdot (10)^{-6} \quad \text{cm} \\
 & E := .5 \cdot 10^6 \quad \text{eV} \quad \text{A} := \frac{d^2 \cdot \pi}{4} \quad A = 0.49 \quad \text{cm}^2 \\
 & J := \frac{i}{A} \quad J = 4.08 \times 10^{-7} \quad \frac{\text{amps}}{\text{cm}^2} \quad \text{Jspot} := \frac{i}{\text{Aspot}} \quad \text{Jspot} = 1.019 \times 10^{-6} \quad \frac{\text{amps}}{\text{cm}^2} \\
 & \text{powerdensity} := J \cdot E \quad \text{powerdensity} = 0.204 \quad \frac{\text{watts}}{\text{cm}^2} \\
 & \text{Dose_rate} := \frac{J}{1.6 \cdot 10^{-19}} \quad \text{Dose_rate} = 2.55 \times 10^{12} \quad \frac{\text{electrons}}{\text{cm}^2 \cdot \text{sec}} \\
 & \text{Dose_rate_spot} := \frac{\text{Jspot}}{1.6 \cdot 10^{-19}} \quad \text{Dose_rate_spot} = 6.366 \times 10^{12} \quad \frac{\text{electrons}}{\text{cm}^2 \cdot \text{sec}} \\
 & \text{ChargeDose} := \text{Dose} \cdot 1.602 \cdot 10^{-19} \quad \text{ChargeDose} = 3.3 \times 10^{-3} \quad \frac{\text{Coulombs}}{\text{cm}^2} \\
 & \text{charge} := \text{ChargeDose} \cdot A \quad \text{charge} = 1.618 \times 10^{-3} \quad \text{Coulombs} \\
 & \text{tsec} := \frac{\text{ChargeDose}}{J} \quad \text{tmin} := \frac{\text{tsec}}{60} \quad \text{thours} := \frac{\text{tsec}}{3600} \\
 & \text{tsec} = 8.088 \times 10^3 \quad \text{tmin} = 134.8 \quad \text{thours} = 2.25 \\
 & \text{calibrationcorrection} := 1.0 \\
 & \text{TotalCoul} := \text{ChargeDose} \cdot A \quad \text{TotalCoul} = 1.618 \times 10^{-3} \\
 & \text{TotalCount} := \frac{\text{TotalCoul}}{\text{Scale}} \quad \text{TotalCount} = 269.6
 \end{aligned}$$

Appendix E. Follow-On Procedures

This appendix is written in the hopes that should another masters student follow my work, they can have a road map to follow.

1. Get metallic and semiconducting Hall samples from RIT or NRL with metal contacts (gold, palladium, or anything that will stick).
2. Use a profilometer to determine thin film height. Or alternatively use AFM to get average thickness (and surface images).
3. Measure Raman on each sample with a mapping set using 25-50 points of measurement around the whole sample. Make sure the alignment is repeatable. Take optical images of the sample in the Raman system using the montage function. Save these as .jpg and .png. Use both 514.5 nm and 633 nm lasers on each sample. Use at least 5 seconds of acquisition, with 2 or more integrations with focus track on each spot. The main spectral range should be 1200 to 2800 cm^{-1} .
4. Do a separate study on the RBM using 2 laser wavelengths (514.5 and 633 nm) with the highest grating available encompassing a spectral range from 0 to 600 cm^{-1} . This range will allow capture of the silicon peak to be used as a normalization parameter when comparing pre- and post-irradiations. Try to get 20000 counts in the RBM, or as many as possible. The RBM focus (over 25 spots with map function) will facilitate deconvolution of the annealing effects, and the diameter dependent CNT degradations.
5. Measure ex-situ temperature dependent Hall in Dr. Look's Hall lab. (down the hall from Raman lab in Sensors directorate.) Go to liquid helium temps (6 K) and measure every 5 K up to as high as they will go. Have Tim Cooper leave the wires on the sample to mount on the electron beam.

6. Take samples to electron beam at WSU. Mount to the copper cold head with vacuum grease or double sided tape, use 7mm columnator (after verifying spot location with test burn). Wire up feed through to either the Ecopia HMS, or a Keithley to measure the Hall. (alternatively you can just measure resistivity.) Ideally there should be a temperature probe on the copper cold head block to determine the temperatures at each measurement.
7. Take IV and Hall measurements in ambient pressure and temperature before pumping down. Start the load lock pump, measure the IV and Hall as its pumping down to get an idea of the pressure dependent resistivity / conductivity. Keep time metrics on pump down and measurements as well.
8. Open load lock, note pressure on control panel, measure Hall and IV as it pumps down. When the pressure gets to 1×10^{-6} torr, it is ready to shoot.
9. Ensure Ecopia is shielded with lead bricks and chiller is on.
10. Shoot sample at 1 MeV up to a fluence of 1×10^{16} electrons per cm^2 . Stop beam.
11. Measure Hall and IV.
12. Start beam again. Shoot to a fluence of 1×10^{17} electrons per cm^2 . Stop beam.
13. Measure Hall and IV.
14. Iterate above for 5×10^{17} electrons per cm^2 and 1×10^{18} electrons per cm^2 .
15. Remove sample, place in vacuum bag for transport to AFRL. Do ex-situ temperature dependent Hall measurements down to 6 K again using same settings.
16. Repeat Raman measurements.

17. Repeat AFM or profilometer measurements.

Bibliography

- [1] M. S. Dresselhaus, G. Dresselhaus, J. C. Charlier, and E. Hernandez, “Electronic, thermal and mechanical properties of carbon nanotubes.” *Philosophical transactions. Series A, Mathematical, physical, and engineering sciences*, vol. 362, no. 1823, pp. 2065–98, Oct. 2004. [Online]. Available: <http://www.ncbi.nlm.nih.gov/pubmed/15370472>
- [2] C. D. Cress, C. M. Schauerma, B. J. Landi, S. R. Messenger, R. P. Raffaele, and R. J. Walters, “Radiation effects in single-walled carbon nanotube papers,” *Journal of Applied Physics*, vol. 107, no. 1, p. 014316, 2010. [Online]. Available: <http://link.aip.org/link/JAPIAU/v107/i1/p014316/s1&Agg=doi>
- [3] J. E. Rossi, C. D. Cress, A. R. Helenic, C. M. Schauerma, R. A. DiLeo, N. D. Cox, S. R. Messenger, B. D. Weaver, S. M. Hubbard, and B. J. Landi, “Ion irradiation of electronic-type-separated single wall carbon nanotubes: A model for radiation effects in nanostructured carbon,” *Journal of Applied Physics*, vol. 112, no. 3, pp. 034314–034314–11, aug 2012.
- [4] F. Banhart, “Irradiation effects in carbon nanostructures,” *Reports on Progress in Physics*, vol. 62, no. 8, p. 1181, 1999.
- [5] V. Skákalová, A. Kaiser, U. Dettlaff, K. Arstila, A. Krashennnikov, J. Keinonen, and S. Roth, “Electrical properties of C4+ irradiated single-walled carbon nanotube paper,” *Physica Status Solidi (b)*, vol. 245, no. 10, pp. 2280–2283, 2008.
- [6] V. Skákalová, A. Kaiser, Z. Osváth, G. Vértessy, L. Biró, and S. Roth, “Ion irradiation effects on conduction in single-wall carbon nanotube networks,” *Applied Physics A: Materials Science & Processing*, vol. 90, no. 4, pp. 597–602, 2008.
- [7] C. D. Cress, J. J. Mcmorrow, S. Member, J. T. Robinson, A. L. Friedman, and B. J. Landi, “Radiation Effects in Single-Walled Carbon Nanotube,” *IEEE Transactions on Nuclear Science*, vol. 57, no. 6, pp. 3040–3045, 2010.
- [8] E. Stassinopoulos and J. Raymond, “The space radiation environment for electronics,” *Proceedings of the IEEE*, vol. 76, no. 11, pp. 1423–1442, nov 1988.
- [9] M. S. Dresselhaus, G. Dresselhaus, and R. Saito, “Physics of carbon nanotubes,” *Carbon*, vol. 33, no. 7, pp. 883–891, 1995.
- [10] H. C. Chuan, “Modeling and Analysis of Ballistic Carbon Nanotube Field Effect Transistor (CNTFET) with Quantum Transport Concept,” Thesis, Malaysia, 2007.
- [11] Y. S. Rao, “Carbon Nanotubes Field Effect Transistors : A Review,” *International Journal of Electronics & Communication Technology*, vol. 7109, pp. 204–208, 2011.

- [12] S. S. Iijima, “Helical microtubules of graphitic carbon,” *Nature (London)*, vol. 354, no. 6348, pp. 56–58, -11 1991, doi:10.1038/354056a0 pmid:.
- [13] M. Biercuk, S. Ilani, C. Marcus, and P. McEuen, “Electrical transport in single-wall carbon nanotubes,” *Carbon Nanotubes*.
- [14] S. S. Iijima, “Single-shell carbon nanotubes of 1-nm diameter,” *Nature (London)*, vol. 363, no. 6430, pp. 603–605, -06 1993, doi:10.1038/363603a0 pmid:.
- [15] S. Iijima, “Growth of carbon nanotubes,” *Materials science and engineering*, vol. 19, no. 1-2, p. 172, 1993, doi: pmid:.
- [16] S. S. Iijima, “Carbon nanotubes: past, present, and future,” *Physica B: Condensed Matter*, vol. 323, no. 104, pp. 1–5, 10 2002.
- [17] V. Djordjević, J. Djustebek, J. Cvetičanin, S. Velićknović, M. Veljković, M. Bokorov, B. B. Stojić, and O. Nešković, “Methods of purification and characterization of carbon nanotubes,” *Journal of Optoelectronics and Advanced Materials*, vol. 8, no. 4, pp. 1631–1634, 2006.
- [18] M. Arnold, A. Green, J. Hulvat, S. Stupp, and M. Hersam, “Sorting carbon nanotubes by electronic structure using density differentiation,” *Nature nanotechnology*, vol. 1, no. 1, pp. 60–65, 2006.
- [19] B. J. Landi, C. D. Cress, and R. P. Raffaele, “High energy density lithium-ion batteries with carbon nanotube anodes,” *Journal of Materials Research*, vol. 25, no. 08, pp. 1636–1644, Jan. 2011. [Online]. Available: http://www.journals.cambridge.org/abstract_S0884291400007743
- [20] P. R. Bandaru, “Electrical Properties and Applications of Carbon Nanotube Structures,” *Journal of Nanoscience and Nanotechnology*, vol. 7, no. 4, pp. 1239–1267, Apr. 2007. [Online]. Available: <http://openurl.ingenta.com/content/xref?genre=article&issn=1533-4880&volume=7&issue=4&spage=1239>
- [21] P. Avouris, J. Appenzeller, R. Martel, and S. Wind, “Carbon nanotube electronics,” *Proceedings of the IEEE*, vol. 91, no. 11, pp. 1772–1784, 2003.
- [22] R. Eisberg and R. Resnick, *Quantum Physics*. John Wiley, 1985.
- [23] V. Gavryushin, “Graphene Brillouin Zone and Electronic Energy Dispersion,” 2012. [Online]. Available: <http://demonstrations.wolfram.com/GrapheneBrillouinZoneAndElectronicEnergyDispersion/>
- [24] S. Rols, Z. Benes, E. Anglaret, J. Sauvajol, P. Papanek, J. Fischer, G. Coddens, H. Schober, and A. Dianoux, “Phonon density of states of single-wall carbon nanotubes,” *Physical review letters*, vol. 85, no. 24, pp. 5222–5, Dec. 2000. [Online]. Available: <http://www.ncbi.nlm.nih.gov/pubmed/11102226>

- [25] S. Reich, J. Maultzsch, C. Thomsen, and P. Ordejón, “Tight-binding description of graphene,” *Physical Review B*, vol. 66, no. 3, p. 035412, 2002.
- [26] S. M. Sze, *Semiconductor devices: Physics and Technology*. New York [u.a.]: Wiley, 2002, iD: 247983020.
- [27] H. Chang, J. Do Lee, S. Lee, and Y. Lee, “Adsorption of NH and NO molecules on carbon nanotubes,” *Applied Physics Letters*, vol. 79, p. 3863, 2001.
- [28] D. Kang, N. Park, J. Hyun, E. Bae, J. Ko, J. Kim, and W. Park, “Adsorption-induced conversion of the carbon nanotube field effect transistor from ambipolar to unipolar behavior,” *Applied Physics Letters*, vol. 86, no. 9, pp. 093 105–093 105, 2005.
- [29] P. Collins, K. Bradley, M. Ishigami, and A. Zettl, “Extreme oxygen sensitivity of electronic properties of carbon nanotubes,” *Science*, vol. 287, no. 5459, pp. 1801–1804, 2000.
- [30] A. A. Zahab, “Water-vapor effect on the electrical conductivity of a single-walled carbon nanotube mat,” *Physical review.B, Condensed matter*, vol. 62, no. 15, pp. 10 000–10 003, -10 2000, doi:10.1103/PhysRevB.62.10000 pmid:.
- [31] A. Krasheninnikov and K. Nordlund, “Irradiation effects in carbon nanotubes,” *Nuclear Instruments and Methods in Physics Research Section B: Beam Interactions with Materials and Atoms*, vol. 216, no. 0, pp. 355 – 366, 2004, proceedings of the E-MRS 2003 Symposium E on Ion Beams for Nanoscale Surface Modifications. [Online]. Available: <http://www.sciencedirect.com/science/article/pii/S0168583X03021104>
- [32] B. W. Smith and D. E. Luzzi, “Electron irradiation effects in single wall carbon nanotubes.” *Journal of Applied Physics*, vol. 90, no. 7, p. 3509, 2001. [Online]. Available: <http://search.ebscohost.com/login.aspx?direct=true&db=aph&AN=5227851&site=ehost-live>
- [33] A. Akkerman, J. Barak, M. Chadwick, J. Levinson, M. Murat, and Y. Lifshitz, “Updated NIEL calculations for estimating the damage induced by particles and γ -rays in Si and GaAs,” *Radiation Physics and Chemistry*, vol. 62, no. 4, pp. 301–310, 2001.
- [34] A. V. Krasheninnikov, K. Nordlund, M. Sirviö, E. Salonen, and J. Keinonen, “Formation of ion-irradiation-induced atomic-scale defects on walls of carbon nanotubes,” *Phys. Rev. B*, vol. 63, p. 245405, May 2001. [Online]. Available: <http://link.aps.org/doi/10.1103/PhysRevB.63.245405>
- [35] G. Gerasimov, “Radiation stability of carbon nanostructures,” *Journal of Engineering Physics and Thermophysics*, vol. 83, no. 2, pp. 393–400, 2010.

- [36] K. Yanagi, H. Udoguchi, S. Sagitani, Y. Oshima, T. Takenobu, H. Kataura, T. Ishida, K. Matsuda, and Y. Maniwa, "Transport Mechanisms in Metallic and Semiconducting Single-Wall Carbon Nanotube Networks," *ACS Nano*, vol. 4, no. 7, pp. 4027–4032, 2010. [Online]. Available: <http://pubs.acs.org/doi/abs/10.1021/nn101177n>
- [37] L. J. Van der Pauw, "A method of measuring the resistivity and Hall coefficient on lamellae of arbitrary shape," *Philips technical review*, vol. 20, no. 8, p. 220, 1958, doi: pmid:.
- [38] J. R. Schwank, M. R. Shaneyfelt, D. M. Fleetwood, J. A. Felix, P. E. Dodd, P. Paillet, and V. Ferlet-Cavrois, "Radiation Effects in MOS Oxides," *Nuclear Science, IEEE Transactions on*, vol. 55, no. 4, pp. 1833–1853, 2008, iD: 1.
- [39] G. Rius, I. Martín, P. Godignon, A. Bachtold, J. Bausells, E. Lora-Tamayo, and F. Pérez-Murano, "Response of carbon nanotube transistors to electron beam exposure," *Microelectronic Engineering*, vol. 84, no. 5-8, pp. 1596–1600, May 2007. [Online]. Available: <http://linkinghub.elsevier.com/retrieve/pii/S0167931707002249>
- [40] M. Dresselhaus, G. Dresselhaus, R. Saito, and a. Jorio, "Raman spectroscopy of carbon nanotubes," *Physics Reports*, vol. 409, no. 2, pp. 47–99, Mar. 2005. [Online]. Available: <http://linkinghub.elsevier.com/retrieve/pii/S0370157304004570>
- [41] M. Hulman, V. Skákalová, S. Roth, and H. Kuzmany, "Raman spectroscopy of single-wall carbon nanotubes and graphite irradiated by γ rays," *Journal of applied physics*, vol. 98, no. 2, pp. 024311–024311, 2005.
- [42] A. Jorio, R. Saito, J. H. Hafner, C. M. Lieber, M. Hunter, T. McClure, G. Dresselhaus, and M. S. Dresselhaus, "Structural (n, m) Determination of Isolated Single-Wall Carbon Nanotubes by Resonant Raman Scattering," *Phys. Rev. Lett.*, vol. 86, pp. 1118–1121, Feb 2001. [Online]. Available: <http://link.aps.org/doi/10.1103/PhysRevLett.86.1118>
- [43] G. Wertheim, "Electron-bombardment damage in silicon," *Physical Review*, vol. 110, no. 6, p. 1272, 1958.
- [44] J. Srour, C. J. Marshall, and P. W. Marshall, "Review of displacement damage effects in silicon devices," *Nuclear Science, IEEE Transactions on*, vol. 50, no. 3, pp. 653–670, 2003.
- [45] S. Costa, E. Borowiak-Palen, M. Kruszynska, A. Bachmatiuk, and R. Kalenczuk, "Characterization of carbon nanotubes by Raman spectroscopy," *Mater Sci Poland*, vol. 26, no. 2, pp. 433–441, 2008.

REPORT DOCUMENTATION PAGE

Form Approved
OMB No. 0704-0188

The public reporting burden for this collection of information is estimated to average 1 hour per response, including the time for reviewing instructions, searching existing data sources, gathering and maintaining the data needed, and completing and reviewing the collection of information. Send comments regarding this burden estimate or any other aspect of this collection of information, including suggestions for reducing this burden to Department of Defense, Washington Headquarters Services, Directorate for Information Operations and Reports (0704-0188), 1215 Jefferson Davis Highway, Suite 1204, Arlington, VA 22202-4302. Respondents should be aware that notwithstanding any other provision of law, no person shall be subject to any penalty for failing to comply with a collection of information if it does not display a currently valid OMB control number. **PLEASE DO NOT RETURN YOUR FORM TO THE ABOVE ADDRESS.**

1. REPORT DATE (DD-MM-YYYY) 21-03-2013			2. REPORT TYPE Master's Thesis		3. DATES COVERED (From — To) 20 Aug 2011 - 21 Mar 2013	
4. TITLE AND SUBTITLE Electron Damage Effects on Carbon Nanotube Thin Films					5a. CONTRACT NUMBER	
					5b. GRANT NUMBER	
					5c. PROGRAM ELEMENT NUMBER	
6. AUTHOR(S) Best, Jeremy S., Capt, USMC					5d. PROJECT NUMBER N/A	
					5e. TASK NUMBER	
					5f. WORK UNIT NUMBER	
7. PERFORMING ORGANIZATION NAME(S) AND ADDRESS(ES) Air Force Institute of Technology Graduate School of Engineering and Management (AFIT/EN) 2950 Hobson Way WPAFB OH 45433-7765					8. PERFORMING ORGANIZATION REPORT NUMBER AFIT-ENP-13-M-37	
9. SPONSORING / MONITORING AGENCY NAME(S) AND ADDRESS(ES) AS&T, NRL 4555 Overlook Ave., SW Washington, DC 20375 (202) 767-3462, cory.cress@nrl.navy.mil					10. SPONSOR/MONITOR'S ACRONYM(S) NRL	
					11. SPONSOR/MONITOR'S REPORT NUMBER(S)	
12. DISTRIBUTION / AVAILABILITY STATEMENT APPROVED FOR PUBLIC RELEASE; DISTRIBUTION UNLIMITED.						
13. SUPPLEMENTARY NOTES						
14. ABSTRACT Thin films (50-100 nm) of electronic type separated (metallic and semiconducting) single walled carbon nanotubes deposited on SiO ₂ - Si substrates are investigated pre- and post-irradiation with 500 keV electrons at fluences $10^{16} \frac{e^-}{cm^2}$ using Raman spectroscopy and temperature dependent Hall measurements to determine the damage effects and mechanisms of device degradation. A decrease in the conductivity of the single walled carbon nanotube thin films is first observed at a fluence level of $1.0 \times 10^{16} \frac{e^-}{cm^2}$ and becomes more significant at fluences above $1.0 \times 10^{17} \frac{e^-}{cm^2}$. The temperature dependent Hall measurements showed an 82% decrease in conductivity at the highest fluence level. The D/G and D/G' ratios of the Raman peak intensities showed an increase of 10 to 40% post irradiation. The increases in the D/G ratios indicate a significant increase in the defect density in the carbon nanotubes through electron interactions with the nanotube structures.						
15. SUBJECT TERMS Carbon Nanotubes, Electron Damage, Raman spectroscopy, Hall measurements						
16. SECURITY CLASSIFICATION OF:			17. LIMITATION OF ABSTRACT	18. NUMBER OF PAGES	19a. NAME OF RESPONSIBLE PERSON	
a. REPORT	b. ABSTRACT	c. THIS PAGE			Dr. John McClory	
U	U	U	UU	127	19b. TELEPHONE NUMBER (include area code) (937)255-3636 x4571; john.mcclory@afit.edu	